Column III Nitride Growth, Characterization and Devices

Thesis by

Robert A. Beach Jr.

In Partial Fulfillment of the Requirements

for the Degree of

Doctor of Philosophy

California Institute of Technology

Pasadena, California

2001

(Submitted April 23, 2001)

To my parents Dave and Karen Smith,

and to all my family

for years of love and support.

Acknowledgements

When I look back at all the years it took to get to this point, it makes me wonder how on earth I ever made it. The one thing that stands out above all the rest is the constant support and encouragment of my family. Never did I hear the words "You can't.", or "Don't bother, you won't make it anyway." It was always "You can do it, if you put your mind to it." So I did, because I could. Parents never lie. I'd also like to thank my sisters for putting up with their bratty little brother and not just drowning me in the tub when I was young. To the professors at Cal Poly, you have a great rapport with the students. I couldn't imagine a better atmosphere in which to learn. I'd like to single out Dr. Foster for rekindling my interest in Physics and proving that learning can be fun, and Dr. Brown for starting me on the path of solid state. At Caltech I ran into an interesting cast of characters: Tom "Spin Doctor" McGill, who gave us guidance and support, and always cared more for the students than any other professor on campus. Thank you for giving us freedom in our research and showing us how the real world works. I believe the experience will be more beneficial than any of us realize at midnight the day before a proposal is due while frantically typing in the computer lab. Ron "XPS Guru" Grant, thanks for the hours of discussion and extremely knowledgeable insight into electron spectroscopy that only years of experience can give. Jim "Surface Oxide" McCaldin, a chemistry database three stories high, thanks for all the valuable time tutoring me on the basics of surface and interface chemistry. Ogden "Neat!" Marsh, how can your eyes be good after reading all those papers? Thanks for all the help with devices and experimental set up. Gerry "That's a run-on sentence." Picus, thanks for fixing up our papers and proposals so we don't look too dumb. Tim "Choo-choo" Harris, the best purchasing guy in town. It's been great having you around. You're a wonderful asset to the group, and a great guy, too. There have been a number of students who have added significantly to my graduate experience, and I'd like to thank them for their help: Eric Daniels, for

looking out for me when I was a new member of the group and explaining how devices work, Eric Piquette, for showing me around a vacuum system, and Zvonimir Bandic, for passing on his mastery of processing. To the younger guys I'd like to thank them for helping create a great working atmosphere. Tom, as always, has attracted the best students. Thanks Chubbs, for help on all things theoretical. Special thanks to Core Dog for fixing my computer so often, and always taking time out to help setup an experiment. Rob "volume control" Stri—-matter (I'm sure you know what goes in the blanks.) for working 12 hour days, taking the project places no one imagined, keeping the group lively, and getting no credit for any of it. Eddo "a genuinly amiable guy," thanks for all the hooop and vacuum help. To the newbies, Nealibob and Itchy, welcome to the jungle. You'll do great. Now go find it yourself! To my friends Steffen, Adam, Mona and Jason, thanks for the support. A special thanks for Isaac for always being there for me for so many years.

And finally for Miss Maggie, you're the best, thanks for the RBS and supporting me in a manner in which I plan to become accustomed for many years to come.

Bob Beach

List of Publications

Work related to this thesis has been or will be published under the following titles:

Piezoelectric fields in nitride devices,
R. A. Beach, and T. C. McGill, J. Vac. Sci. Technol. B **17** (4),1753 (1999).

Compositionally dependent band offsets in AlN/Al_xGa_xN heterojunctions measured by using x-ray photoelectron spectroscopy,
R. A. Beach, E. C. Piquette, R.W. Grant, and T. C. McGill, Nitride Semiconductors, MRS proceedings Vol. 482, 775 (1998).

XPS study of oxygen adsorption on (3x3) reconstructed MBE grown GaN surfaces,
R. A. Beach, E. C. Piquette, and T. C. McGill, MRS Internet JNSR 4,U656 (1999).

Fabrication of GaN suspended microstructures,
R.P. Strittmatter, R. A. Beach, T. C. McGill, Appl. Phys. Lett. **17** (12),110 (2001).

Nitride based high power devices: Design and fabrication issues,
Z. Z. Bandić, E. C. Piquette, P. M. Bridger, R. A. Beach, and T. C. McGill, Solid State Electronics **42** (12) 2289 (1998).

Nickel layers on indium arsenide,
C.J. Hill, R. A. Beach, and T. C. McGill, J. Vac. Sci. Technol. B **18** (4),2044 (2000).

Abstract

This thesis describes a number of advancements in the III-V nitride material system achieved at Caltech. Major improvements in optimized growth of III-V nitride materials by radio frequency molecular beam epitaxy are presented. The first GaN based MEMs devices are reported, and their fabrication and characterization are detailed. The growth of InN is discussed, and the morphology and crystal quality are presented. In addition, the switching behavior of the first GaN thyristor is reported. The surface chemistry and band offsets of the nitrides are also investigated using x-ray photoelectron spectroscopy. These investigations are presented in two parts. Part I describes the growth and characterization of III-V nitride materials and includes a discussion of piezoelectric effects in this material system. Part II describes the device related successes mentioned above.

The focus of the second chapter is the description and calculation of piezoelectric phenomena in nitride heterojunctions. The magnitude of the piezoelectric effects in nitride materials is such that entirely new device concepts can be developed. On the other hand, traditional devices are impacted by these polarization fields, and proper accounting for them must be made for device design. Some of these effects are calculated and new devices employing these fields proposed.

The major issues pertaining to MBE growth are discussed in the third chapter. Substrates, nitridation, film nucleation, and the dependence of film quality on growth parameters are investigated by means of AFM, cathodoluminescence, x-ray diffraction, and reflection high energy electron diffraction. It is found that the buffer layer deposition parameters and V/III ratio during subsequent growth are the major factors in determining the resulting films crystal quality.

In addition to growth, x-ray photoelectron spectroscopy has been used to investigate the surface chemistry of column-III nitrides. It was found that the oxidation of GaN was self limiting and did not proceed significantly farther than the first mono-

layer. Many of the core level and valence band maximum positions were determined, as well as the valence band offsets for the AlN/AlGaN system. Part II describes characterization of nitride devices. The switching behavior of a GaN thyristor is described and possible explanations for its behavior investigated. GaN pn and pin diodes are characterized electrically and via electroluminescence. It is found that less than ideal electrical properties of these devices may be related to a high level of deep trap states that produce high levels of leakage current as well as suppress the light emission of these diodes.

Finally, a new method of preferentially etching n type GaN is presented. This technique is extended to the fabrication of GaN MEMs devices, and piezoelectric strain sensors and micropumps fabricated with this technique are characterized.

Contents

List of Figures

List of Tables

Glossary of Acronyms

AC	alternate current
AFM	atomic force microscopy
CAIBE	chemically assisted ion beam etching
CL	cathodoluminescence
DC	direct current
EBIC	electron beam induced current
ECR	electron cyclotron resonance
EL	electroluminescence
FET	field effect transistor
FWHM	full width at half maximum
HEMT	high electron mobility transistor
HFET	heterostructure field effect transistor
HVPE	hydride (or halide) vapor phase epitaxy
HRXRD	high resolution x-ray diffraction
LED	light-emitting diode
MBE	molecular-beam epitaxy
MB	megabyte
MOCVD	metalorganic chemical vapor deposition
PL	photoluminescence
PMT	photomultiplier tube
PN	p-type doped/n-type doped semiconductor junction
RF	radio frequency
RHEED	reflection high energy electron diffraction
SEM	scanning electron microscopy
SIMS	secondary ion mass spectroscopy

SL	superlattice
SPR	solid phase recrystallization
STM	scanning tunneling microscopy
TEM	transmission electron microscopy
UHV	ultra-high vacuum
UID	unintentionally doped
UV	ultraviolet
XPS	x-ray photoelectron spectroscopy
XTEM	cross-sectional transmission electron microscopy
ZB	zincblende
WZ	wurtzite
WBG	wide bandgap

Chapter 1 Introduction

1.1 Introduction to Thesis

This thesis centers around the column III-nitride material system. Development of a RF-MBE growth technology and characterization of material quality, as well as determination of band offsets and surface reactivity are presented in part I. Some previously unexplored devices are discussed in part II of this thesis. These include GaN based thyristors. In addition, a method for producing GaN based MEMs devices is presented, and devices fabricated with this technique are investigated. The two main thrusts of this thesis research were to improve the material quality of material grown by MBE and to expand the arena of nitride based devices to include new devices that take advantage of the unique properties of the nitrides.

1.1.1 General Motivation

The III-V nitride system possesses a wide range of attractive attributes including large direct band gaps, high critical fields for electronic breakdown, and high thermal and chemical stability. With direct band gaps of 1.9eV for InN, 3.4eV for GaN and 6.2eV for AlN, the column III-nitride material system could potentially be fabricated into optical devices that operate from the red well into the ultra violet region of the spectrum. Blue and UV optoelectronic devices are a technologically important region of the electromagnetic spectrum in which semiconductor devices had until recently achieved little success. The ability to emit and detect light of the three primary colors will have tremendous impact on imaging and graphics applications. Light emitting diodes capable of emitting white light are expected to one day replace incandescent light bulbs. The exceptional efficiency of nitride based LED's offers up to a tenfold energy savings compared to conventional light bulbs, while their lifetime of 10^6hours

is 100-1000 times longer than conventional lighting sources.[1] In fact, once installed, these light sources may never need replacing in the lifetime of the home. Another important region of the spectrum occurs around 4.75eV. This is the energy of light absorbed by ozone. Satellite communications employing light of this wavelength would be secure from earth. In addition, the nitrides are expected to exhibit superior radiation hardness as compared to Si or GaAs based devices making them attractive for space based applications.

Research into nitride based devices has primarily focused on these optical applications. Recent successes in producing high power HFETs has led to the realization that nitride materials may also play important roles in high power and high frequency applications. This is primarily due to the large breakdown fields and high saturation velocities of the nitrides. Gallium nitride HFETs are expected to perform in the 10-100 GHz range. This makes nitride materials ideal for microwave switching as well as emitters for cellular phone applications. In addition, AlGaN/GaN HFETs have shown the capability to switch high voltages, above 100V. [2] This may make GaN devices ideal for analog front ends in analog to digital converters. Optoelectronic devices such as LEDs, UV detectors, and laser diodes are currently being fabricated and marketed, and heterojunction field effect transistors are well on their way to commercialization. This insures that the trend toward higher quality material and better processing technology will continue. Expanding the range of devices employing nitride materials may result in added benefits similar to those achieved in the optoelectronic and microwave applications discussed above.

An obvious application of GaN's high critical fields that has yet to be investigated with significant success is high power switching and rectifying. Nitride materials have the potential to improve power management systems from electric motor drives in heavy industry to power grid control for the electric power industry. High critical fields allow thinner devices and higher doping for the same standoff voltage. This leads to lower on state voltage drop, less wasted power, and lower cooling requirements, all of which are extremely beneficial for power management applications.

1.1.2 Scope of Investigations

Although the surge in interest in GaN during the last decade has resulted in amazing improvements in the understanding of both the material properties and growth dynamics of nitrides, significant hurdles still remain for the continued development of this material system. The lack of a lattice matched substrate for growth, and the extreme difficulties in producing GaN by conventional bulk growth techniques requires heteroepitaxial growth of nitrides on non ideal substrates. This causes a number of difficulties for producing high quality material with low defect densities. Historically GaN has been grown predominantly by near equilibrium vapor phase techniques such as MOCVD or HVPE. Many recipes for improving the crystal quality of nitride materials grown by these techniques have been developed. Comparatively little work has been done, however, employing the far from equilibrium growth method of molecular beam epitaxy. Many of the techniques developed to produce high quality GaN using MOCVD have led to marginal improvements, or even deterioration of the crystal quality when employed during MBE growth. The progress of MBE as a viable growth technology for column-III nitrides requires a reinvestigation of growth dynamics for this much different method of crystal growth. To this end, we have investigated the effects of growth stoichiometry in both the nucleation and main layer deposition stages of growth to determine the optimal parameters for nitride growth employing RF-MBE.

Incorporating nitride materials into more diverse device structures will further improve the attraction of this material system for many applications. The nitrides large direct band gap has been exploited to produce optical devices in the blue and UV parts of the spectrum, and the high saturation velocities and large two-dimensional electron gas concentrations at the AlGaN/GaN interface have been used to produce high frequency high power HFET transistors. Nitride materials have also been shown to possess very high critical fields for breakdown. Very little work has been done, however, to extend the applications of nitride materials in the direction of high power devices. The lifetimes of minority carriers have been shown to be long enough to

produce bipolar transistor devices,[3] and recently the first npn and pnp transistors were demonstrated.[4, 5] Extending this transistor success to include high voltage switching by employing a thyristor structure has not been reported thus far. We have fabricated such structures and their current voltage characteristics are presented here.

The bulk of nitride research has focused on GaN and ternary materials with low alloy fractions of aluminum and indium. Indium nitride is by far the least studied of the nitride materials. Calculations indicate that InN has the highest saturation velocity of the nitrides,[6] and its band gap of 1.9eV is still quite large compared to conventional materials such as Si or GaAs. The growth of this material has been hampered by many of the same difficulties as GaN, however, and much less research has been directed at obtaining high quality material. We have investigated growth of this material for possible integration with Si employing CeO_2 interlayers. The use of CeO_2 is employed to overcome the large lattice mismatch between Si and InN.

Microelectromechanical devices have recently advanced to the point of commercialization in applications ranging from airbag control in secondary restraining devices to engine monitoring in self tuning engines. Production of MEMs devices in the nitrides would expand the applicability of these devices to high temperature and caustic environments given GaN's thermal and chemical stability. In addition, nitride MEMs devices could take advantage of the large piezoelectric effects in the nitride material system. We have developed a method for producing GaN MEMs structures. This technique is presented here and some MEMs devices are characterized.

1.2 Summary of Results

Only recently has RF-MBE been investigated as a means of producing column-III nitride materials, and still requires significant development of the basic aspects of nitride growth using this technique. This thesis includes investigations into the parameters that influence crystal quality when employing RF-MBE. AlN, GaN, InN, and AlGaN were grown using radio frequency plasma assisted molecular beam epitaxy. As is discussed in chapter 3, growth of GaN can be broken down into two parts.

The first is preparation of the surface to be grown on. This includes nitridation of the substrate, if sapphire is to be used as the substrate, and nucleation layer deposition. These two steps define the surface template the subsequent growth will see when main layer deposition is initiated. The second part is the deposition of the main layer that will constitute the bulk of the material deposited. We have investigated stoichiometry and temperature effects on these two stages of growth. It was found that stoichiometry during all stages of growth was paramount in determining crystal quality. Unlike other III-V materials grown by MBE, GaN can not be grown under group V rich conditions without rapid degradation of the surface morphology. In addition, excessive group III conditions results in metal droplet accumulation. These two restrictions narrow the acceptable window of growth conditions that can produce good material. We have determined that optimal growth conditions require slightly metal rich conditions for both buffer layer and main layer deposition. Buffer layer temperature had some effect on crystal quality, but good material could be grown employing almost any temperature buffer. The predominant effect of lower buffer layer temperatures was a significant narrowing of the ideal stoichiometric conditions. Given the low rate of metal reevaporation at lower temperatures, metal droplet condensation became difficult to avoid, while metal poor conditions resulted in higher pit densities in the resulting films. Nitrogen rich conditions during main layer growth also lead to high levels of yellow luminescence in cathodoluminescence spectra taken after growth completion. We have used reflection high energy electron diffraction (RHEED) to observe the transition from metal rich to nitrogen rich growth conditions during growth interrupt, and determined that optimal growth conditions result in an excess layer of metal on the surface. The quantity of metal for optimal growth is observed to coincide with a time for the RHEED to brighten after shuttering the metal source of $\sim$5-10s. This allows stoichiometry to be adjusted at the beginning of growth to achieve proper flux ratios for the remainder of growth.

Gallium nitride bipolar devices were fabricated and characterized. We were able to show bistable switching of a pnpn GaN thyristor. We observed unexpected behavior of these devices in the form of persistent conductivity. Once switched into the on state

by applying a forward bias greater than the forward breakover voltage, these devices remained in the onstate even after removal of any forward bias. In addition we found that this behavior was non-destructive and temperature sensitive. Thermal cycling of the device returned it to its original forward blocking mode. It is proposed that this behavior is associated with the persistent conductivity observed in GaN, and may be due to ionization of deep traps within the base layer, resulting in a pinned on state until thermal cycling. GaN pn and pin diodes were grown and processed as another method of characterizing the material quality our GaN. Electroluminescence revealed a high level of radiative deep levels within our material. Commensurate with the high level of yellow luminescence was significant leakage in reverse bias, and nonideal current voltage curves that indicated a high level of trap states within the gap.

Indium nitride was investigated as a material for integration with Si. InN was grown on (111) Si employing CeO^2 intermediary layers, as well as on GaN. The use of the cubic materials resulted in the stabalization of the cubic phase of InN. The morphology of InN grown on GaN was similar to GaN morphology with mountainous areas of $\sim$100nm hieght. Growth of CeO^2 resulted in hexagonal crystalites of $\sim 0.5\,\mu$m in diameter. Dopent selective photoelectrochemical (PEC) etching of n-type GaN was extended to the fabrication of novel GaN MEMs devices including micropumps and piezoresistive pressure sensors. Peristaltic compression of the undercut channels in these pumps was observed and assigned to a joule heating mechanism. The MEMs based pressure sensors showed $\Delta R/R$ values in the 1-2x10^{-4} range. This is the first reported use of PEC for production of GaN based MEMs devices and may open an entirely new area of devices utilizing nitride based materials.

1.3 Outline of Thesis

This thesis is divided into two parts. The first part describes investigations into the growth of column-III nitride materials by RF-MBE and the subsequent characterization of those materials by various methods including atomic force microscopy, x-ray diffraction, cathodoluminescence, and x-ray photoelectron spectroscopy. The second

half of this thesis deals with fabrication and characterization of devices including Schottky diodes, pn and pin diodes, thyristors, and MEMs devices.

Chapter 2 discusses the physical and electrical properties of column-III nitrides and presents calculations pertaining to spontaneous and piezoelectric polarizations. Some effects due to these fields are presented, and methods for incorporating the effects of these polarization fields into device design are examined. Chapter 3 describes the growth of nitride materials carried out here, and presents methods for optimizing growth conditions to produce improved materials. In chapter 4 XPS investigations into the surface chemistry of nitrides is presented, and some material parameters such as core level positions and valence band offsets are measured. Chapter 5 contains characterization of a number of devices. The first section presents results on the characterization of the electrical properties of a GaN thyristor. The second section investigates the electrical properties of GaN pn junctions. Chapter 6 describes the fabrication and characterization of GaN MEMs devices utilizing a dopent selective photoelectrochemical etch technique.

Bibliography

[1] S. Nakamura and G. Fasol, *The Blue Laser Diode* (Springer, Berlin, 1997).

[2] X. Dang, R. Welty, D. Qiao, P. Asbeck, S. Lau, E. Yu, K. Boutros, and J. Redwing, Elec. Lett. **35**, 602 (1999).

[3] Z. Bandic, P. Bridger, E. Piquette, and T. McGill, Solid State Elec. **44**, 221 (2000).

[4] B. Shelton, J. Huang, D. Lambert, T. Zhu, M. Wong, C. Eiting, H. Kwon, M. Feng, and R. Dupuis, Elec. Lett. **36**, 80 (2000).

[5] A. Zhang, G. Dang, F. Ren, J. Han, A. Baca, R. Shul, H. Cho, C. Monier, X. Cao, C. Abernathy, and S. Pearton, Appl. Phys. Lett.**76**, 2943 (2000).

[6] S. O'Leary, B. Foutz, M. Shur, U. Bhapkar, and L. Eastman, J. Appl. Phys.**83**, 826 (1998).

Part I

Growth and Characterization

Chapter 2 III-Nitride Properties

Group III-nitrides have attracted considerable attention recently due to a number of their exceptional physical and electrical properties. The primary stimulation for research into nitride materials comes from their large direct band gaps and their physical robustness compared to other semiconducting materials. Advances in growth of GaN have allowed significant clarification of it physical and electrical properties in the last decade. This has lead to the realization of blue LEDs and lasers [1] as well as high power Schottky and pn diodes.[2] In addition, advantageous use of the piezoelectric behavior of this material system has led to high power HFETs operating in the gigahertz frequency range.[3] This chapter discusses the physical and electrical properties of the nitrides and presents some calculations of the magnitude and effects of piezoelectricity on nitride devices.

2.1 Physical Properties

The natural structure of AlN, GaN, and InN is wurtzite, a hexagonal structure defined by the edge length, a, of the basal plane hexagon and the height, c, of the hexagonal prism. The structure consists of alternating hexagonal planes of Ga, Al, or In and N with a stacking sequence of ABAB, with the c axis perpendicular to the hexagonal planes. The positive c direction is defined by convention to point from the cation to anion along the cation to anion bond that is perpendicular to the basal plane. This is depicted schematically in figure 2.1. With direct band gaps of 1.9eV for InN, 3.4eV for GaN and 6.2eV for AlN, the column III-nitride material system could potentially be fabricated into optical devices that operate from the red well into the ultra violet region of the spectrum. Blue and UV optoelectronic devices are a technologically important region of the electromagnetic spectrum in which semiconductor devices had until recently achieved little success. The ability to emit and detect light of the three

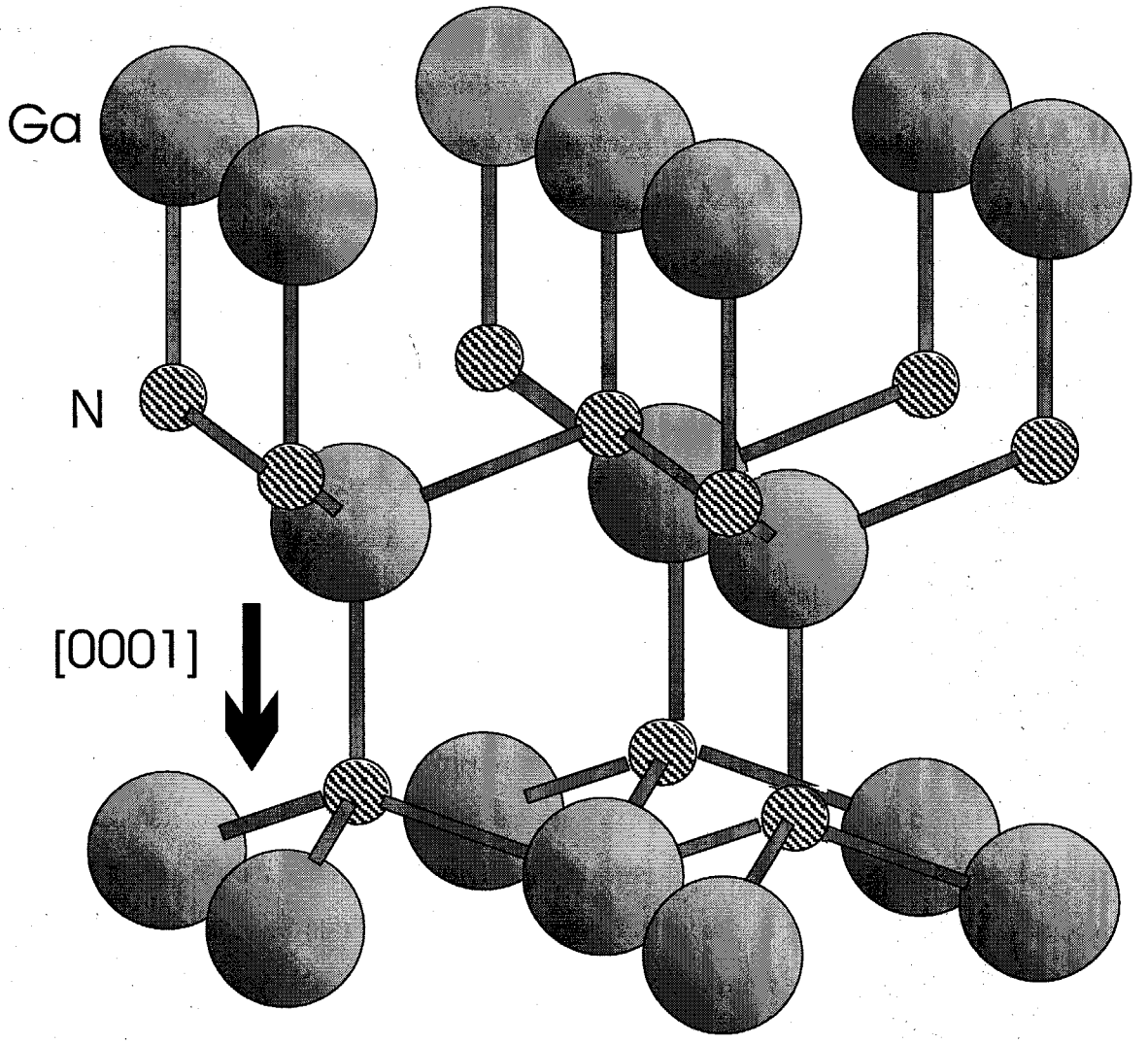

Figure 2.1: Schematic of wurtzite GaN.

primary colors will have tremendous impact on imaging and graphics applications. Another important region of the spectrum occurs around 4.75eV. This is the energy of light absorbed by ozone. Satellite communications employing light of this wavelength would be secure from earth. In addition, the nitrides are expected to exhibit superior radiation hardness as compared to Si or GaAs based devices making them attractive for space based applications.

GaN was first synthesized by Johnson et. al.[4] ,who noted "Gallic nitride is an exceedingly stable compound." This chemical and thermal stability along with gallium nitrides large band gap makes it an attractive candidate for applications in

caustic and high temperature environments. This same robustness, however, makes processing of nitride devices exceedingly difficult. There have been many reports of GaN's resistance to standard wet etching techniques [5] and has led most researchers to employ various ion milling techniques, such as Reactive Ion Etching (RIE) and Chemically Assisted Ion Beam Etching (CAIBE), for device fabrication. This type of physio-chemical etching produces a number of detrimental effects for contacting the resulting material. It has been shown that damage to the surface caused by RIE lowers the Schottky barrier height for GaN Schottky diodes [6] and that Schottky diodes with etched mesas suffer from increased reverse leakage current unless extra processing steps are employed to passivate the mesa walls.[7] In addition, contacting buried p-type layers is made difficult by the introduction of compensating n-type defects at the exposed surface.[8] A number of schemes for reconditioning the exposed surface after etching have been developed with varying degrees of success. Future development of device processing will have to address this fundamental difficulty. GaN's lattice constants have been measured and their values determined to be a=3.189 Å and c=5.185 Å. Maruska and Tietjen [5] performed measurements over a temperature range of 300-900 K and observed a mean thermal expansion coefficient of $\Delta a/a=5.59x10^{-6}$/K. Sichel and Pankove[9] measured the thermal conductivity of GaN and obtained a room temperature value of 1.3W/cm K, in good agreement with the predicted value of 1.7W/cm K.[10]

Aluminum nitride has many of the same physical attributes as GaN such as its hardness, thermal conductivity, and resistance to high temperature and caustic environments. AlN's large band gap has led to investigation of its potential as an insulating material for GaAs and InP devices, and its large piezoelectric constants have attracted attention for surface acoustic wave devices. Primarily, however, interest in AlN has stemmed from its alloys with GaN which may permit optoelectronic devices that operate in the UV. The currently accepted values of AlN's lattice constants are a=3.112 Å and c=4.982 Å.[11] The room temperature thermal conductivity of AlN is ~2W/cm K,[12] and its coefficient of thermal expansion is $\Delta a/a\sim4x10^{-6}$/K and $\Delta c/c\sim5x10^{-6}$/K.[13]

Indium nitride is the least studied of the nitride materials. Its band gap of 1.9 eV is in a range currently achievable by other more mature material systems, thus it lacks the motivating factor that has spurred research in aluminum and gallium nitride. The lack of a suitable substrate as well as other materials related difficulties have resulted in few reports of single crystal material. Correspondingly most measurements of its physical parameters have been performed on highly conductive polycrystalline material, and a consensus has not been reached on many of its properties. Table 2.1 gives some of the physical parameters of the nitrides quoted in the literature.

The thermal stability of the nitrides is a critical parameter in terms of both high temperature device applications as well as understanding the surface stability and decomposition rate for optimization of growth parameters. Figure 2.2 shows the partial pressure of mass 28 amu (N_2, CO, C_2H_4) recorded as samples of nitride materials were heated in vacuum.[18] This data shows a rapid decomposition of material beginning around 630, 850, and 1040 °C respectively for InN, GaN, and AlN. The rate of nitrogen evolution Φ(N)is equal to the decomposition rate, and the slope of ln(Φ(N)) vs. 1/T gives the effective activation energy of decomposition in vacuum. The activation energy was determined to be 3.5eV (336 kJ/mol), 3.9 eV (379 kJ/mol), and 4.3 eV (414 kJ/mol) for InN, GaN, and AlN respectively. The decomposition rate was determined to be one monolayer per sec at 795, 970, and 1050 °C. This gives an estimate for temperature limits for high temperature or high power devices, and indicates that protective measures may be necessary for nitride devices in high temperature applications.

2.2 Electrical Properties of the Nitrides

Interest in optoelectronics has been the primary motivation for research into nitride materials. Simple applications such as traffic street lamps of the proper color is estimated to be a billion dollar a year industry. As shown in figure 2.4, the nitrides span the entire visible range. The growth of high quality material, however, has not been a trivial endeavor. Attempts to produce device quality material have been

	AlN		GaN		InN	
Band Gap (eV)	6.20		3.39		1.89	
E_g Temp. Coef. (10^{-4} eV/K)			-6.0		-1.8	
Lattice Constant (A) a=	3.112		3.189		3.548	
c=	4.982		5.185		5.760	
E_B(M-N)(eV)	2.88		2.20		1.98	
Therm. Expans. Coef. (10^{-6}/K) $\Delta a/a$	4.2		5.59			
$\Delta c/c$	5.3		3.17			
Thermal Cond.	2.0 W/cm K		1.3			
Dielectric Constant $\varepsilon(0)$	8.5		9.5			
$\varepsilon(\infty)$	4.68		5.35			
Elastic Moduli	Exp.	Calc.	Exp.	Calc.	Exp.	Calc.
C11 (GPa)	345	396	390	367	190	223
C12	125	137	145	135	104	115
C13	120	108	106	103	121	92
C33	395	373	398	405	182	224
C44	118	116	105	95	10	48
Bulk Modulus	201	207	210	202	139	141

Table 2.1: Properties of Column-III Nitrides at 300K.

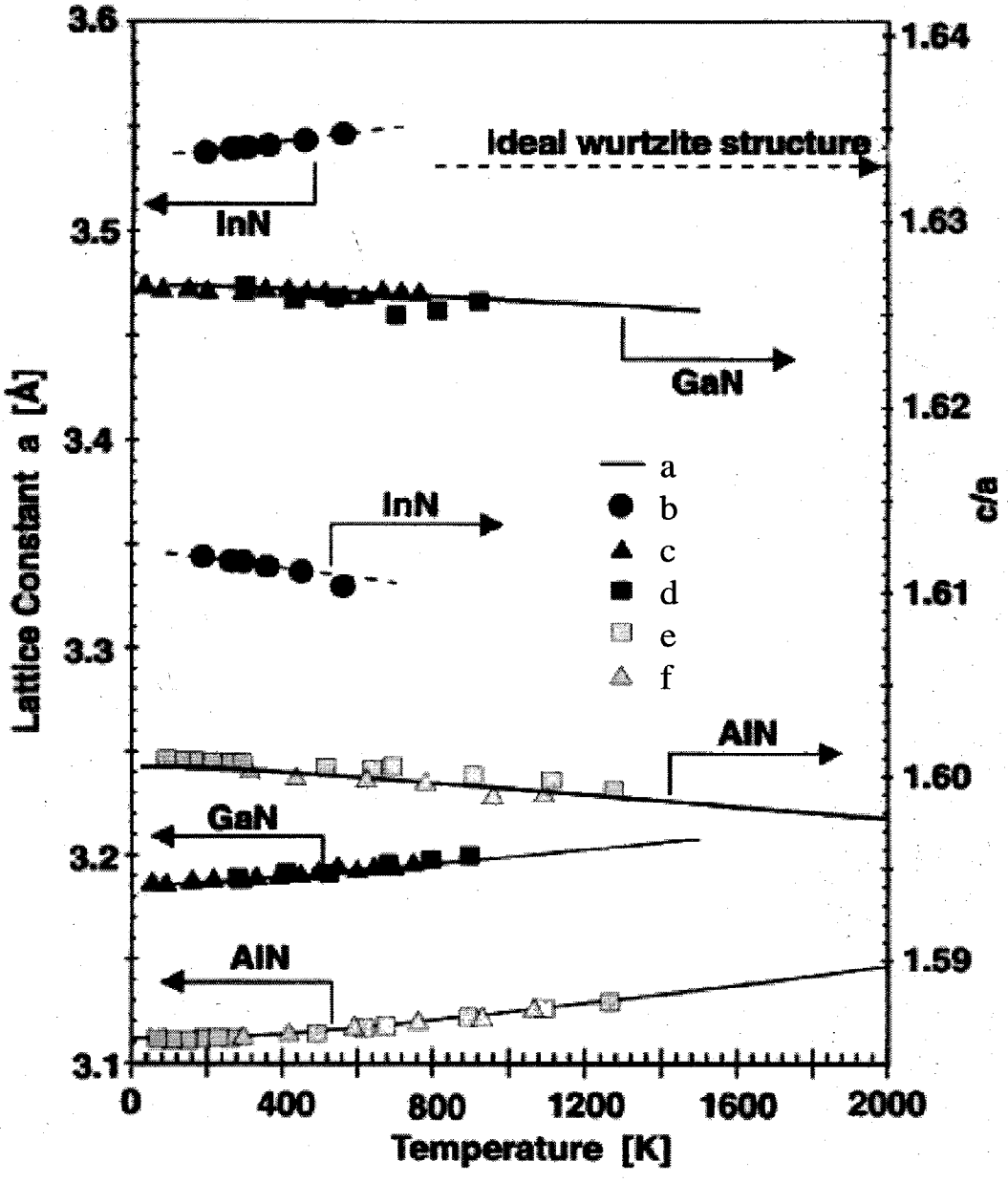

Figure 2.2: Lattice constants of the nitrides as a function of temperature.a)[14]b)[15]c)[16]d)[5]e)[17]f)[13]

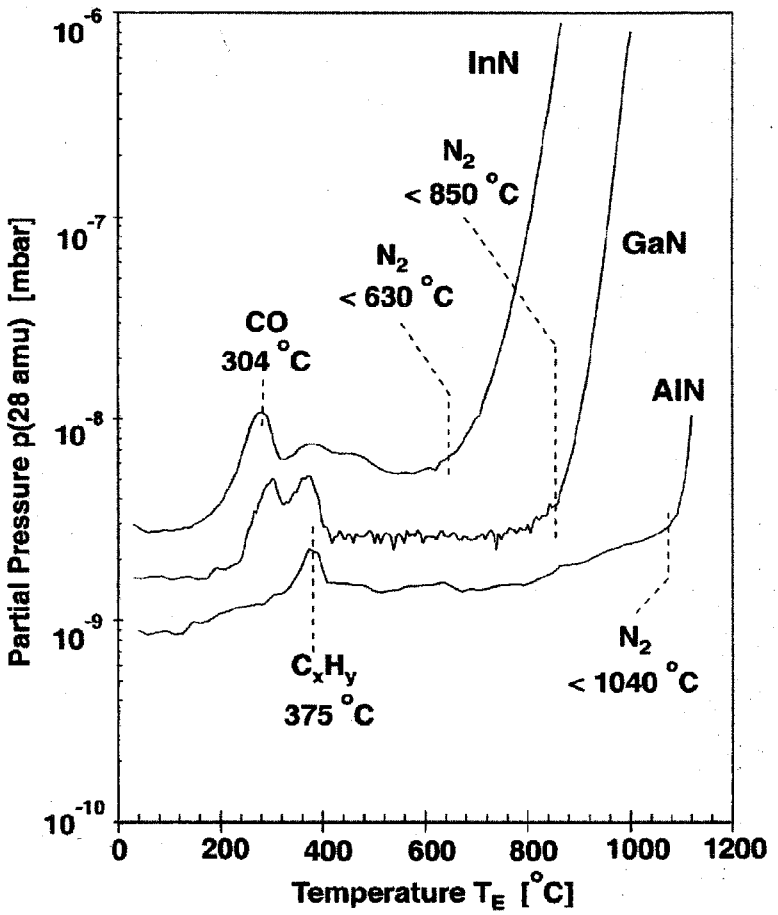

Figure 2.3: Partial pressure of nitrogen during thermal annealing of InN, GaN, and AlN in vacuum. [18]

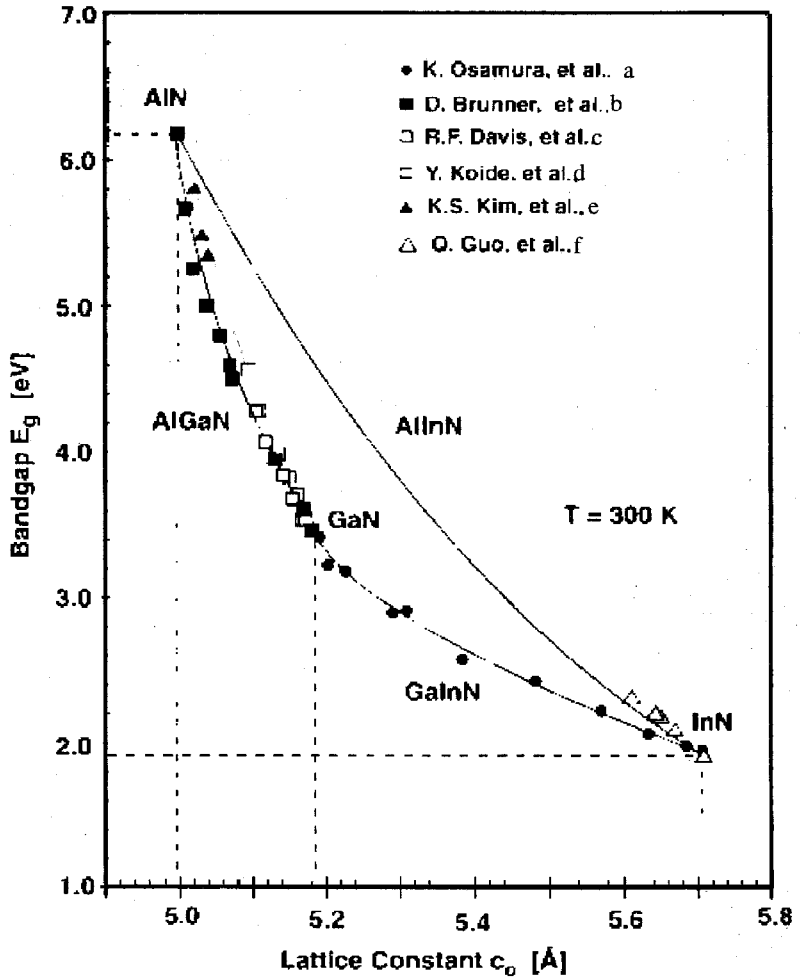

Figure 2.4: Band gap of column III Nitrides verse lattice constant c. a)[19] b)[20] c)[21] d)[22] e)[23] f)[24]

under way for over 40 years, yet GaN based devices have only recently advanced to the point of commercialization, and AlN and InN are still in their infancy in terms of understanding their growth dynamics.

Control of the electrical properties and doping in the nitrides remains a significant obstacle to devices, particularly bipolar devices. All unintentionally doped GaN has a residual n type doping with the best samples showing carrier concentrations $\sim 10^{16}/cm^3$. No impurity has been shown to exist in high enough quantity to account for this doping, and the background doping has generally been attributed to native defects and nitrogen vacancies within the material. p-type material has been achieved

in both MBE and MOCVD material by doping with Zn or Mg.[25] Lower quality material, however, suffers from compensation and results in highly resistive material. In addition, the activation energy of all acceptors are quit large, with Mg being the lowest with a thermal ionization energy of 155-165 meV.[26] Some scattered reports of both n and p doping of AlN can be found in the literature, however, most material is highly resistive and most often insulating. On the other extreme, undoped InN is highly n-type with residual doping $\sim 10^{18}/cm^3$ or higher. It should be noted, however, that GaN suffered from a similar level of residual doping when first investigated, and only through extensive efforts to grow high quality material was this overcome. n-type GaN with mobilities of greater than 800 cm^2/Vs has been reported by a number of authors. p-type material results in hole mobilities on the order of 10 cm^2/Vs. The low mobilities of Mg doped material may be due to the high doping concentrations required to produce p-type material. The large activation energy of Mg in GaN requires that doping levels of $10^{20}/cm^3$ are needed to produce carrier concentrations of $10^{18}/cm^3$. While lower doping densities often results in compensated highly resistive material. The lowest intrinsically doped InN was grown by Tansley and Foley. Their sample showed a room temperature electron concentration of $5x10^{16}/cm^3$ and a room temperature mobility of 2700 cm^2/Vs and a maximum value of 5000cm^2/Vs at 150 K.[27] Table 2.1 lists some of the electrical properties of the nitrides. Included in table 2.1 are the piezoelectric coefficients of the nitrides. Wurtzite is the structure with the highest symmetry compatible with the existence of spontaneous polarization, and the III-Nitrides are predicted to have very large spontaneous polarization fields. In addition to the static polarization associated with the wurtzite crystal structure, piezoelectric fields are produced in strained heterojunction structures. The effects produced by spontaneous and piezoelectric polarizations are discussed further in the next section.

2.3 Spontaneous and Piezoelectric Polarizations

Piezoelectricity has been studied extensively for applications in precise control of positioners and vibrators for atomic force microscopy and recently has been employed for nanometer control of optics in integrated telescopes such as the Keck telescope on Monokea. In addition piezoelectric effects in GaAs have been studied for their influence on recombination and stark shifts in (111)AlGaAs/GaAs [28, 29] quantum wells as well as for applications in strain sensors employing AlGaAs HFETS.[30] These piezoelectric effects allow for interesting possibilities in strain field engineering. It has been shown that the AlGaInN system possesses extremely high piezoelectric constants [31](about 7 times larger than GaAs). This has resulted in numerous papers cataloging piezoelectric effects in nitride structures. These include the piezoresistive effect in GaN/AlN/GaN semiconductor-insulator-semiconductor (SIS) structures,[32] in which small deformations of the SIS structure lead to changes in the in-plane resistance. A similar effect is seen in AlGaN/GaN heterojunction field effect transistors (HFETs). [33] In this case the change in spontaneous polarization and strain induced piezoelectric polarization induce a compensating 2-dimensional electron gas (2DEG) at the AlGaN-GaN interface.[33, 34, 35] Piezoelectric fields have also been shown to effect the optical properties of InGaN/GaN and GaN/AlGaN quantum wells. The strain induced electric field tilts the conduction and valence bands within the well, resulting in charge separation and increased recombination times as well as a red shift in the emission verse absorption spectrum.[36, 37, 38] In the last few years, substantial advances in growth of nitrides has lead to improvements in the structural and electronic properties of GaN and its ternary alloys. This has resulted in major advances in blue-green light-emitting diodes and lasers as well as HFET power devices. To further improve the performance of these devices, the effects of piezoelectricity must be accounted for. In addition, the use of piezoelectric fields can result in a number of interesting devices such as piezoelectrically enhanced Schottky diodes and photodetectors. This chapter discusses the origin of piezoelectricity and presents calculations of the fields produced in various nitride based heterostructures.

2.3.1 Outline of section

Section 2.3.2 discusses the basic principles of spontaneous polarization and piezoelectricity and presents basic calculations of piezoelectric fields in nitride structures. Section 2.3.3 investigates the effects these fields have on devices and presents some novel device designs that take advantage of polarization fields in the nitrides.

2.3.2 Polarizations in nitride materials

The natural structure of AlN, GaN, and InN is wurtzite, a hexagonal structure defined by the edge length a of the basal plane hexagon and the height c of the hexagonal prism. The structure consists of alternating hexagonal planes of Ga, Al, or In and N with a stacking sequence of ABAB, with the c axis perpendicular to the hexagonal planes. The positive c direction is defined by convention to point from the cation to anion along the cation to anion bond that is perpendicular to the basal plane. This is depicted schematically in figure 2.5.

Wurtzite is the structure with the highest symmetry compatible with the existence of spontaneous polarization, and the III-Nitrides are predicted to have very large spontaneous polarization fields. In addition to the static polarization associated with the wurtzite crystal structure, piezoelectric fields are produced in strained heterojunction structures. Piezoelectricity is the result of two processes. One is the rearrangement of electronic states in the crystal. The other is displacement of charged constituents within the lattice. Due to the semi-ionic nature of the nitrides, displacement of charged constituents is the largest contributor to the piezoelectric response in the AlGaInN system. A quantitative description of the strain induced polarization is given by;

$$P_i = \sum_j e_{ij}\varepsilon_j \tag{2.1}$$

We conform to the established practice when transforming tensors to the more concise matrix notation. For a good explanation of the placement of various factors of 2, such as ε_6=2 ε_{12}, refer to Nye.[39] Here, P_i is the polarization in the i direction, ε_j is the

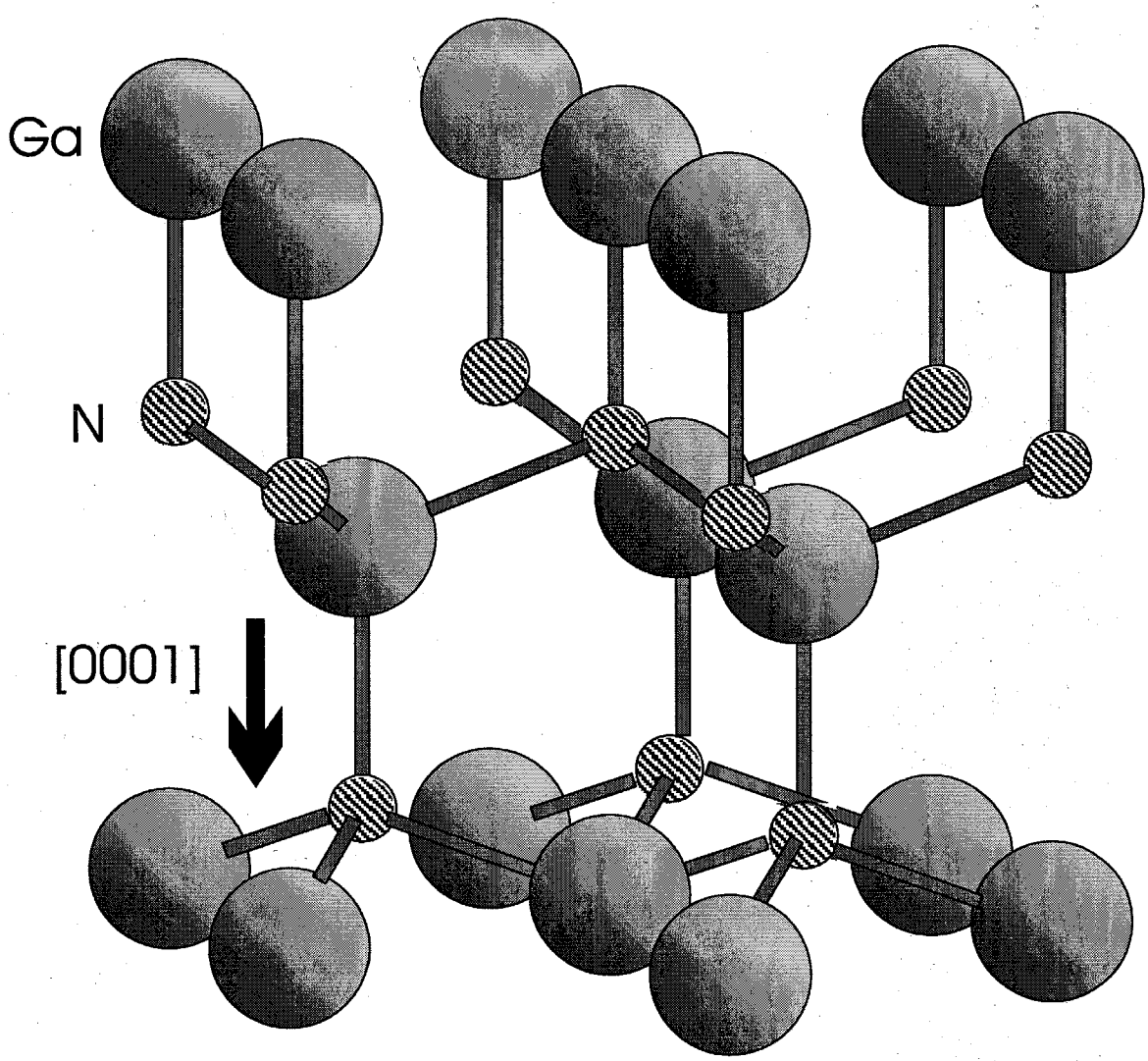

Figure 2.5: Schematic of wurtzite GaN.

j component of strain, and e_{ij} is the ij component of the piezoelectric tensor. The strain generated in psuedomorphic epilayers is determined by the lattice mismatch for the in-plane strain and energy minimization for the perpendicular component of strain. With the 3-axis set as the growth direction, e_1 and e_2 are given by;

$$\varepsilon_{1,2} = \frac{a_s - a_l}{a_l} \tag{2.2}$$

Here, a_s (a_l) is the substrate (epilayer) lattice constant. The lattice constants were assumed to follow Vegard's law. The strain energy, U, is given by;

$$U = \frac{1}{2}\sum_{ij} C_{ij}\varepsilon_i\varepsilon_j \tag{2.3}$$

The C_{ij}'s are the elastic constants of the strained layer. The perpendicular component of strain is determined by minimizing this strain energy. The piezoelectric polarization can then be calculated using equation 2.3. For all alloys a linear interpolation of piezoelectric constants and elastic moduli has been used. Due to the lack of experimental data for bulk InN, we have used the elastic coefficients of GaN in place of InN. We have used the spontaneous polarization and piezoelectric constants of reference [31], along with the elastic coefficients of references [40] and [41]. The spontaneous polarization of the bulk is assumed to be canceled by charging of surface states. If this were not the case, an enormous field, on the order of a few MV/cm, would be present across the entire sample. The effect of changes in spontaneous polarization from the bulk to epilayer are accounted for in these calculations by assuming a linear relationship between alloy fractions and spontaneous polarizations. Figure 2.6 shows the calculated fields generated in InGaN/GaN, GaN/AlGaN, and AlGaN/GaN epilayers for undoped structures.

The direction of these fields depends on the polarity of the growth. For InGaN grown on GaN and GaN grown on AlGaN, there is a compressive strain in the epilayer. This results in a piezoelectric field in the $[000\bar{1}]$ direction. For AlGaN grown on GaN the strain is tensile, and results in a piezoelectric field in the [0001] direction.

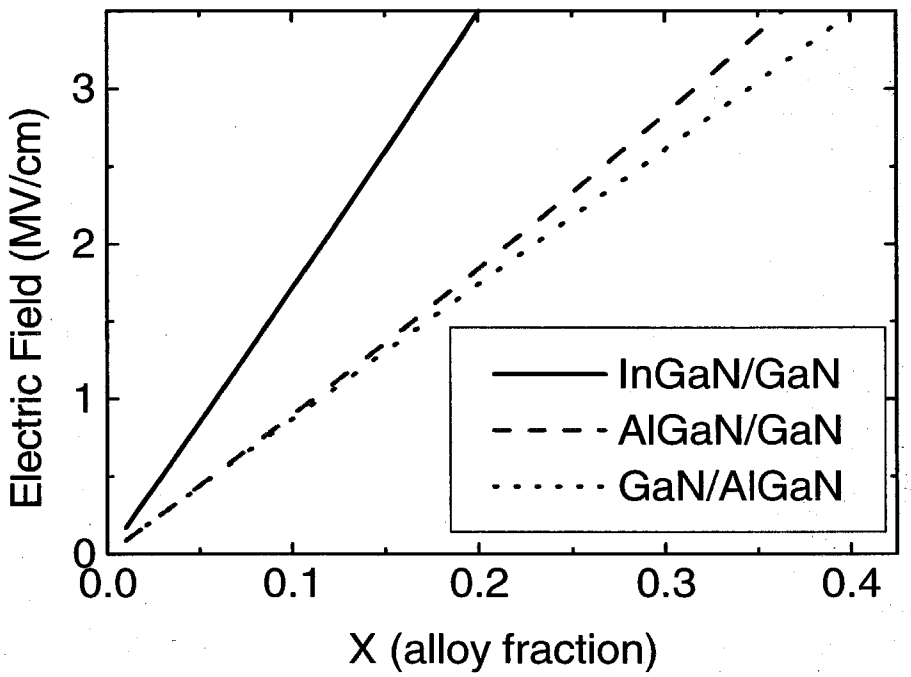

Figure 2.6: Comparison of fields in III-N heterostructures.

The effect of bulk spontaneous field cancellation is to increase the electric field for GaN/AlGaN and AlGaN/GaN and to decrease the field for InGaN/GaN. It is interesting to note the similarities in electric field for the AlGaN/GaN and GaN/AlGaN structures. From a quick look at the piezoelectric coefficients, one would expect the AlGaN/GaN structure to have a 20% larger field than the GaN/AlGaN structure due to AlN's larger piezoelectric coefficient. This is not the case, however. The change in spontaneous electric field has the same magnitude, but opposite sign, for both structures. Although not shown, the spontaneous contribution represents 2/3 of the resulting field. This results in the closely matched curves for AlGaN/GaN and GaN/AlGaN in figure 2.6. The electric field is given approximately by E=-18.6MV/cm x (-3.0MV/cm x) for In_xGa_xN/GaN (GaN/Al_xGa_xN). The negative sign indicates an electric field in the [000$\bar{1}$] direction. This is toward the substrate in metal-organic chemical vapor deposition (MOCVD) and halide vapor phase epitaxy (HVPE) grown samples.[42] Very good agreement between calculated and observed electric fields was obtained for the GaN/AlGaN structures when screening due to doping was incorporated into the calculations. For a 100 Å GaN/$Al_{0.15}$ $Ga_{0.85}N$ single quantum well, a field of 0.40 MV/cm was calculated while measurements employing photoluminescence resulted in a value of 0.42 MV/cm.[37]

2.3.3 Polarization fields in nitride devices

Heterojunction Field Effect Transistors

Nitride based heterojunction field-effect transistors have emerged as attractive candidates for high power devices operating at microwave frequencies. These devices benefit from a high density two-dimensional electron gas that arises at the AlGaN-GaN interface. This 2DEG has been shown to arise from a large electric field present in the strained AlGaN barrier layer.[34] The expected 2DEG density for a Schottky/AlGaN/GaN structure is given by;

$$n_{2d} = \frac{\sigma_p}{e} - \frac{\varepsilon_{AlGaN}}{de^2}(e\phi_b + E_F - \Delta E_c) + 0.5N_d d \qquad (2.4)$$

Here, σ_p is the polarization charge at the AlGaN-GaN interface caused by the change in spontaneous polarization and the piezoelectric polarization. ε_{AlGaN} is the dielectric constant of the AlGaN layer, N_l is the doping density in the AlGaN layer, and d is the AlGaN layer thickness. We have used a value of 1.0 eV for the Schottky barrier height (ϕ_b) of the contact on GaN. We have assumed an increase in Schottky height for AlGaN identical to the conduction band offset, thus reducing $e\phi_b$-ΔE_c to $e\phi_{GaN}$. E_F is the Fermi level with respect to the conduction band edge at the AlGaN/GaN interface. We have used a value of 0.1 eV for E_F and $10^{18}/cm^3$ for N_l in these calculations. Figure 2.7 shows the results of this calculation for variable Al content in the AlGaN layer, and compares the results to experimental measurements found in the literature.[35, 43]

The thickness of the AlGaN layer is also an important parameter in these HFETs. Figure 2.8 shows the dependence of the 2DEG density on AlGaN barrier thickness for three Al contents. As can be seen in the figure, a distinct role off occurs in the 2DEG density at ~150 Å. After this point, the electron density begins to flatten out with little increase for added thickness.

Quantum Wells

Light emitting diodes based on GaN, AlGaN, and InGaN have already been produced and marketed with great success. [44] It has been well documented that these quantum well structures possess a large red-shift in the emission versus absorption spectrum. This has been shown to result from the piezoelectric fields generated by strain in the well layer.[38] These piezoelectric fields result in charge separation and decreased oscillator strength for the quantum well structure, resulting in decreased efficiency for light emitting devices. Advantageous use of piezoelectric fields has resulted in improved device performance for HFET's employing a strain generated 2D electron gas.[34, 35] A similar use of strained field engineering has yet to be investigated for light emitting quantum wells. Here we incorporate the effects of doping on the fields present in the quantum well, and present a method for determining the most advantageous doping profiles for light emitting devices. Due to the detrimen-

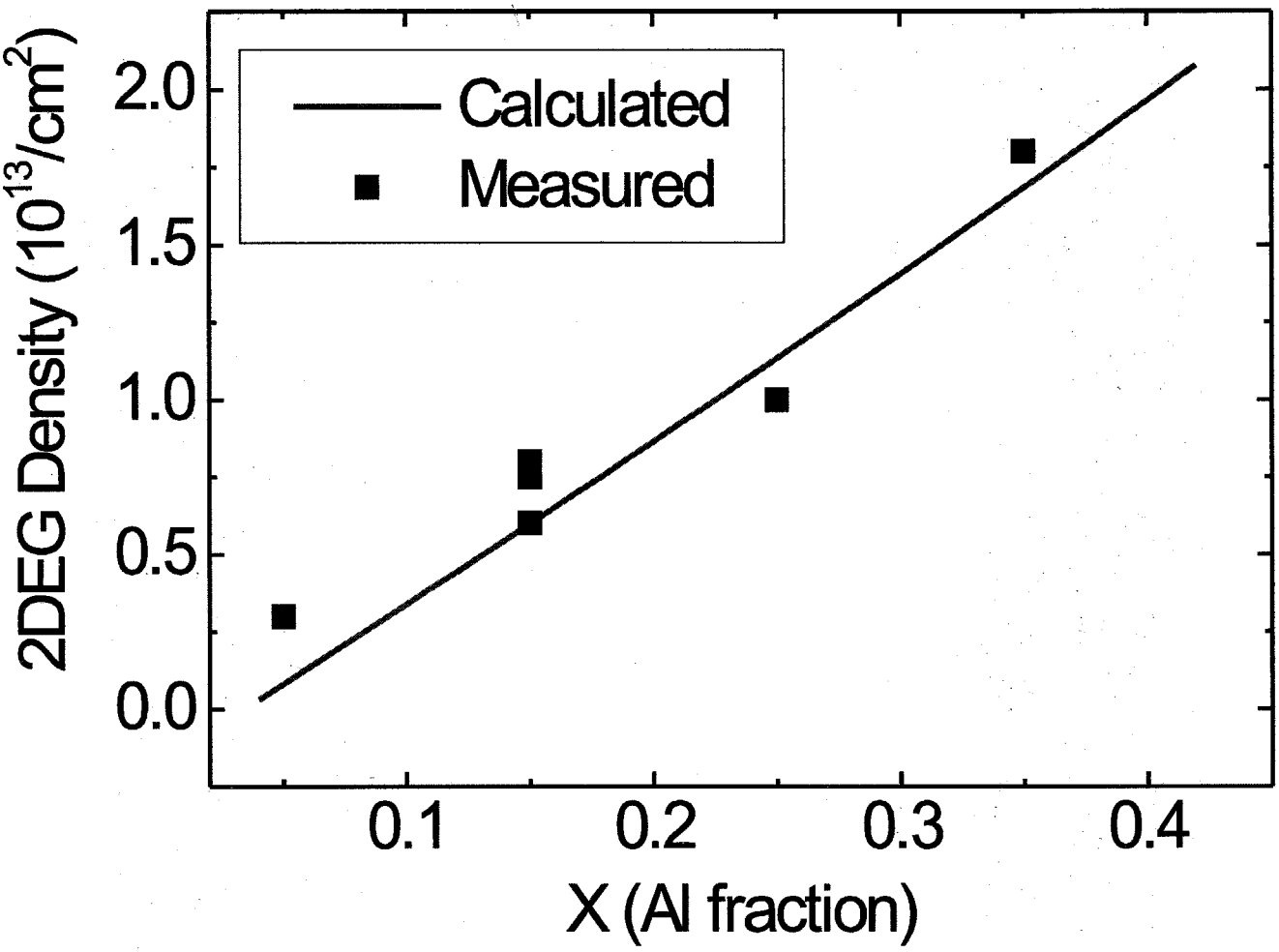

Figure 2.7: Comparison of calculated and measured 2DEG densities for AlGaN(300 Å)/GaN HFETs. Data from references [35] and [44]

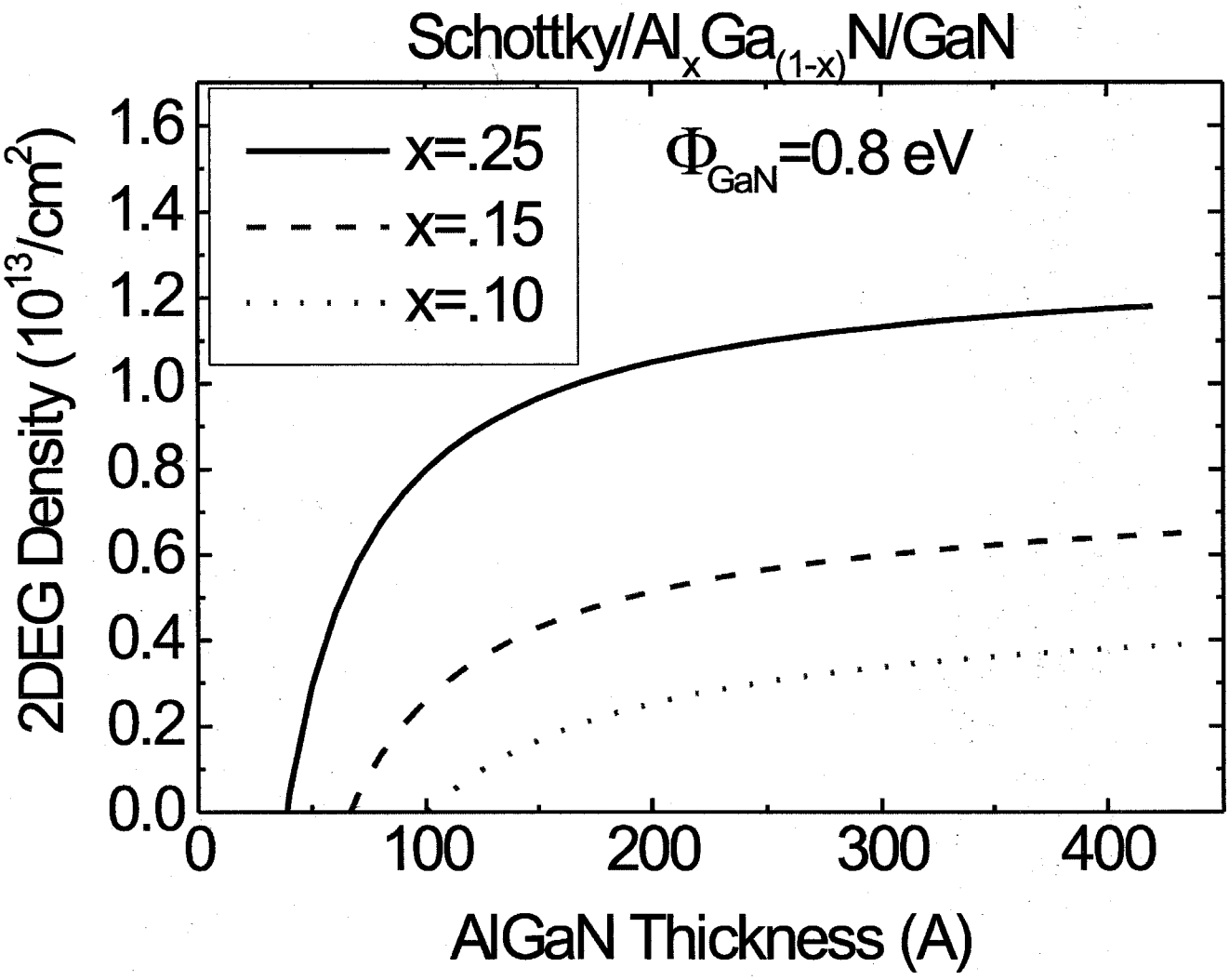

Figure 2.8: Thickness dependence of 2DEG in AlGaN/GaN structures. Graph shows the role over in 2DEG density after ~150 Å.

tal effects the electric field has on oscillator strength and hence quantum efficiency, minimization of these fields is of particular interest to the LED and laser community. Of first order importance is the doping. The polarity of the growth determines the sign of the resulting piezoelectric polarization charge at the well interface. As mentioned above, MOCVD and HVPE have been shown to result in Ga faced GaN. This results in a strain generated electric field that points towards the substrate. For the depletion region field to reduce the piezoelectric field a growth sequence resulting in p-GaN/InGaN/n-GaN/substrate is required for Ga faced material. For complete cancellation of the electric field in the well region, the charge in the donor depletion region plus the piezoelectric polarization charge at the well-donor region interface must equal zero. A mathematical statement of this is;

$$P = qL_dN_d = \sqrt{\frac{2\varepsilon_s q N_d N_a V_{bi}}{N_d + N_a}} \tag{2.5}$$

Here, P is the polarization in the well, N_d is the donor density in the n region, N_a is the acceptor density in the p region, L_d is the depletion length in the donor region, ε_s is the dielectric constant in the bulk, and V_{bi} is the built in voltage. Due to the high doping concentrations required for p-type GaN, a large disparity in doping density occurs in GaN p-n structures. Setting the ratio of acceptors in the p region to donors in the n region equal to α, i.e., $N_a = \alpha N_d$, and solving for N_d, this reduces to

$$N_d = \frac{P^2(\alpha + 1)}{2\varepsilon_s q V_{bi}\alpha} \tag{2.6}$$

Figure 2.9 shows the results of this calculation for a range of alloy compositions with α set to 1. Due to the approximately linear nature of the polarization charge on alloy composition, the doping density can be well approximated by a second order polynomial in x. For InGaN/GaN N_d ~6.7x10^{20}/cm^3 x^2 and for GaN/AlGaN N_d ~2.0x10^{19}/cm^3 x^2. These numbers are well within the region of doping densities achieved in GaN and should not cause difficulties in growth of appropriately doped structures. One caveat that must be discussed is the dependence of the built-in volt-

age, V_{bi}, on doping density. The built-in voltage is the energy difference between the fermi levels in the n and p layers. We have used a constant V_{bi} for these calculations of 3.2 eV. This will require modification based on fermi levels determined for actual devices, but is not expected to vary significantly. In addition, the on state voltage will decrease the depletion region and result in a lower cancellation field. Reduction of the value used here by the voltage drop across the device in the on state will be required when determining the doping density of the structure.

Schottky Barrier Detectors

Currently, GaN is predominantly grown with Ga faced polarity. N faced material, however, can result in a wide range of new and interesting devices. One is a UV detector employing piezoelectric fields to reject leakage current. Figure 2.10 shows the structure and band diagram for a field enhanced detector. We present the barrier enhancement and rejection field for this device.

A simple electrostatic analysis results in the below equation connecting the Schottky height at the metal-AlGaN interface to the depletion length in the GaN bulk.

$$\phi_{AlGaN} = \frac{0.5N_d eL^2}{\varepsilon_{GaN}} + \frac{(N_d eL - \sigma_p)d}{\varepsilon_{AlGaN}} + \frac{0.5N_l ed^2}{\varepsilon_{AlGaN}} + E_F + \Delta E_c \qquad (2.7)$$

In equation 2.7, N_d (N_l) is the doping density in the GaN (AlGaN), L is the depletion width, d is the strained layer thickness, E_F is the fermi-level to conduction band edge energy separation, and ΔE_c is the conduction band offset. After solving this equation for the depletion width (L), the effective Schottky height can be calculated from;

$$\phi_{eff} = \frac{0.5N_d eL^2}{\varepsilon_{GaN}} + E_F + \Delta E_c \qquad (2.8)$$

Figure 2.11a shows the calculated effective Schottky height for three values of barrier thickness versus aluminum content in the barrier region. We have used $10^{18}/\text{cm}^3$ ($10^{16}/\text{cm}^3$) for the bulk (strained layer) doping density. For low Al mole fraction the barrier height is equal to the Schottky height of the metal-AlGaN interface. In this

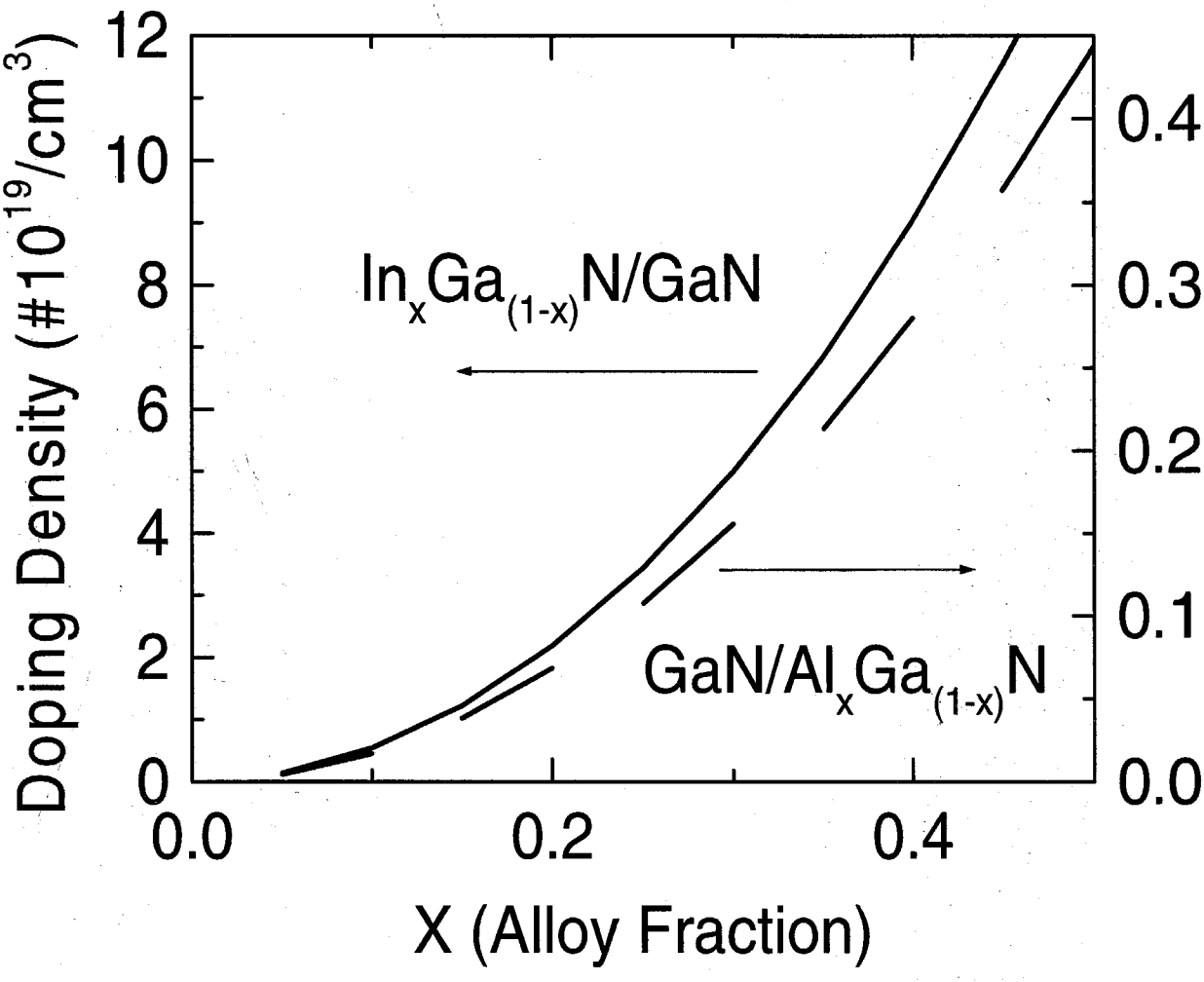

Figure 2.9: Graph of required doping density for field cancellation in InGaN/GaN and GaN/AlGaN quantum wells for α equal to 1.

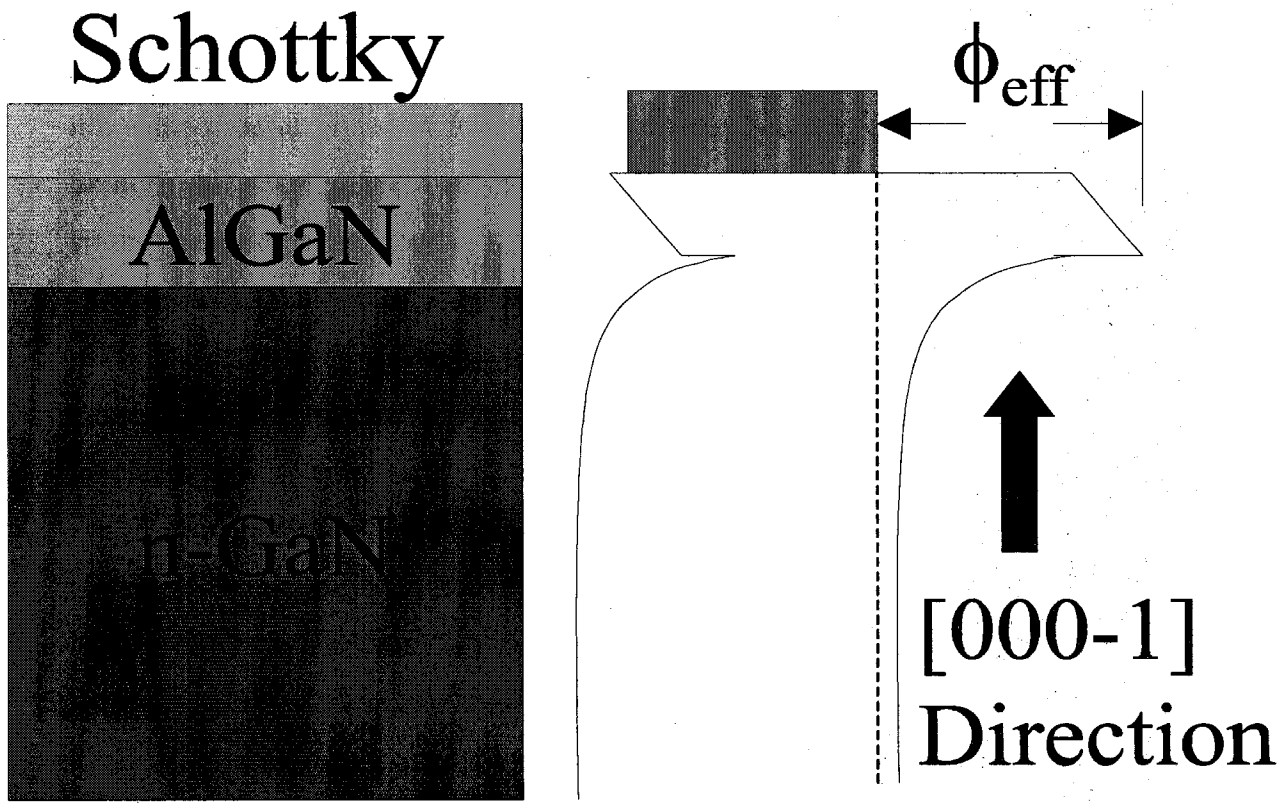

Figure 2.10: Schematic of epitaxial layer structure and band-edge energy diagram for Schottky detector.

region the polarization field is not large enough to overcome the depletion region field and produce added Schottky height. The Al molar fraction at which this kink occurs is dependent on the doping in the GaN. The maximum effective Schottky height is reached when the GaN valence band at the AlGaN/GaN interface moves above the Fermi level. At this point, a two-dimensional hole gas is formed at the AlGaN/GaN interface. This is analogous to the electron gas formed in the HFET structure. Increasing the polarization field further results in increased hole accumulation, but little additional height is achieved. It has been found that coherently strained $Al_{0.25}Ga_{0.75}N$ can be grown up to ~ 300 Å on GaN.[45] This indicates that strain relaxation should not cause a significant shift from these calculated Schottky heights. Doping density is found to have a significant effect on the effective Schottky height. Figure 2.11b illustrates the changes in effective height with doping in both the barrier layer and bulk. It was found that doping resulted in a later turn on and lower over all enhancement of the Schottky height. Doping in the bulk layer had the greatest effect on Schottky heights; however, doping in the barrier layer caused significant reduction in effective barrier height as well.

The nitrides show exceptional promise for many applications ranging from optoelectronic devices to high power switches. Their unique combination of robustness, large breakdown fields and large piezoelectric coefficients makes them interesting for a variety of novel applications that other material systems are incapable of performing. The lack of a mature growth technology for the nitrides, however, hinders the development of many of these interesting devices. The next chapter discusses the issues related to nitride growth and our investigations of molecular beam epitaxy growth of column III nitrides.

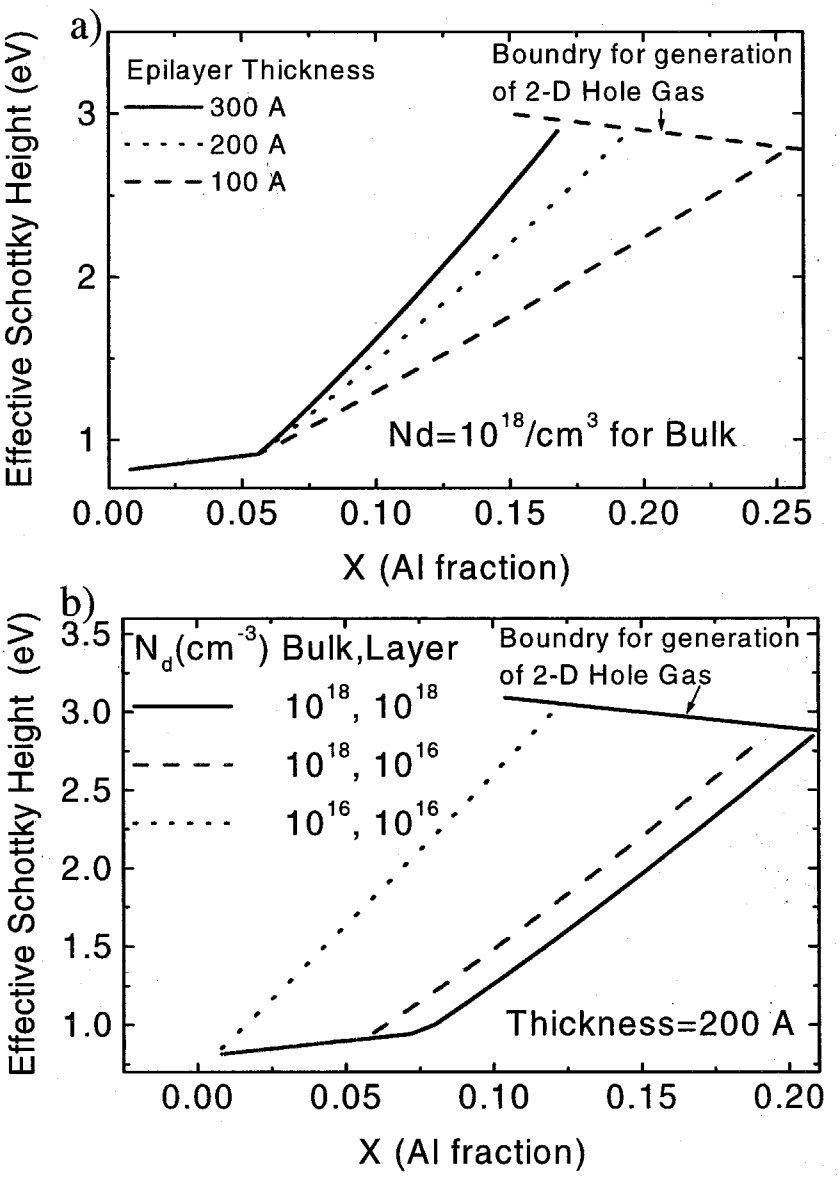

Figure 2.11: Graph showing a) effective Schottky heights as a function of Al mole fraction for three values of epilayer thickness, b) effective Schottky height versus Al mole fraction for three sets of doping parameters.

Bibliography

[1] S. Nakamura and G. Fasol, *The Blue Laser Diode* (Springer, Berlin, 1997).

[2] Z. Bandic, P. Bridger, E. Piquette, T. McGill, R. Vaudo, V. Phanse, and J. Redwing, Appl. Phys. Lett.**74**, 1266 (1999).

[3] X. Dang, R. Welty, D. Qiao, P. Asbeck, S. Lau, E. Yu, K. Boutros, and J. Redwing, Elec. Lett. **35**, 602 (1999).

[4] W. Johnson, J. Parsons, and M. Crew, J. Phys. Chem. **36**, 2561 (1932).

[5] H. Maruska and J. Tietjen, Appl. Phys. Lett. **15**, 327 (1969).

[6] A. Zhang, G. Dang, F. Ren, X. Cao, H. Cho, E. Lambers, S. Pearton, R. Shul, L. Zhang, A. Baca, R. Hickman, and J. Van Hove, MRS Internet J. Nitr. Semi. Res.**5**, U715 (2000).

[7] T. Zhu, D. Lambert, B. Shelton, M. Wong, U. Chowdhury, and R. Dupuis, Appl. Phys. Lett.**77**, 2918 (2000).

[8] X. Cao, S. Pearton, G. Dang, A. Zhang, F. Ren, R. Shul, L. Zhang, R. Hickman, and J. Van Hove, MRS Internet J. Nitr. Semi. Res.**5**, U481 (2000).

[9] E. Sichel and J. Pankove, J. Phys. Chem. **38**, 330 (1977).

[10] I. Chetverikova, M. Chukichev, and L. Rastorguev, Inorganic Materials **22**, 53 (1986).

[11] W. Yim, E. Stofko, P. Zanzucchi, J. Pankove, M. Ettenberg, and S. Gilbert, J. Appl. Phys. **44**, 292 (1973).

[12] G. Slack, J. Phys. Chem. Solids **34**, 321 (1973).

[13] W. Yim and R. Paff, J. Appl. Phys. **45**, 1456 (1974).

[14] K. Wang and R. Reeber, Mat. Res. Symp. Proc. **482**, 863 (1998).

[15] A. Sheleg and V. Savastenko, Izv. Akad. Nauk. SSSR Neorg. Mater **15**, 1598 (1979).

[16] M. Leszczynski, T. Suski, and H. Teiseyre, J. Appl. Phys. **76**, 4909 (1994).

[17] G. Slack and S. Bartram, J. Appl. Phys. **46**, 89 (1975).

[18] O. Ambacher, M. Brandt, R. Dimitrov, T. Metzger, M. Stutzmann, R. Fischer, A. Miehr, A. Bergmaier, and G. Dollinger, J. Vac. Sci. Technol. B**14**, 3532 (1996).

[19] K. Osamura, S. Naka, and Y. Murakami, J. Appl. Phys. **46**, 3432 (1975).

[20] D. Brunner, H. Angerer, E. Bustarret, F. Freudenberg, R. Hopler, R. Dimitrov, O. Ambacher, and M. Stutzmann, J. Appl. Phys.**82**, 5090 (1997).

[21] M. D. Bremser, W. G. Perry, T. Zheleva, N. V. Edwards, O. H. Nam, N. Parikh, D. E. Aspnes, and R. F. Davis, MRS Internet J. Nitr. Semi. Res.**1**, 8 (1996).

[22] Y. Koide, H. Itoh, M. Khan, K. Hiramatu, N. Sawaki, and I. Akasaki, J. Appl. Phys. **61**, 4540 (1987).

[23] K. Kim, A. Saxler, P. Kung, M. Razeghi, and K. Lim, Appl. Phys. Lett.**71**, 800 (1997).

[24] Q. Guo, H. Ogawa, and A. Yoshida, J. Crystal Growth **146**, 462 (1995).

[25] W. Gotz and N. Johnson, Appl. Phys. Lett. **68**, 667 (1996).

[26] I. Akasaki, H. Amano, M. Kito, and K. Hiramatsu, J. Lumin. **48-9**, 666 (1991).

[27] T. Tansley and C. Foley, Elec. Lett. **20**, 1066 (1984).

[28] D. Smith, Solid State Comm. **57**, 919 (1986).

[29] T. Keuch, R. Collins, D. Smith, and C. Mailhoit, J. Appl. Phys.**67**, 2650 (1990).

[30] R. Beck, M. Eriksson, R. Westervelt, K. Campman, and A. Gossard, Superlattices and Microstructures **20**, 363 (1996).

[31] F. Bernardini, V. Fiorentini, and D. Vanderbilt, Phys. Rev. B **56**, R10024 (1997).

[32] A. Bykhovski, V. Kaminski, M. Shur, Q. Chen, and M. Khan, Appl. Phys. Lett.**68**, 818 (1996).

[33] A. Bykhovski, B. Gelmont, and M. Shur, J. Appl. Phys.**74**, 6734 (1993).

[34] E. Yu, G. Sullivan, P. Asbeck, C. Wang, D. Quiao, and S. Lau, Appl. Phys. Lett. **71**, 2794 (1997).

[35] P. Asbeck, E. Yu, S. Lau, G. Sullivan, J. Van Hove, and J. Redwing, Electronic Lett. **33**, 1230 (1997).

[36] J. Im, H. Kollmer, J. Off, A. Sohmer, F. Scholz, and A. Hangleiter, Phys. Rev. B **57**, R9435 (1998).

[37] J. Im, H. Kollmer, J. Off, A. Sohmer, F. Scholz, and A. Hangleiter, Mat. Res. Soc. Symp. Proc. **482**, 513 (1998).

[38] T. Taakeuchi, S. Sota, M. Katsuagawa, M. Komori, H. Takeuchi, H. Amano, and I. Akasaki, Jpn. J. Appl. Phys. **36**, L382 (1997).

[39] J. Nye, *Physical Properties of Crystals* (Oxford, London, 1957).

[40] A. Polian, M. Grimsditch, and I. Grzegory, J. Appl. Phys. **79**, 3343 (1996).

[41] L. McNeil, M. Grimsditch, and R. French, J. Am. Ceram. Soc. **76**, 1132 (1993).

[42] E. Hellman, MRS Internet J. Nitr. Semi. Res.**3**, 11 (1998).

[43] J. Redwing, J. Flynn, M. Tischler, W. Mitchel, and A. Saxler, Proc. Mat. Res. Soc. **1**, 395 (1996).

[44] S. Nakamura, M. Senoh, S. Nagahama, N. Iwasa, T. Yamada, T. Matsushita, Y. Sugimoto, and H. Kiyoku, Appl. Phys. Lett.**70**, 1417 (1997).

[45] H. Kim, J. Lin, H. Jiang, W. Chow, A. Botchkarev, and H. Morkoc, Appl. Phys. Lett.**73**, 3426 (1998).

Chapter 3 Molecular Beam Epitaxy Growth of Column III Nitrides

3.1 Introduction

The first attempts to grow III-V nitrides took place in the early 1960's. The researchers of that time, however, encountered significant difficulties in producing high quality material. All GaN and InN material suffered from very high n-type background doping resulting from native defects believed to result from nitrogen vacancies. In addition, no suitable substrate was available with a similar lattice constant, and achieving p-type material, even in films with relatively low intrinsic doping, could not be achieved. In the last decade a number of notable advances in nitride growth have been achieved. The native background doping has been reduced to as little as $1x10^{16}/cm^3$ and p-type material is now routinely produced. AlGaN/GaN and GaN/InGaN heterostructures have been produced resulting in quantum well LEDs and lasers, high mobility transistors, and quarterwave reflectors. Zinc blende phases of GaN, AlN and InN have been grown, and there properties are beginning to be measured. These advances are largely a result of improvements in the growth technology presently available. We can be optimistic that with the current high level of research focused on nitride materials this rapid progress will continue. This chapter reviews some of the issues related to growth of nitride materials and the techniques employed for growth. In addition it describes our research into molecular beam epitaxial growth of column III nitrides.

3.2 Substrates

Ideally, growth of bulk gallium nitride from a melt, such as commonly used for other elemental and compound semiconductors, would be used to produce substrates for further device growth and fabrication. There are a number of fundamental difficulties in producing GaN boules using bulk growth techniques. The foremost barrier to bulk growth is the stability and low solubility of nitrogen. With a bond strength of 9.8eV, N_2 is extremely stable and resistant to any reaction in which it is required to dissociate. In addition, the solubility of nitrogen in liquid gallium is extremely low. These two constraints result in high temperatures, to dissociate significant amounts of the nitrogen, and high pressures, to induce substantial solution of the nitrogen into the melt, being required for bulk growth. Initial attempts to grow bulk GaN from a melt have been carried out at Unipress in Poland. The pressure in their growth apparatus was 20 kbar at a temperature of 2000 °C.[1] Some success was achieved, however, the largest samples produced were plate-like crystals of ~1cm diameter. In addition, these samples were highly conductive due to a high level of oxygen impurities and point defects. This success gives hope that GaN substrates from bulk will be achievable in the future. Currently, however, growth of GaN relies on heteroepitaxial growth techniques utilizing a range of different substrates.

3.3 Heteroepitaxial Substrates

Ideally, a substrate should be lattice matched in the plane of growth, have the same coefficient of thermal expansion, and be robust enough to withstand the high temperatures associated with nitride growth. Also, GaN is a polar compound and an unambiguous anion/cation ordering is desirable to avoid inversion domains. Similarly, since GaN is a wurtzite structure with stacking sequence ABABAB, growth on a zinc blende material such as GaAs with a stacking sequence of ABCABC results in stacking mismatch boundary effects at step edges.[2] Table 3.1 lists some of the substrates used for growth of GaN as well as their lattice and thermal mismatch to

Table 3.1: Comparison of some substrates for GaN heteroepitaxy.

Substrate Material	a (hex) (Å)	Mismatch (%)	$\Delta\alpha_{Ta}$ ($10^{-6}K^{-1}$)	Stacking Mismatch
Al_2O_3 (0001)	4.758	16.1	-1.9	yes, NP
6H-SiC (0001)	3.08	3.5	1.4	yes
ZnO (0001)	3.252	-1.9	2.7	no
GaAs (111)	3.997	-20.0	~ -1	yes
Si (111)	3.840	-17	3	yes, NP
GaAs (100)	5.653	-20.0	~ -1	no

GaN. No material possesses all of the desired qualities, but significant progress has been made in overcoming many of the difficulties associated with growth on dissimilar substrates. SiC has many suitable qualities as a substrate for GaN. As shown in table 3.1, the in-plane lattice mismatch is 3.5% and the thermal mismatch is 1.4x10^{-6}/K. SiC is also a polar material which facilitates growth of single polar GaN. It has been shown that growth on Si face (0001) SiC results in Ga polar (0001) GaN, while growth on C face (000$\bar{1}$) SiC results in N polar (000$\bar{1}$) GaN. In addition, SiC is a thermally stable material and can be doped both n and p type. The major drawback of SiC is its price. Typical substrates of 2 inch diameter cost around $2000, and growth of GaN on SiC has been shown to produce only marginally better material than material grown on the most commonly used substrate, sapphire. Sapphire is a very robust and chemically inert material with several orientations available for use as substrates. GaN has been investigated on a number of these planes.[3, 4] The most commonly used plane is the c-plane (0001). The lattice parameter and thermal expansion coefficient mismatches are quite large compared to SiC, but sapphire's price is ~5% that of SiC. Although sapphire is a highly ionic compound, it is not polar, thus it does not present a preferred polarity of growth for GaN. A great deal of research has focused on the nucleation and growth of GaN on sapphire, and a number of recipes have been developed to optimize the growth of unipolar GaN with reduced defect density. Wu et.al. have shown that optimized growth results in up to two orders of magnitude improvement in defect density.[5] Most high performance GaN devices have been

grown on sapphire, including light emitting diodes,[6] lasers,[7] HFET's,[8] and high power diodes.[9] A number of other materials have been investigated as candidates for substrates for GaN. GaAs is of interest for production of the zinc blende phase of GaN. Cubic GaN has been reported by a number of researchers and it has been determined that an arsenic overpressure during growth is required to stabilize the zinc blende phase. In addition, successful fabrication of InGaN/GaN quantum well and GaN p-n LED's have been reported for zinc blende GaN grown on GaAs.[10, 11] Problems related to growth of GaN on GaAs stem from their large lattice mismatch (20%), and the instability of GaAs at optimum GaN growth temperatures. Si(111) has also been tried as a substrate with recent reports of AlGaN/GaN heterostructures containing a two-dimensional electron gas at the AlGaN GaN interface with room temperature mobility of 1600 cm^2/V s.[12] Many other exotic materials have also been investigated as substrates for GaN. These include $MgAl_2O_4$[13], $LiGaO_2$[14], $NdGaO_3$[15]. They are all decent lattice matches to GaN, however, they suffer from instability at high temperature, and unintentional oxygen doping of the resulting GaN is a concern. Hafnium has also been shown to have many positive attributes as a substrate for GaN.[16] It has a nearly identical in plane lattice constant and very similar coefficient of thermal expansion (5.6x10$^-$6/K for GaN 5.96x10$^-$6/K for Hf). It is very stable to temperatures well above growth temperature of GaN, and it is conductive, there by overcoming one of the difficulties of device fabrication on sapphire. Hf suffers two drawbacks. One is that Hf is an extremely hard and stable material making production of smooth single crystal substrates almost as difficult as making GaN. Second is that HfO_2 is also both chemically and thermally stable making removal of the native oxide quite difficult. GaN substrates have been produced by a couple of techniques. One method is rather straightforward, growth of thick GaN layers on sapphire, followed by chemomechanical polishing to remove the sapphire. The other involves growth of thick GaN by HVPE, followed by exposing the back side of the sapphire to high power laser pulses from an eximer laser. The wavelength of the eximer laser is such that the light is transmitted through the sapphire and absorbed at the GaN/sapphire interface. The pulses are set to have enough

energy to decompose the GaN. After scanning across the entire substrate, the wafer is heated to melt the Ga, and the GaN slides off the substrate.[17] These substrates still possess the high defect levels associated with the original growth on sapphire, but do enable back side contacts to the GaN. The lack of an ideal substrate results in many growth related difficulties and degrades the resulting device performance. One problem related to heteroepitaxial growth on highly mismatched substrates is large mosaicity in the deposited layer. This can be seen in the x-ray diffraction ω-$\omega/2\Theta$ area scan shown in figure 3.1. This sample consisted of AlN grown on sapphire followed by growth of GaN and then InN. With each layer the width of the ω rocking curve broadens, indicating increased tilt of grains within the films. The large amount of crystal disorder indicated by the diffraction pattern has significant impact on a number of key parameters for device performance such as carrier mobility, leakage current, and minority carrier lifetime. A solution to the problems associated with growth on highly mismatched substrates has not been discovered yet, however, many techniques for improving crystal quality in the heteroepitaxial material have been developed for GaN. The following sections discuss some of the growth methods used to produce nitride materials, and some of the techniques used to improve crystal quality.

3.4 Methods of Growth

A number of growth techniques have been employed to produce heteroepitaxial GaN on many of the substrates discussed in the previous section. These methods include sublimation, pulsed laser deposition (PLD), hydride vapor phase epitaxy (HVPE), metalorganic chemical vapor deposition (MOCVD), and several variations of molecular beam epitaxy including ammonia gas source MBE (GSMBE), metalorganic MBE (MOMBE), and plasma assisted MBE (RF-MBE and ECR-MBE). The most studied technique for growth of nitrides is by far MOCVD. The original success that reignited research in GaN was achieved by Akasaki and coworkers [18] and S. Nakamura of Nichia Chemical Industries. [19] They both used MOCVD to produce high quality GaN on sapphire. The development of low temperature buffer layers for im-

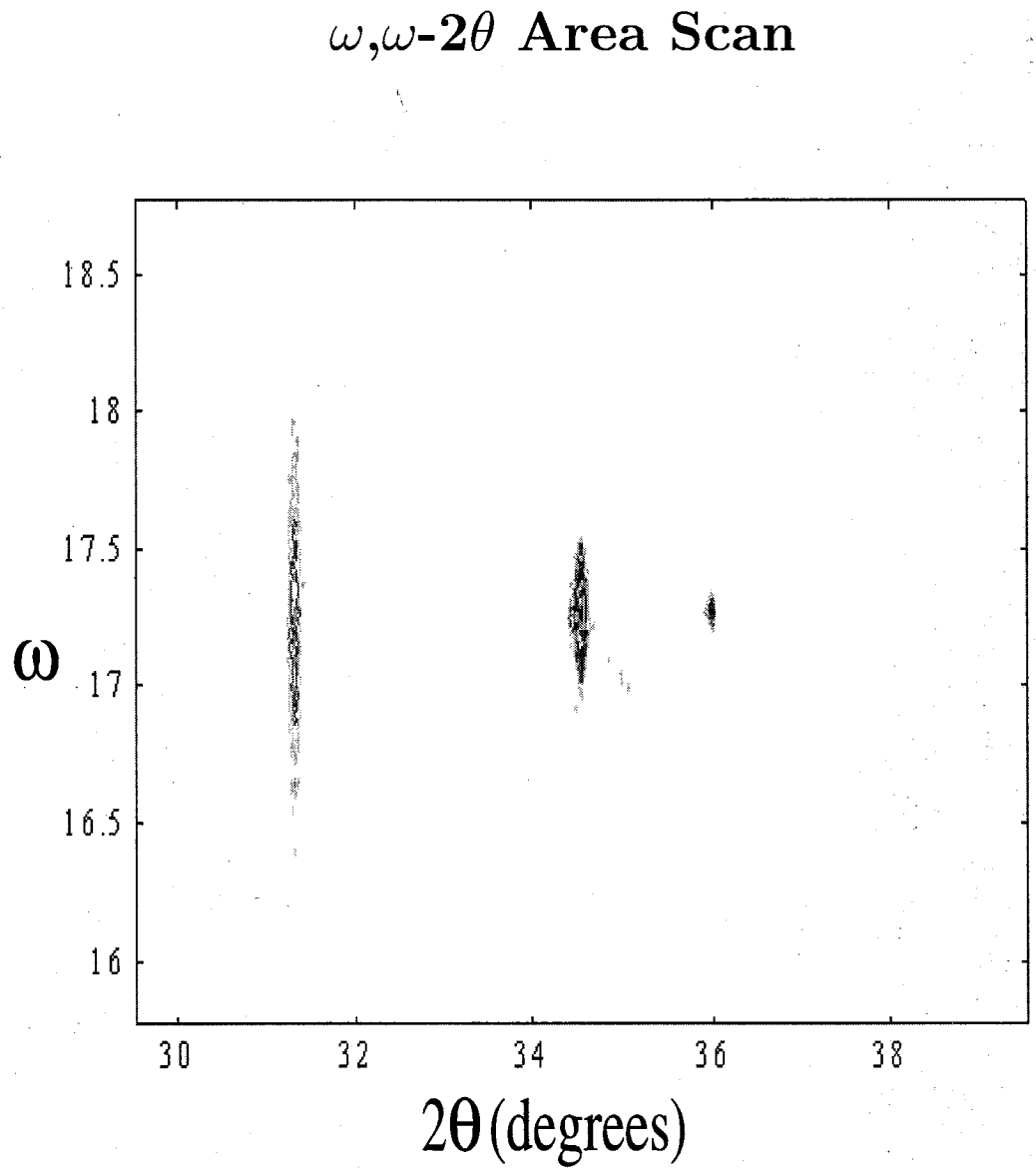

Figure 3.1: X-ray diffraction pattern of InN/GaN/AlN/Sapphire.

proved structural and electrical characteristics, as well as low energy electron beam irradiation (LEEBI) for the activation of Mg acceptors to produce p-type material, were key advances in GaN growth.

3.4.1 MOCVD

MOCVD growth is usually carried out in an inductively heated reactor with a graphite susceptor used to hold, rotate, and heat the substrate. Highly reactive precursor gases are introduced into the chamber and flow to the substrate surface where they are cracked by the hot substrate and react to form the desired compound. The typical nitrogen precursor gas is ammonia (NH_3), while the group III precursors are the metalorganic compounds, trimethyl-gallium (TMG) for Ga, trimethyl-indium (TMI) for In, and trimethyl-aluminum (TMA) or triethyl-aluminum (TEA) for Al. In addition, carrier gases such as H_2 or N_2 are used to control the convection and flow patterns within the chamber. Pressure within the chamber ranges from .1 to 1 atmosphere, and the substrate is kept between 1050 °C and 1100 °C during growth. MOCVD can achieve 2-5 μm per hour growth rate and results in arguably the best material available.

3.4.2 Vapor Phase Epitaxy

Hydride vapor phase epitaxy (HVPE) has attracted considerable interest for growing GaN due to the high growth rates, up to several hundred microns per hour, achievable with this technique. HVPE grown films are attractive for applications in high power electronics in which thick layers are required to stand off high voltages. In addition, thick HVPE material is being produced to serve as quasibulk substrates for other growth techniques. In conventional HVPE, GaCl and ammonia are used as sources of Ga and nitrogen. The $GaCl_3$ is produced by flowing HCl, along with a carrier gas such as hydrogen or nitrogen, over liquid Ga. The supply of $GaCl_3$ is then controlled by the Ga temperature and gas flow rate. The reactor pressure and growth temperatures are very similar to those of MOCVD.

3.4.3 MBE

Molecular beam epitaxy differs from the previous growth techniques in that the chamber pressure during growth is much lower, typically 10^{-6}-10^{-4}Torr. This allows the use of a number of in-situ diagnostic tools such as desorption mass spectroscopy, ellipsometry, and a number of electron diffraction techniques, including RHEED, LEED, and RHEELS, for studying growth kinematics. Growth temperatures are much lower than in VPE techniques, typically between 750 °C and 850 °C. Growth rates are quite low for the nitrides, $\sim$.1-1μm/hr. These two features combine to make MBE very attractive for producing extremely abrupt interfaces for quantum wells and HEMTs.

3.5 Our Growth System

The III-nitride growth system used during the investigations presented in this thesis is one of four MBE systems attached to a growth, metalization, and analysis cluster operated by our research group. The system includes dedicated growth chambers for II-VI, Si-Ge, III-As/Sb, and III-N materials interconnected via a vacuum transfer tube to an eight source e-beam metalization chamber and x-ray photoelectron/Auger electron spectroscopy chamber. This system provides great flexibility for growth and characterization of a wide range of materials and heterostructures in multiple material systems. Figure 3.2 is a schematic of our system.

3.5.1 Group III Sources

The group III metals as well as the doping materials of Mg and Si are obtained from effusion cells in our system. The gallium and indium cells are dual zone effusion cells. They have two heater coils, one wrapped near the lip, the other larger and positioned around the bulk of the cell. This configuration is designed to allow added heating to the lip of the cell. Typically the lip is maintained 50-100 °C hotter than the bulk. This reduces recondensation of metal from the bulk onto the lip where "spitting" may occur. Spitting has been implicated as a cause of oval defects in III-V materials.

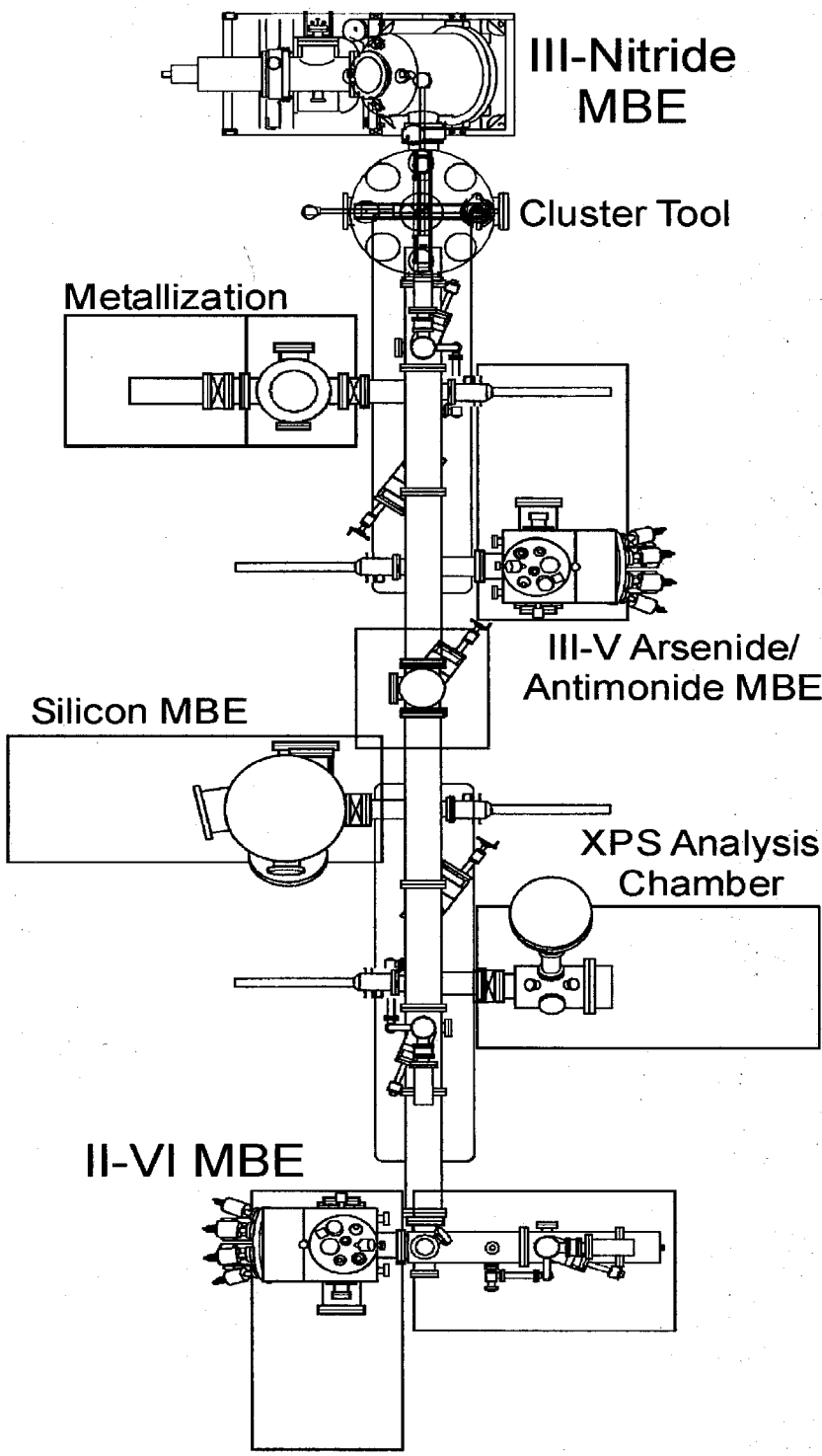

Figure 3.2: Schematic of the vacuum system used for this work.

The aluminum source cell is a "cold lip" cell. As opposed to the Ga and In cells, this cell does not have heating near the lip, and in addition has venting holes in the crucible shielding to allow extra cooling near the lip. This form of effusion cell was developed to reduce creepage associated with aluminum. Aluminum wets the PBN crucible and will creep up out of the cell and around to the heating filaments where it can short or otherwise damage the cell. In conjunction with the high nitrogen plasma pressure within the chamber, which bonds with the creeping aluminum near the lip, significant reduction of creepage can be achieved. Due to silicon's low vapor pressure, the Si dopent cell is specifically designed for high temperatures. Typical temperatures for Si doping of GaN range from 1100 °C to 1400 °C. The magnesium dopent source uses a standard cell. No exceptional measures are required for Mg due to its high vapor pressure, and cell temperatures are usually between 250 °C and 400 °C.

3.5.2 Nitrogen Source

While MBE usually relies on solid phase elemental or compound materials, nitrogen is unavailable in such a form. N_2 is effectively inert and useless as a source material unless measures are taken to increase its reactivity. Several different methods have been used to produce chemically active nitrogen containing source materials. Ammonia has been used as the nitrogen source for growth of GaN, and growth rates of 1-2μm/hr have been achieved. MBE using ammonia gas as the source of group V element is often referred to as gas source MBE (GSMBE). In this methodology the substrate is maintained at or above 900 °C and the ammonia is cracked at the substrate surface. Other more reactive gases have been tried as sources of nitrogen including azides and hydrazine. However, no significant improvement over ammonia was observed and these gases pose a significantly greater health risk than ammonia. Another method for obtaining active nitrogen is through excitation of N_2 in a plasma source. The two common forms of this type of source are electron cyclotron resonance (ECR), and radio frequency (RF) plasma sources. High quality GaN has been reported using both of these types of nitrogen sources. The work reported here was

performed using a RF plasma source from SVT Associates. The source operates by releasing ultra high purity nitrogen into the excitation chamber through a high precision leak valve. The nitrogen is then excited by a water cooled RF coil operating at 13.56 MHz with a forward bias of 200-400W. The excited nitrogen then escapes the plasma source through an aperture directed toward the substrate. Various aperture designs have been investigated from single hole apertures to shower head apertures with 400 small holes. Our source has a single hole aperture of $3mm^2$ area. Until recently plasma sources were extremely inefficient with only 1-2% activation of the nitrogen. Advances in design have resulted in up to 45% activation efficiency and growth rates as high as $6\mu m/hr$ demonstrated by SVT Associates.

3.5.3 In Situ Characterization

The MBE system is equipped to perform reflection high energy electron diffraction (RHEED) with a 10keV electron gun and 8" phosphor screen. The electron gun is also used in conjunction with optical piping and a spectrometer for in situ cathodoluminescence. This has been extremely useful for characterization of the optical quality of the as grown films. A translatable ion gauge is also attached to the system such that partial pressures of the various constituents can be measured. A difficulty encountered using this method of determining partial pressures is that the nitrogen plasma is highly reactive and tended to etch the ion gauge filaments and cage wires resulting in variations in measured pressures over time, and eventual failure of the device. This is a common problem with all of the filaments within the chamber, but to a lesser extent given there distance from the plasma source. In addition, plasma etching of the PBN crucibles overtime makes them more susceptible to cracking during temperature cycling, and inadvertent boron doping of the GaN has been reported to be as high as $10^{19}/cm^3$ when aged PBN crucibles are used.[20] Therefore, care must be taken to replace crucibles on a regular basis. In place of the translatable ion gauge, a residual gas analyzer has been placed in an empty source port for obtaining consistency in partial pressures from growth to growth, as well as investigating desorption of the

growth constituents from the substrate.

3.6 Growth Procedures and Observations

A typical growth cycle consists of substrate introduction, outgasing, nitridation, buffer layer deposition, and main layer growth. After introduction of the substrate, the cryoshrouds are cooled using liquid nitrogen gravity fed from tanks on the roof. The substrate is heated to 1000 °C during chamber cooldown to remove any surface contaminants and outgas the substrate. The nitrogen leak valve is then opened to obtain a chamber pressure of $\sim 2 \times 10^{-4}$Torr and a nitrogen plasma is ignited while the various metal temperatures are raised to growth temperatures. It is important to ignite the plasma prior to melting the Al at ~760 °C as discussed earlier to avoid creepage. The nitrogen plasma is then set to its typical grow parameters, $\sim 5 \times 10^{-5}$Torr and 350W forward power. Nitridation of the sapphire substrate is then performed to form a thin layer of AlN on the surface of the Al_2O_3. A buffer layer is then deposited to nucleate growth. Substrate and source temperatures are then raised appropriately, and the main layer growth is then initiated. Each of the preceding steps can have significant effects on the quality of the resulting film. Optimization of all of the parameters available can take years of growth and study. In addition, many conflicting reports of the effects of any individual parameter on growth quality exist in the literature, making determination of ideal nitridation, buffer layer, and growth parameters exceedingly difficult. The remainder of this chapter will discuss investigations into the effects each of these parameters has on film morphology and optical quality.

3.7 Sapphire Substrates and Nitridation

Several studies of the nitridation of sapphire have been reported in the literature. The effect of substrate temperature during nitridation was studied by Namkoong et. al.[21] They report significant improvement in GaN surface morphology after employing low temperature nitridation. Roughness in the GaN grown after high

temperature nitridation has been ascribed to formation of AlN islands on the sapphire prior to GaN depostition.[22] These islands act as nucleation centers for growth of the GaN. This then leads to large grains that coalesce as the film grows, forming the large hexagonal morphology characteristic of MBE grown GaN. Other authors, however,[20] believe AlBN caused by decomposition of the PBN crucible in plasma sources leads to zinc blende inclusions at the sapphire GaN interface. These zinc blende areas are cited as the cause of the zinc blende RHEED spots frequently observed during the initiation of GaN growth on nitrided sapphire. Subsequent overgrowth of these inclusions is cited as the cause of the typically rough surface morphology of GaN. Others believe that the difference in growth rate between Ga polar and N polar GaN leads to surface roughening. Initiation of unipolar GaN then would be a key issue for surface morphology in addition to its importance in electrical quality of material and its role in piezoelectric devices. One possible explanation for the conflicting reports on nitridation pretreatments is that different authors cite different material parameters for determining what is beneficial and detrimental to the subsequent growth of GaN. An example of this are the conflicting reports associated with initial nitridation time. Namkoong reported that long nitridation times, greater than one hour, result in higher quality GaN material based on symmetric x-ray diffraction peaks.[21] Keller et. al. [23] found that the nitridation time significantly affects the XRD width of GaN as well. Short nitridation times of 60s resulted in symmetric [0002] peak FWHM widths of 269 arcsec while long exposures of 400s resulted in widths of 40 arcsec. This would agree with the previous report. The asymmetric $[10\bar{1}2]$ peaks, however, showed the opposite effect with the short exposure resulting in widths of 413 arcsec, and long exposures resulting in 740 arcsec. This data then shows that depending on the choice of investigation, different conclusions could be drawn from the same set of samples. This paper, however, was very thorough and went on to investigate the electrical, optical, and microstructural characteristics of the samples. It was found that the improvement in mosaic tilt of the sample was commensurate with an increase in pure edge dislocations. This resulted in electron mobilities of 149 cm^2/Vs for long exposures and 592 cm^2/Vs for short nitridation times. This type

of complete characterization is required for MBE grown material for a wide range of parameters whose effects are still poorly characterized.

3.8 Buffer Layers and Polarity

Until 1985, GaN grown by MOCVD was deposited directly on sapphire, and resulted in films with rough surfaces and high defect levels. Amano et. al. significantly improved the morphology, electrical, and optical characteristics of their GaN by depositing a thin,$\sim$ 50 Å, AlN buffer layer on the sapphire before growth of GaN.[18] Nakamura adopted the low temperature buffer layer approach, but used GaN as the buffer material.[24] Optimization of this buffer layer process resulted in the demonstration of blue LEDs.[6] Both AlN and GaN buffer layers result in Ga polar material in MOCVD grown GaN. Early growth of GaN by MBE resulted in nitrogen polar material. Recently, however, Ga polar material has been reported for AlN buffer layers.[8, 25] This has lead to control of crystal polarity and fabrication of normal and inverted heterojunction field effect transistors.[26, 27] Control of polarity in conjunction with piezoelectric engineering of strain fields also allows fabrication of other interesting devices as discussed in chapter 2. A great deal of effort has been directed at determination of crystal polarity. (For a good review see Hellman.[28]) Post growth determination of crystal polarity is usually done by chemical stability tests. Nitrogen polar GaN has been shown to etch much more rapidly than Ga polar material when placed in strong alkali solutions, $\sim$100 Å/min for N polar and $<$10 Å/min for Ga polar. More extravagant techniques, such as convergent beam electron diffraction, have been used for polarity determination; however, this requires significant equipment and analysis of the resulting pattern is not straight forward. In situ determination of polarity has benefited greatly from a systematic mapping of the reconstructions of both polarities of GaN.[29]

Although none of the reconstructions observed by Smith et. al. are stable at typical growth temperatures, $\sim$800 °C, the Ga polar 2x2 reconstruction is stable under nitrogen plasma exposure at growth temperature. Nitrogen polar material only

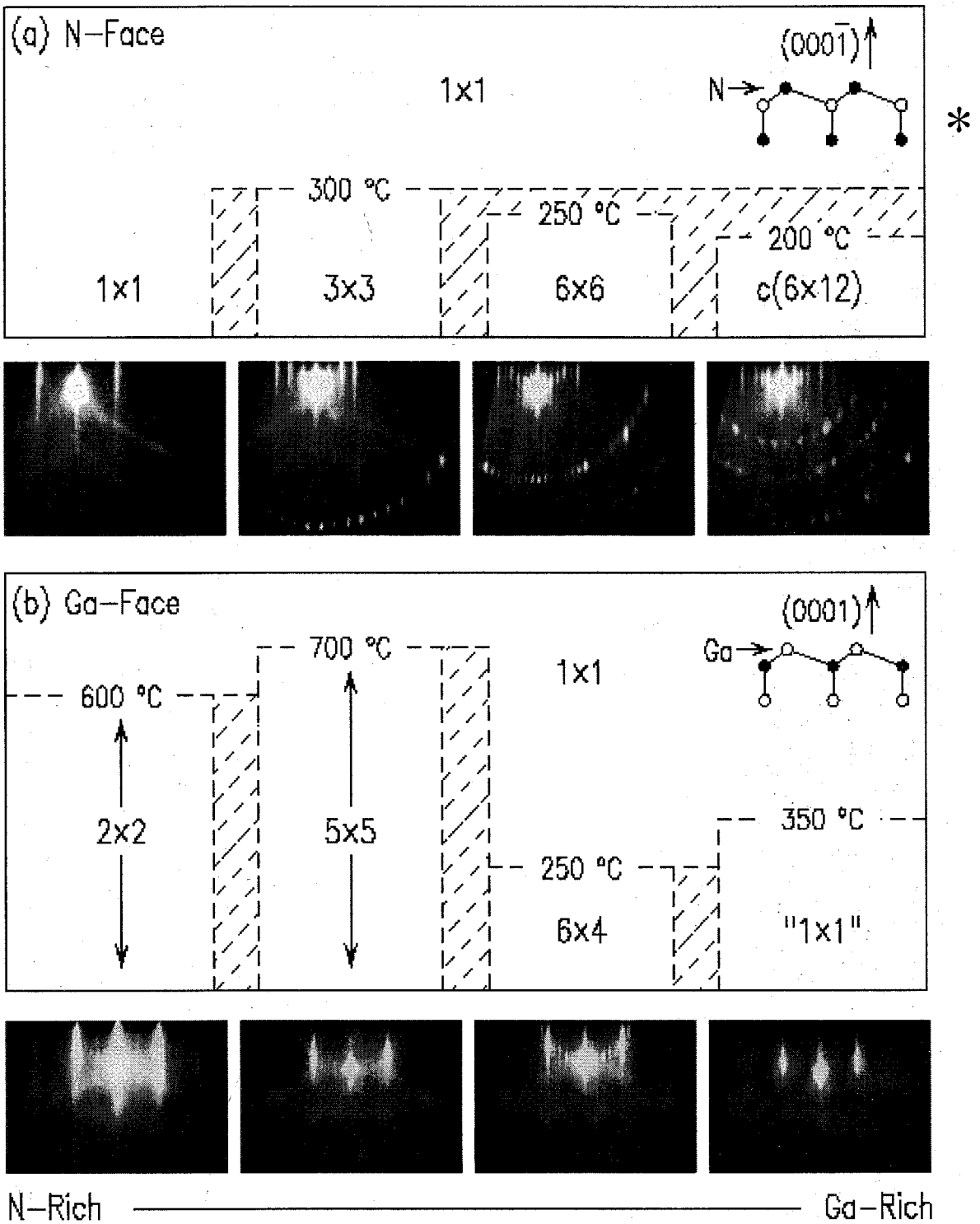

Figure 3.3: Mapping of reconstructions of GaN.[29]

shows a 1x1 reconstruction at growth temperature. Confirmation of nitrogen polarity occurs during cool down of the sample after growth. If the surface of the sample is exposed to the nitrogen plasma during cool down, the 1x1 reconstruction is maintained throughout cool down. If, however, the plasma is shuttered immediately after growth, the slight decomposition of the sample during cool down results in enough excess Ga on the surface to result in one of the many reconstructions of the GaN surface. Figure 3.4a shows the 2x reconstruction observed during growth of Ga polar GaN. Figure 3.4b shows the 3x reconstruction of N polar GaN after cool down. In addition to polarity control, buffer layers play a critical role in determining morphologies during subsequent growth. It is believed that the growth rate of the N and Ga polar surfaces is different depending on the particular growth conditions present at the surface. This can lead to height variations over the GaN surface. In addition, nucleation over the entire substrate is a key requirement of the buffer layer. Figure 3.5 shows AFM scans of three MBE samples nucleated under different conditions, and one MOCVD sample for reference. The morphology of sample a is characteristic of a number of different buffer layer conditions. High and low temperature buffer layers of either AlN or GaN result in the hexagonal pitting observed to decorate the surface of sample a if nitrogen rich or to a lesser extent stoichiometric growth conditions are used during the first few seconds of growth. In fact, highly metal rich conditions for a short time result in the lowest occurrence of pits. Care must be taken, however, to avoid the formation and subsequent nitridation of metal droplets. RHEED observations are a valuable tool during the nucleation process. After nitridation of the sapphire substrate, the RHEED pattern is typically a streaky and bright AlN pattern. Upon opening of the Al shutter, the pattern changes rapidly. For nitrogen rich growth, the RHEED pattern becomes bright, spotty, and diffuse. This set of changes correspond to the formation of AlN islands with a nitrogen terminated surface. The lack of a conductive metal termination layer results in charging, and correspondingly a diffuse RHEED pattern. For metal rich conditions, the RHEED pattern remains streaky, but dims rapidly and disappears. Under our growth conditions this occurs in approximately 10-15 seconds. Some researchers have attributed this to formation of an amorphous layer of AlN.

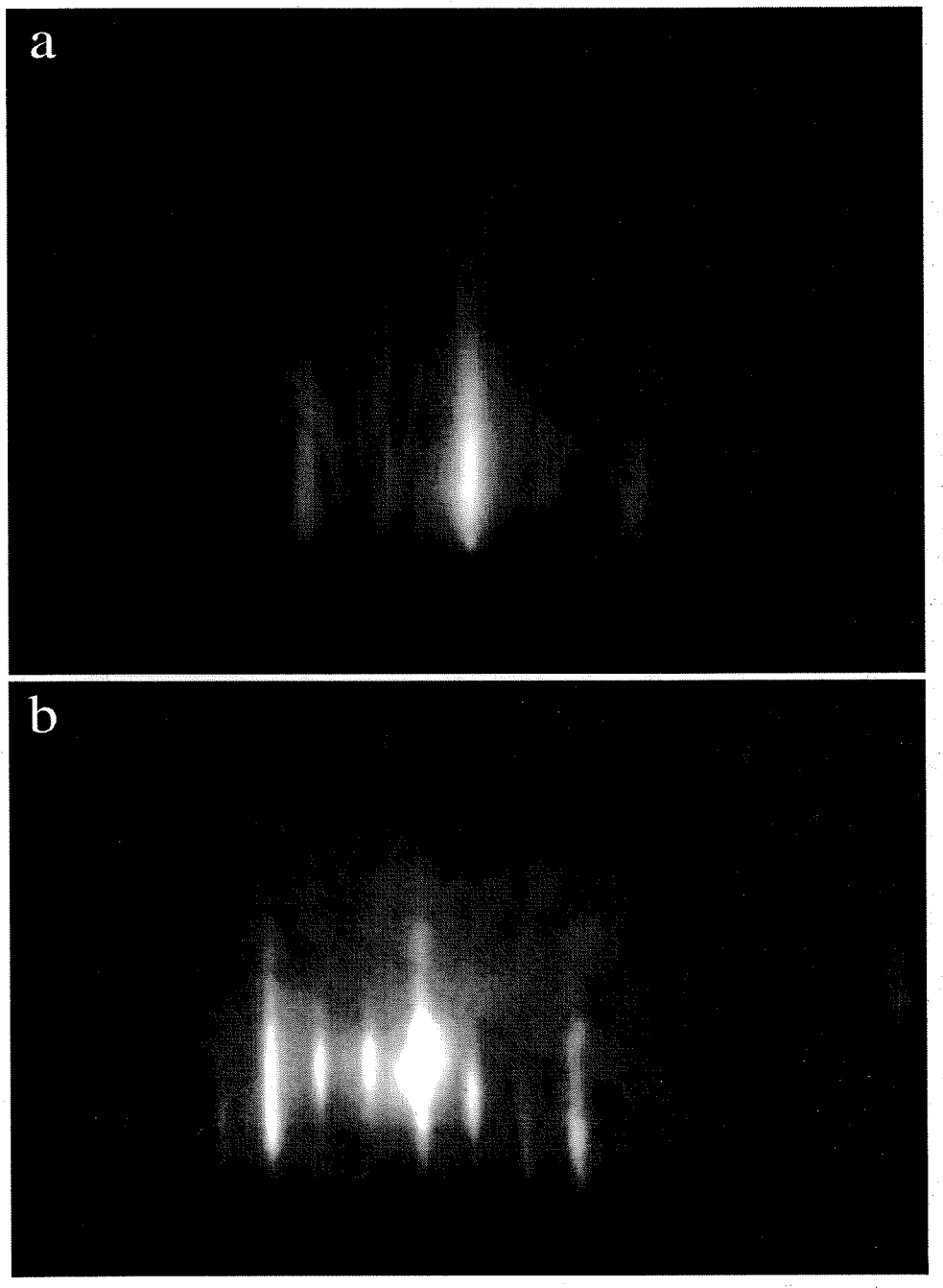

Figure 3.4: Reconstructions of GaN, a)2x reconstruction during growth interrupt of Ga polar GaN while exposing to nitrogen plasma, b)3x reconstruction after cool down of N polar GaN.

Shuttering the Al at this stage, however, results in an immediate brightening of the RHEED pattern and streaks are still observed. This indicates that a crystalline layer of AlN is still present and growing under a few monolayers of amorphous Al riding on the surface. This Al layer damps the electron diffraction from the underlying layer. The metal rich conditions of this type of buffer layer promote wetting of the surface and a more complete coverage of the substrate surface. Figure 3.5 b and c are two samples grown using Al rich buffer layers. For sample b growth was initiated at 600 °C while for sample c growth was initiated at 850 °C. There are two advantages to higher temperature buffer layers. One is that at elevated temperatures, the reevaporation of Al from the surface is higher. This hinders the formation of metal droplets on the surface. Secondly, initiating growth at a low temperature results in additional strain in the buffer layer when the substrate is ramped up to the optimal growth temperature. As seen in the figure, some improvement in surface morphology is obtained from higher temperature buffer layers. For the two samples shown in figure 3.5 b and c, the rms roughness over the entire 1 μm^2 area shown is 0.358nm for the low temperature buffer layer, and 0.066nm for the high temperature buffer layer. These are both significant improvements over nitrogen rich buffer layers that result in roughness similar to that shown in figure 3.5a which has an rms roughness of 1.7nm in the smooth regions between pits. This is contrary to results obtained employing MOCVD. The difference in optimal buffer layer conditions may be due in part to the higher growth temperatures employed by MOCVD as well as the significantly different surface conditions present during MOCVD growth compared to MBE. It is not surprising that significant differences in optimal buffer layer parameters exist between these two very different growth methods. As will be discussed in the next section, the optimal growth conditions for MOCVD growth of GaN are extremely nitrogen rich, while growth under even slightly nitrogen rich conditions during MBE growth results in very poor surface morphology. In particular, surface mobility is enhanced at higher growth temperatures. It has been shown that the Ga polar GaN surface becomes very smooth when annealed at high temperatures, while the N polar face becomes rough. This is the main reason for the strong preference towards Ga

polar material for MOCVD growth, and perhaps why nitrogen rich conditions can be employed during growth employing this growth method. Given MBEs more modest growth temperature, both polarities can be grown with similar crystal quality. Unfortunately, lower temperatures do not take advantage of GaNs tendency to flatten out at high temperatures. Some temperature considerations relevant to growth are discussed in the next section.

3.9 Temperature Limits of Growth

As indicated earlier by the decomposition temperatures of the various nitrides, the temperature at which MBE growth can be carried out for each of the nitrides is significantly different. Aluminum nitride can be grown easily at temperatures from 750 °C to upward of 1000 °C with a streaky RHEED pattern throughout if metal rich conditions can be maintained. This can be difficult given that aluminum's residency time on the surface is quite short at temperatures above 900 °C. Unlike the extremely stable AlN, InN decomposes rapidly above 650 °C. Indium nitride is found to relax immediately when deposited on GaN. Figure 3.6 shows the RHEED of ~5 Å of InN deposited at 480 °. The RHEED is stable for extended periods with the indium shutter closed; however, ramping the growth temperature back up to 550 °C results in removal of the InN layer and RHEED reverts to a GaN pattern. This was repeated multiple times to determine the maximum temperature at which the InN was stable. At higher temperatures, the RHEED reverts quickly to a GaN pattern, but at ~520 ° it appears relatively stable. At these low temperatures, indium' s reevaporation rate is extremely low. This can lead to formation of In droplets on the surface if the nitrogen arrival rate, and subsequent indium incorporation into the InN film, is too low. Growth under nitrogen rich conditions, however, leads to spotty and faceted RHEED patterns. These two difficulties make the window of optimum growth conditions very narrow.

GaN does not show a tendency to decompose rapidly like InN and can be grown at relatively high temperatures. This results is a lower tendency to form metal droplets. Typical growth temperatures are between 700 °C and 850 °C. Growth at lower tem-

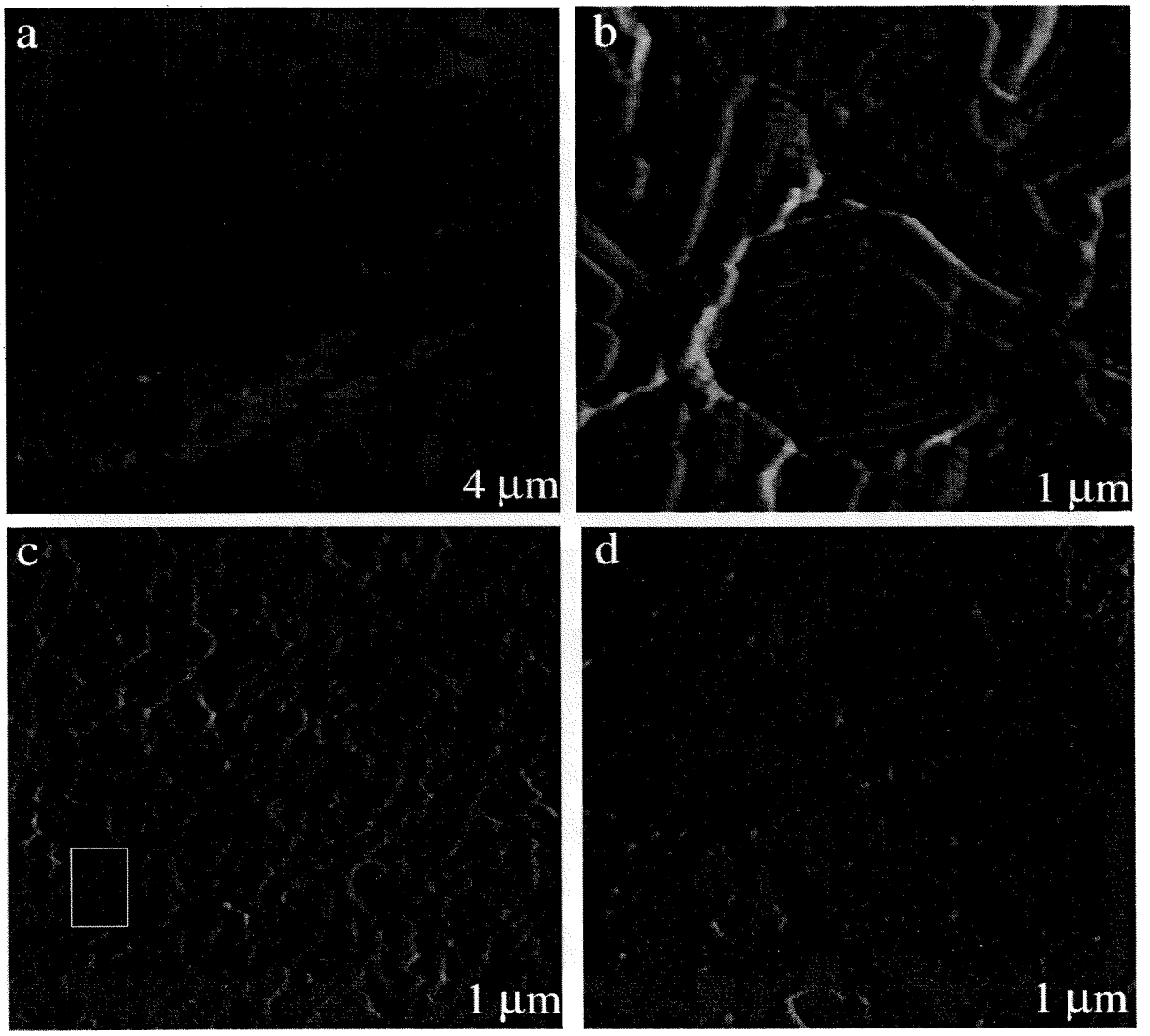

Figure 3.5: These four AFM images of GaN samples show some of the improvements obtained by buffer layer optimization. RMS roughness is over entire scan area unless otherwise noted. a)High temperature nitrogen rich AlN buffer layer. 75nm full scale, RMS roughness excluding pits 1.69nm, b)Low temperature Ga rich buffer layer. 5nm full scale, RMS roughness .358nm (.081nm in box), c)High temperature Al rich buffer layer. 2nm full scale, RMS roughness .066nm (.045nm in box), d)MOCVD grown GaN with low temperature GaN buffer layer. 1nm full scale, RMS roughness .018nm

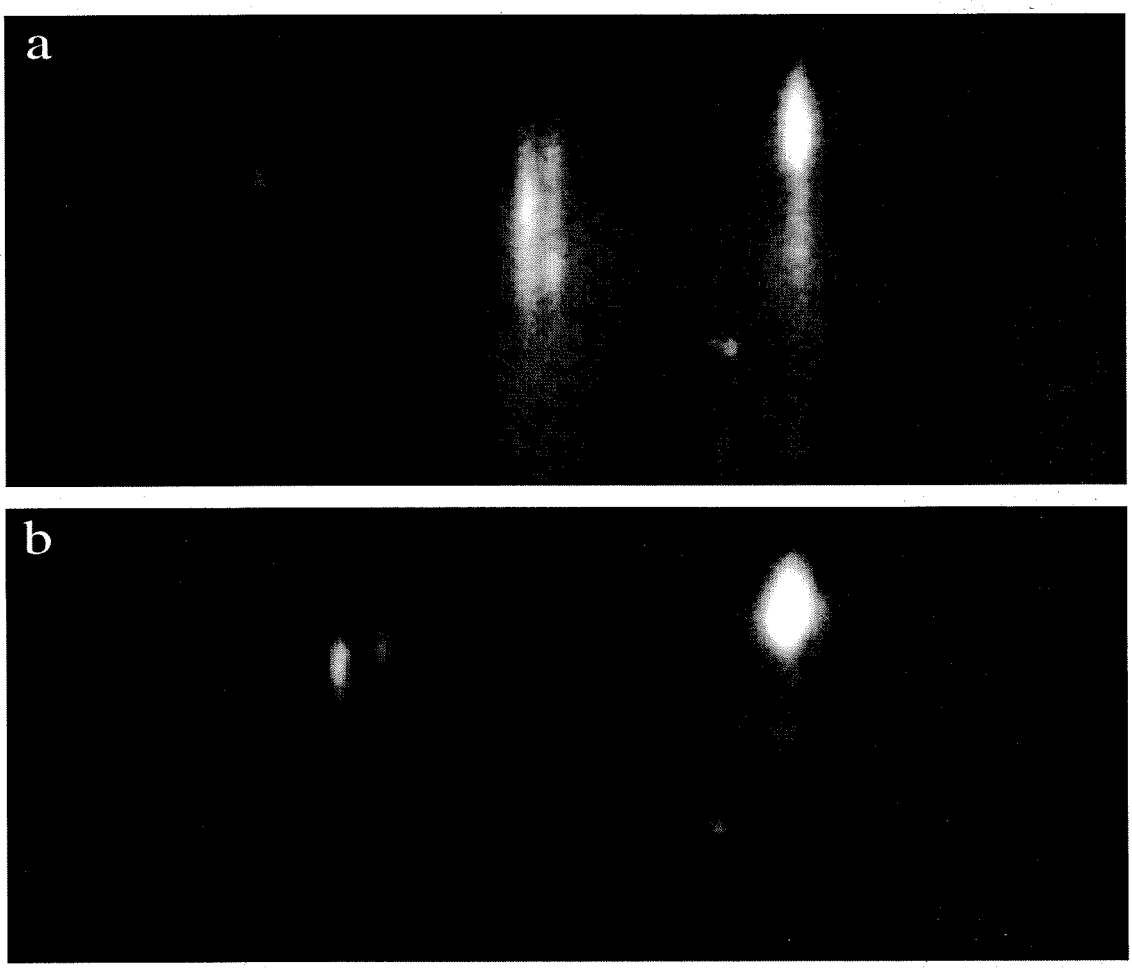

Figure 3.6: RHEED of relaxation of $\sim$5 ÅInN on GaN.

peratures, ~700°, leads to surface roughening due to lower surface mobility. Surface mobilities are also affected by the surface chemistry. It has been shown that the arrival rate of the metal and nitrogen constituents can drastically alter the growth mode during RF-MBE. The effect the stoichiometry of the arriving materials has on morphologies is discussed in the following chapter.

3.10 V/III ratio and morphology

As mentioned above for InN, GaN morphology is highly dependent on the ratio of gallium to nitrogen fluxes arriving at the growing surface. It has been reported that the mobility of Ga atoms on a Ga terminated surface is much higher than the mobility of Ga atoms on a N terminated surface.[30] Therefore, growth under gallium rich conditions results in Ga terminated surfaces, and Ga atoms on the surface have time to hop to low energy binding sites such as step edges. Growth under nitrogen rich conditions, however, results in immediate incorporation of the gallium and statistical roughening of the surface. This is clearly observed in the RHEED pattern during growth. Nitrogen rich growth leads to spotty and faceted RHEED patterns; while slightly Ga rich conditions can maintain streaky RHEED patterns for many hours. In addition, the brightness of the RHEED streaks is indicative of the III/V ratio on the growing surface. The intensity of RHEED dims with increasing Ga and brightens when Ga is shuttered, allowing incorporation and reevaporation of the gallium on the surface. The time required to completely incorporate or evaporate the metal on the surface is an indication of the current stoichiometry on the surface during growth. Also, puddle formation can be checked in this manner. If Ga droplets have formed on the surface, nitridation of tens of minutes is required to achieve brightening of the RHEED pattern. This is due to continued wetting of the surface from excess gallium in the puddles. Unfortunately, once puddles have formed, there is no effective way of recovering a smooth surface other than extended growth times. The long nitridation times required to incorporate all the puddled gallium results in roughening of the surface and spotting in the RHEED pattern. The response of the RHEED pattern to

nitridation is shown in figure 3.7. The best growth conditions are those that result in brightening in approximately 10 seconds. Shorter brightening times or conditions in which the RHEED does not dim under Ga flux result in rough surfaces due to nitrogen rich conditions. Longer times often lead to Ga droplet formation.

The luminescence properties of GaN are also highly dependent on the stoichimetry of growth. Figure 3.8 shows the cathodoluminescence spectrum of GaN under different growth conditions. Stoichiometric growth leads to an increase in the so called yellow luminescence (YL) from GaN. Nitrogen rich conditions, in fact, can lead to complete quenching of the band gap recombination seen at 366nm. Slightly metal rich conditions, however, lead to greatly reduced YL intensity. This is consistent with the hypothesis that YL is related to Ga vacancies.[31] However, it does not rule out the possibility that defects are responsible given that crystal quality also degrades with nitrogen rich growth conditions. Also shown in figure 3.8 is the CL of a GaN layer capped with 300 Å AlN layer. This may be related to recombination of carriers within the two-dimensional electron gas at the AlN-GaN interface with holes generated by the impinging high energy electrons. Alternatively, residual strain in the AlN layer may cause a shift in the AlN recombination energy resulting in the extra peak centered around 430nm. The peak at 315nm in the AlN spectrum is not present in the cap layer sample; however, this makes assigning the extra peak in the cap layer sample to AlN more dubious.

Figure 3.9 shows the dependence of morphology on V/III ratio during growth. As can be seen in 3.9a, nitrogen rich growth leads to small grain rough surfaces as expected from a statistically roughened surface. Increasing the Ga flux to approximately stoichiometric conditions results in larger flat grains with some valleys surrounding the mesa shaped gains. Increasing the metal to nitrogen ratio further, to slightly Ga rich, results in very flat surfaces; droplet formation, however, limits the V to III ratio employable. Figure 3.9d is a schematic diagram of optimal growth conditions verses growth temperature. Low temperatures result in a narrower growth window. While higher temperatures result in better surfaces, growth rate slows considerably due to the increased decomposition of the GaN and high reevaporation rate of the Ga on the

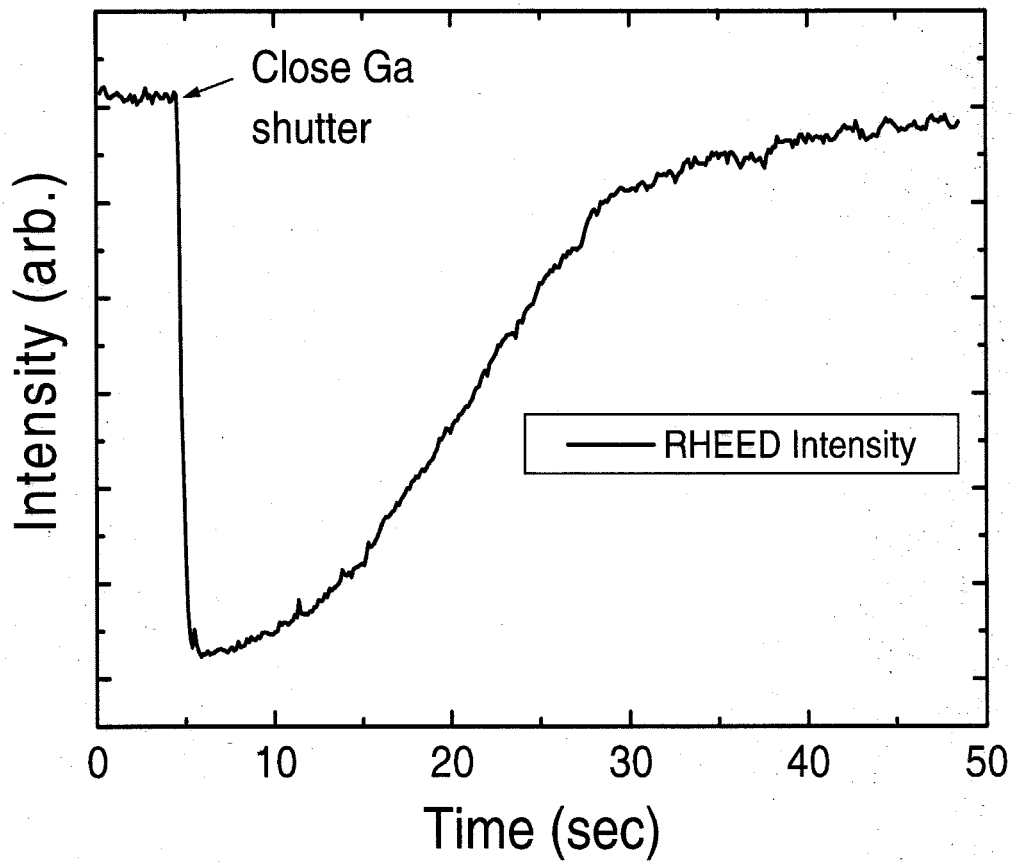

Figure 3.7: Brightening of RHEED after shuttering Ga during slightly Ga rich growth of GaN.

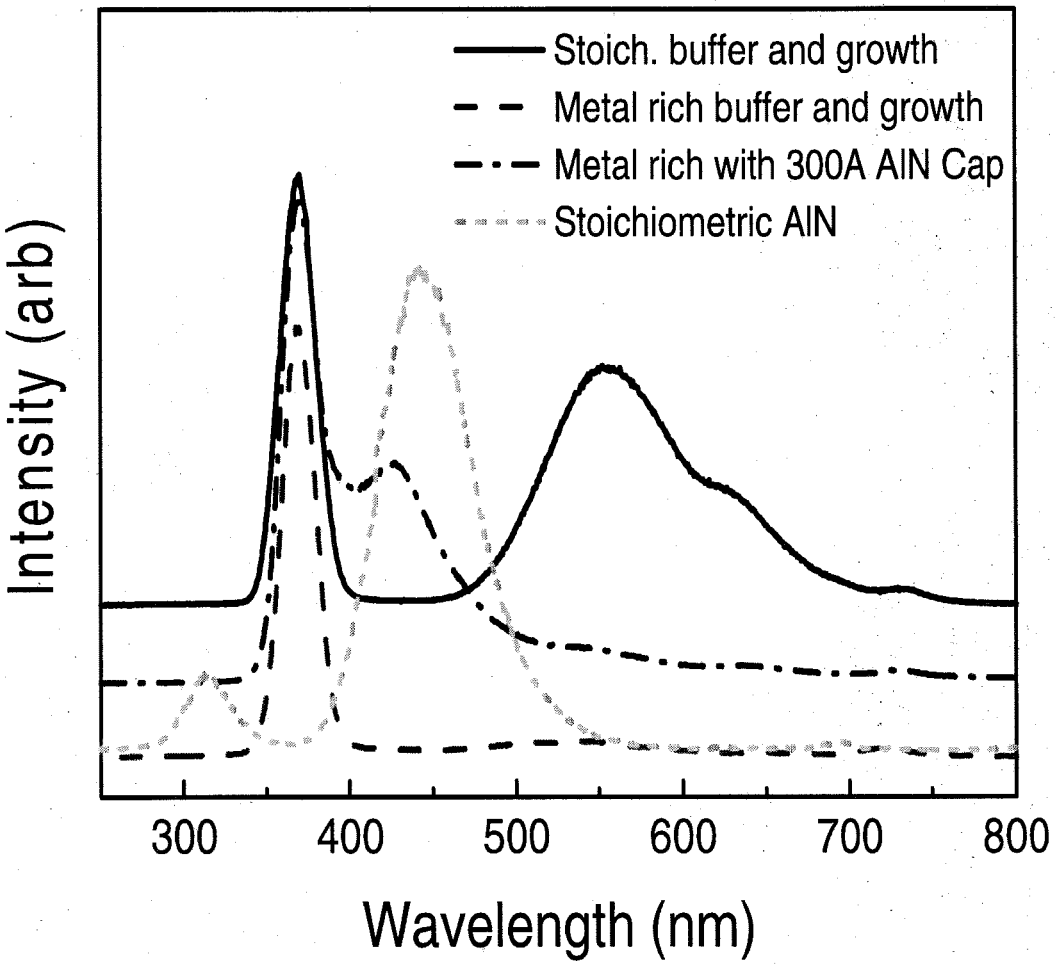

Figure 3.8: Compairison of room temperature CL as a function of growth conditions.

surface. The AFM image of figure 3.9c contains many pits decorating the edges of the hexagonal grains. As discussed earlier, it is believed that these pits are associated with the growth initiation process.

Achieving optimized growth conditions during all the steps of GaN growth is extremely difficult, but high quality material is achievable using MBE and sapphire substrates. Figure 3.10 compares the x-ray diffraction patterns of three samples, two grown by MBE here at Caltech and the other by MOCVD at the University of Wisconsin. Although neither sample is the best reported in the literature, the comparison is an attempt to remove growth experience from the evaluation of the two growth techniques. As can be seen in the figures, the crystal quality of MBE grown material can be similar to that of MOCVD. Both MBE samples were grown in the metal rich regime but with growth nucleated at two different temperatures. Slight improvement is obtained from higher temperature buffer layers. Of particular interest for electronic applications is the $(11\bar{2}4)$ peak. Off c-axis diffraction peaks are important for determining the pure edge dislocation density. And it has been observed that mobilities in GaN track with the intensity and width of the off axis diffraction peaks. As seen in figure 3.10c, the low temperature buffer layer sample grown by MBE has a slightly less intense $(11\bar{2}4)$ diffraction peak but does show a 45% reduction in width compared to the MOCVD sample. The high temperature buffer layer sample is significantly more intense than either of the other samples and has the narrowest full width at half max. Figure 3.10 shows an XRD scan of the (0002) peak of an $Al_{.03}Ga_{.97}N/GaN/Al_{.03}Ga_{.97}N/GaN$ sample. The intensity oscillations indicate very smooth surfaces, and from their spacing the thickness of the intermediate GaN layer can be determined, and hence growth rate can be calculated. For this sample we grew at $0.33\,\mu$m/hr. Control of alloy incorporation is important for applications involving heterostructures such as heterojunction field effect transistors. Growth of AlGaN alloys is discussed in section 3.11.

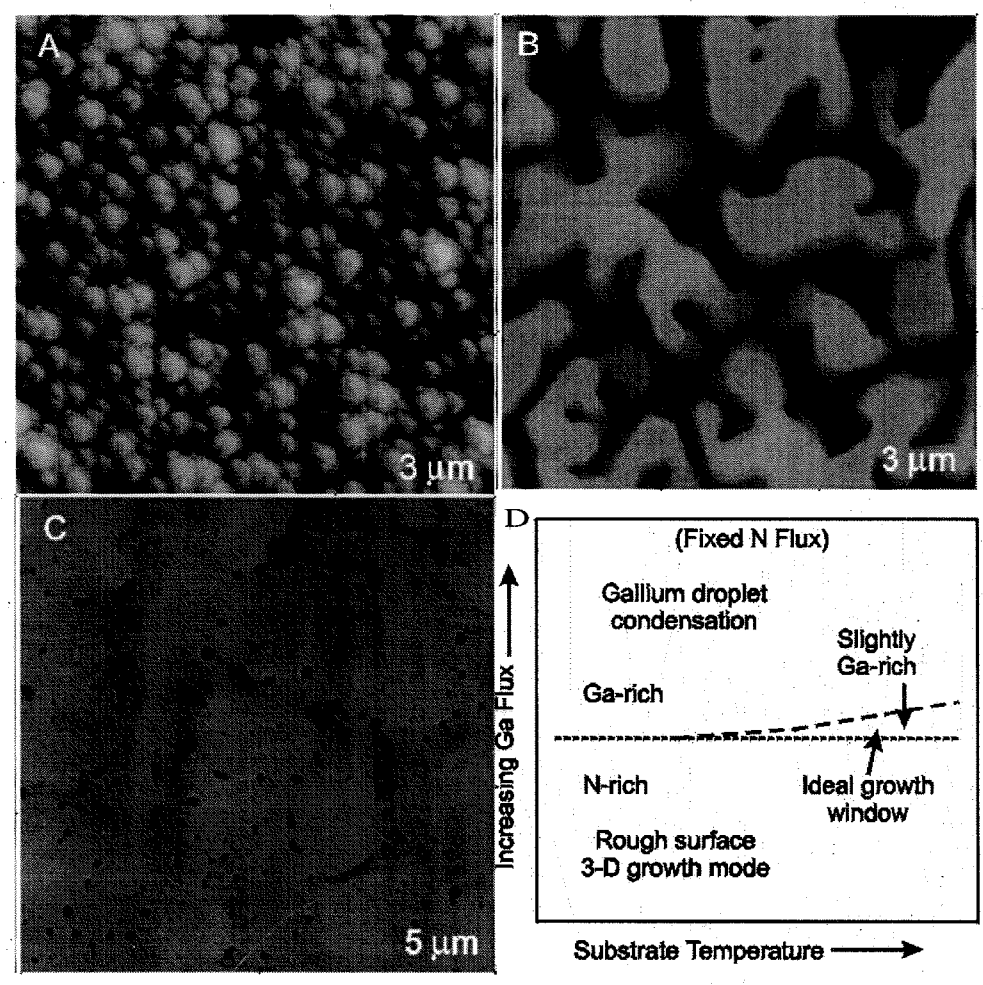

Figure 3.9: Growth stoichiometry and film morphology.

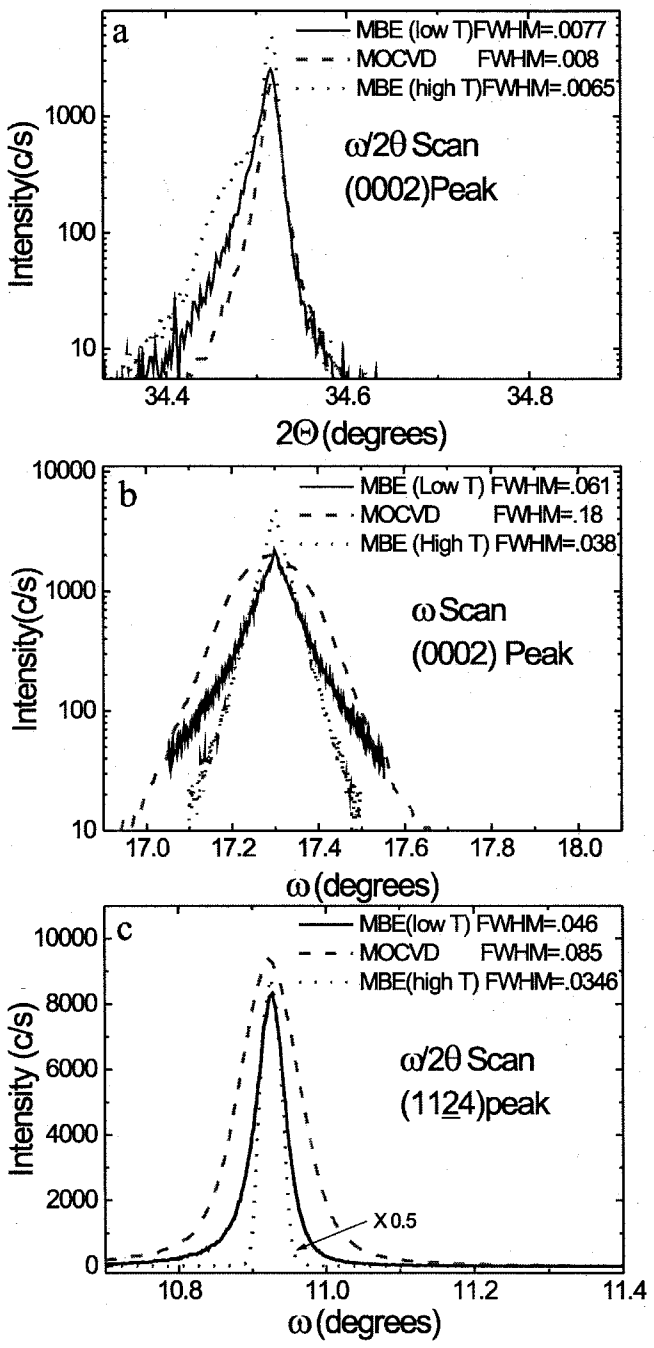

Figure 3.10: Comparison of x-ray diffraction peaks from MOCVD and MBE samples.

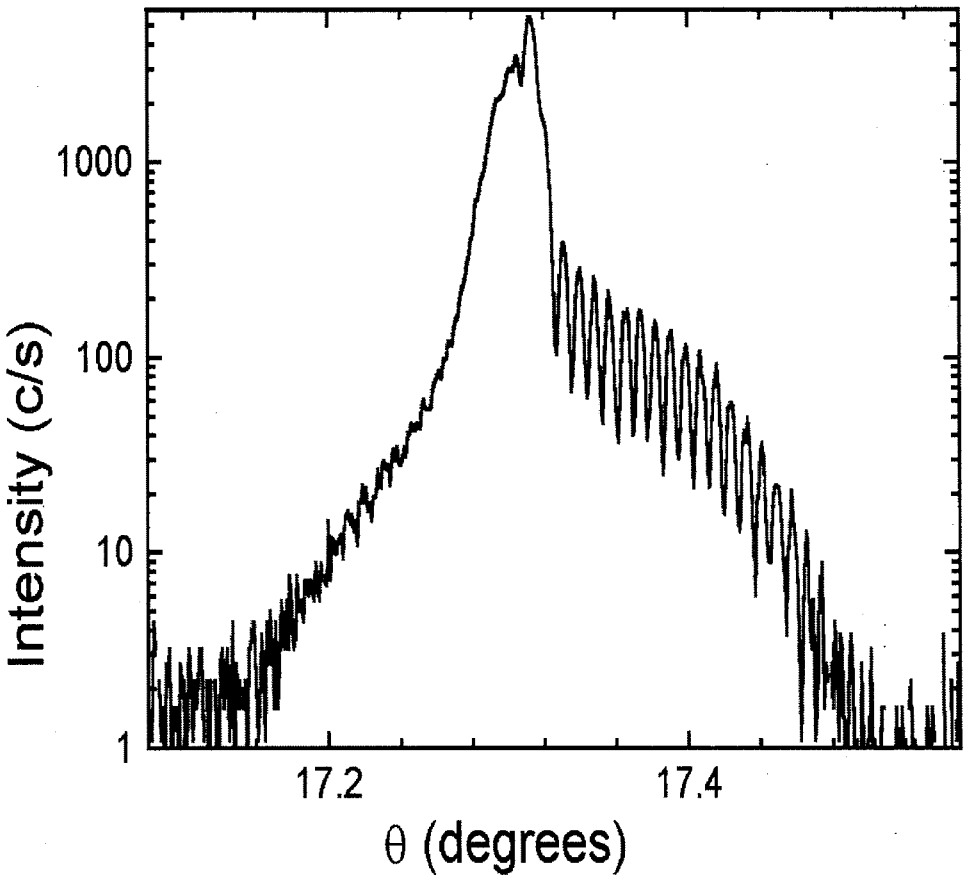

Figure 3.11: Interference oscillations from an $Al_{.03}Ga_{.97}N/GaN/Al_{.03}Ga_{.97}N$ structure.

3.11 Growth of Alloys

A number of AlGaN alloys have been grown with various Al contents. The Al content was found to vary exponentially with Al cell temperature. Incorporation of the Al was found to be preferential over incorporation of Ga under standard growth conditions. During growth, the Ga cell temperature was controlled to produce slightly metal rich conditions. At the end of growth, both metal shutters are closed simultaneously, and the film is allowed to cool under nitrogen exposure. XPS of the alloy films showed a significantly higher Ga content in the top ~10 Å then in the bulk films. As an example of this, a thick sample of AlGaN with Al content of 12% as determined by XRD showed only 6.5% Al in XPS with a decrease in Al peak intensity with higher angle indicating an Al deficiency near the surface. This indicates that although the surface is covered by a thin layer of metal during growth, the Al within this layer is preferentially incorporated into the growing nitride film. The Al content of some AlGaN films is shown in figure 3.12 versus the Al cell temperature.

3.12 Growth of InN

As discussed earlier, growth of InN is performed at much lower temperature than GaN, and the window of optimal growth conditions is expected to be much smaller than that of GaN. Growth of InN by vapor phase techniques is hampered by the low decomposition temperature of InN. The nitrogen source for these techniques relies on the decomposition of ammonia at the growth surface. Since InN must be grown at lower temperatures than GaN, the decomposition rate of the ammonia is very low. This leads to slow growth rates and a high level of nitrogen vacancies in the films. This is believed by some to be the cause of the high level of native n-type doping in InN films. Others attribute the high level of doping to decomposition of the InN and subsequent loss of nitrogen from the bulk. Figure 3.13 shows the x-ray diffraction from three InN samples grown under conditions similar to optimal growth conditions for GaN, i.e., the In cell temperature is raised to produce slightly metal rich growth

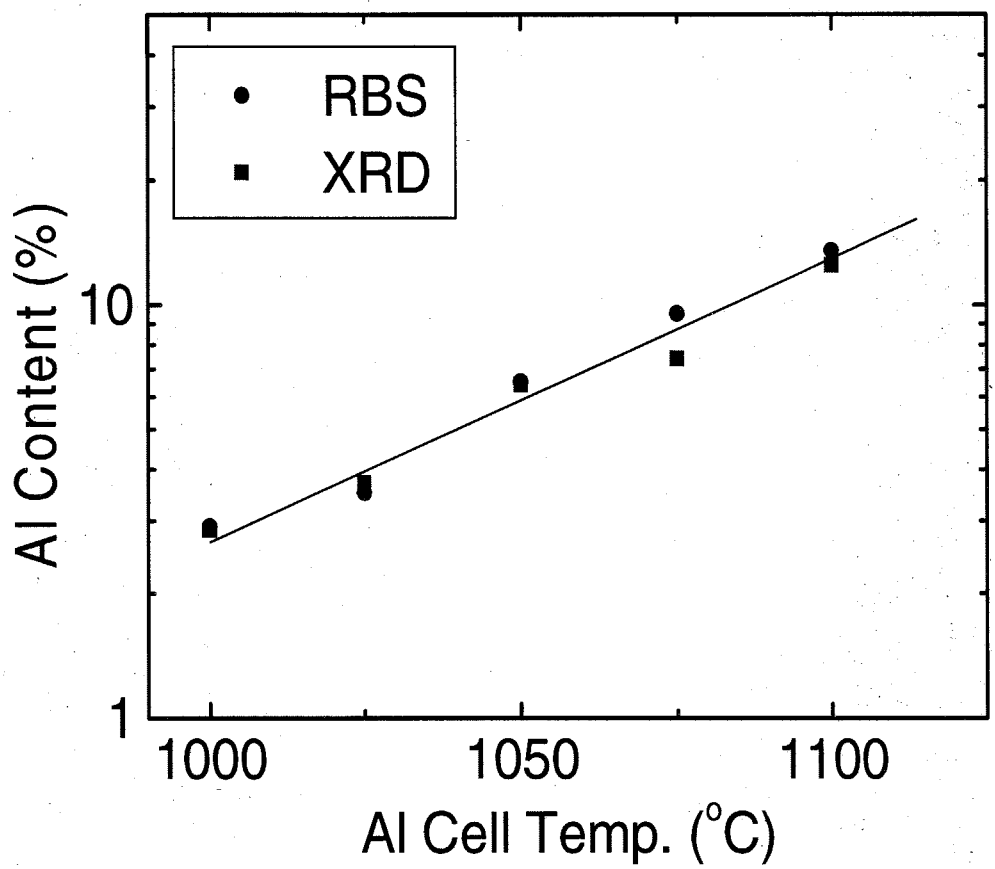

Figure 3.12: Al content in AlGaN ternary compounds verse Al cell temperature with gallium main cell temperature set to ~880 °C and gallium lip temperature at 1100 °C. 1-2 deg changes in Ga main temperature were made to maintain proper V/III ratios for higher Al cell temperatures.

conditions. This is determined by the transition of the RHEED pattern from spotty and bright to streaky and slightly dim. Samples N089 and N108 where grown on GaN/sapphire. Sample Ce2 was grown on CeO_2 deposited on (111) Si substrates.

CeO_2 was investigated as a substrate for InN growth to determine if a nitridation step similar to the nitridation of sapphire could be employed to produce a thin layer of CeN. CeN is a cubic material with a rock salt crystal structure with lattice constant 5.0245 Å. The atom spacing in the (111) plane of CeN is 3.55 Å, which is close to InNs lattice constant of 3.54 Å, resulting in 0.3% inplane mismatch. N089 and N108 were grown at 480 °C and 350 °C respectively. As can be seen in the XRD scans, the widths of the peaks improved greatly with increased temperature, approaching values similar to those of GaN samples. Interestingly, the InN grown on CeO_2 contained significant amounts of the cubic phase of InN. This may be related to the rough surfaces obtained during deposition of the CeO_2 on Si. Growth initiated along one of the exposed cubic planes may stabilize the cubic form of InN. This may indicate that growth on one of the other orientations of CeO_2, such as (100), or (110), may result in cubic InN. We currently have had limited success in growing high quality thick CeO_2, so those studies have yet to be performed, but further investigation of this substrate for InN growth may be interesting.

The AFM images shown in figure 3.14 are from the InN samples grown on GaN. Figures 3.14a-c are a zoom in sequence on a large, $\sim 2\,\mu$m, plateau region on sample n089. Figure 3.14d is from sample n108. The morphology of both samples is quite rough with rms roughness of $\sim$ 30, 15, 4, and 10nm for figures a-d respectively. Sample n089 shows many large grains surrounded by canyons on a large scale. Zooming in to the relatively flat surface of one of the large grains shows an interesting pattern of small pits on the order of 15nm deep that appear to be arranged in a hexagonal pattern. This may be due to the initial relaxation of the InN when first deposited on the highly mismatched GaN substrate. N108 also displayed mountainous morphology, but on a slightly reduced scale. Figure 3.14 shows AFM images of the InN deposited on the CeO_2 substrate. The sample is characterized by a high density of small crystallites, $\sim 0.5\,\mu$m in diameter. These crystals show hexagonal symmetry and a high

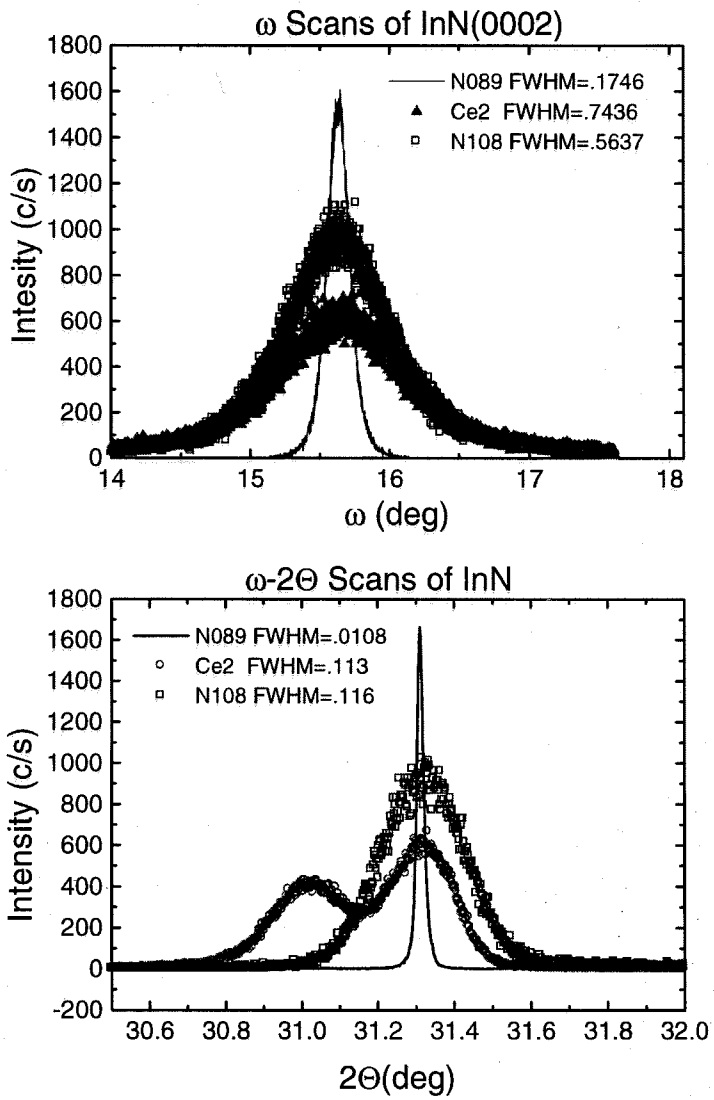

Figure 3.13: X-ray diffraction scans of InN grown on GaN and CeO_2.

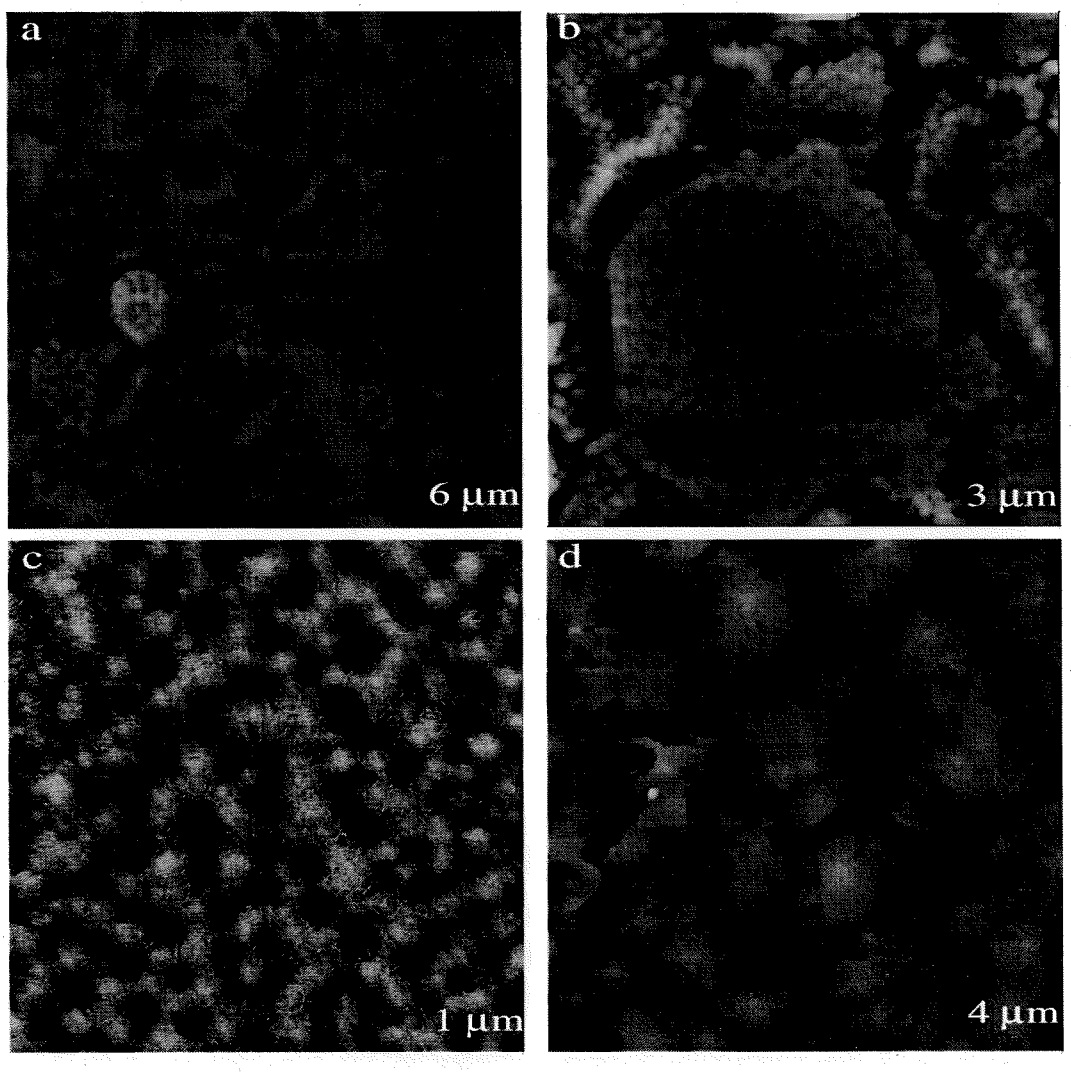

Figure 3.14: AFM comparison of InN samples grown on GaN.

degree of orientation. The sharpness of the crystal edges indicates good mobility of the surface atoms during growth, but may indicate a higher mobility for planes other than the (0001) or (111). This is similar to MOCVD growth of GaN where the chemistry and temperature can be controlled to produce preferential growth along alternative planes. This has been used to produce hexagonal pyramids with very sharp peaks in the hopes of producing field emission tips. The AFM images here suggest the same type of enhancement of the mobilities along vertically inclined planes.

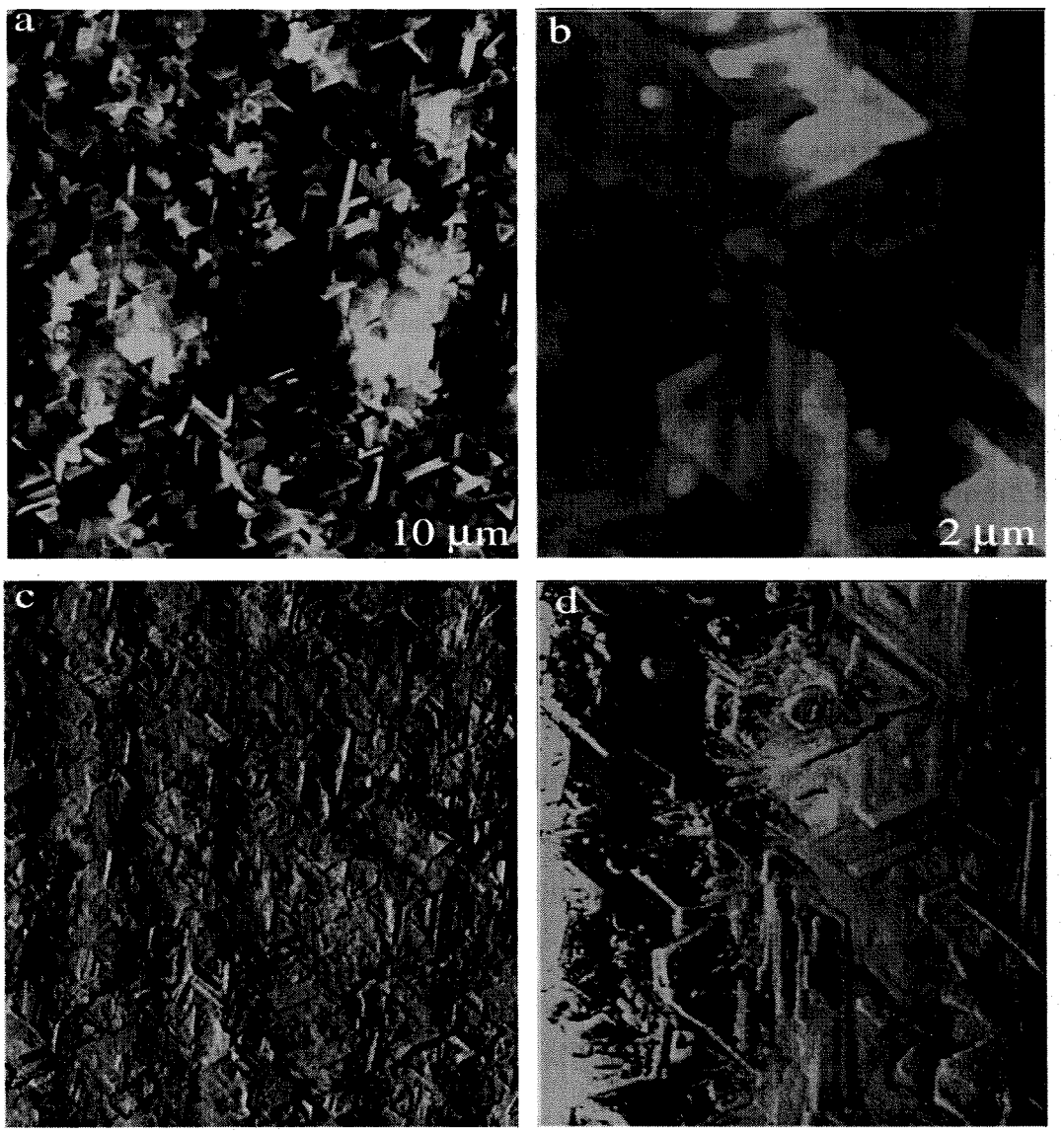

Figure 3.15: AFM comparison of InN samples grown on CeO_2. a and c are height and phase of a 10 μm area showing the crystalite and hexagonal orientation of sample. b and d are height and phase of a 2 μm area, showing the sharp edges steps of these crystalites.

3.13 Chapter Summary and Conclusions

Column III nitrides have been grown by RF-MBE on sapphire substrates. Crystal quality and surface morphology has been studied as a function of buffer layer and growth conditions using AFM, XRD, and CL. It was found that the stoichiometry of the AlN buffer layer played a prominent role in determining the quality of the resulting GaN films. In particular, pit density in films grown employing metal rich buffer layers was significantly reduced. In addition, XRD performed on these samples showed improved peak widths with approximately a factor of two improvement in the symmetric (0002) ω and ω-2Θ peak widths. Off axis peak widths for samples with metal rich buffer layers were found to be on par with samples grown by MOCVD. The film morphology was investigated to determine the effects of the gallium to nitrogen flux ratio during growth. It was found that the surface flatness continued to improve as the Ga flux was increased up to the point at which Ga droplets began to form. Super lattice type interference oscillations were observed in double heterojunction samples employing optimized metal rich growth of both the buffer layer and main layer material indicating a high degree of interface flatness. Growth employing this methodology resulted in very smooth surfaces with rms roughness on the order of 0.1nm which is approaching that of MOCVD material.

Indium nitride was grown on GaN/sapphire, as well as on CeO_2/Si(111). It was determined that InN was stable up to $\sim$520 °C by observing the relaxation of InN on GaN using RHEED. X-ray diffraction was used to determine that growth temperature near the decomposition temperature of InN result in narrower peak widths. The InN/GaN film morphology was found to be very rough in our samples, on the order of 10's of nm. InN/CeO_2 resulted in a high density of small crystallites with diameters of $\sim$0.5 μm. These crystals showed a high degree of orientation and distinct hexagonal symmetries. In addition, growth of InN/CeO_2 resulted in significant amounts of cubic InN. This may prove to be a reliable method of integrating Si with InN if high quality InN growth can be developed.

Bibliography

[1] S. Porowski, MRS Internet J. Nitr. Semi. Res.**4S1**, G3.10 (1999).

[2] D. Smith, S. Tsen, B. Sverdlov, G. Martin, and G. Markoc, Solid State Elec. **41**, 349 (1997).

[3] T. Lei, K. Ludwig, and T. Moustakas, J. Appl. Phys.**74**, 4430 (1993).

[4] S. Tripathy, R. Soni, H. Asahi, K. Iwata, R. Kuroiwa, K. Asami, and S. Gonda, J. Appl. Phys.**85**, 8386 (1999).

[5] X. Wu, P. Fini, B. Heying, S. Keller, U. Mishra, S. DenBaars, and J. Speck, J. Cryst. Growth **190**, 231 (1998).

[6] S. Nakamura, M. Senoh, N. Iwasa, S. Nagahama, T. Yamada, and T. Mukai, Jpn. J. Appl. Phys. Pt. 2 **34**, L1332 (1995).

[7] S. Nakamura and G. Fasol, *The Blue Laser Diode* (Springer, Berlin, 1997).

[8] M. Murphy, B. Foutz, K. Chu, H. Wu, W. Yeo, W. Schaff, O. Ambacher, L. Eastman, T. Eustis, R. Dimitrov, M. Stutzmann, and W. Rieger, MRS Internet J. Nitr. Semi. Res.**4**, U851 (1999).

[9] Z. Bandic, P. Bridger, E. Piquette, and T. McGill, Appl. Phys. Lett.**74**, 1266 (1999).

[10] D. As, A. Richter, J. Busch, M. Lubbers, J. Mimkes, and K. Lischka, Phys. Stat. Solidi A **180**, 369 (2000).

[11] Y. Taniyasu, K. Suzuki, D. Lim, A. Jia, M. Shimotomai, Y. Kato, M. Kobayashi, A. Yoshikawa, and K. Takahashi, PHYSICA STATUS SOLIDI A-APPLIED RESEARCH **180**, 241 (2000).

[12] F. Semond, P. Lorenzini, N. Grandjean, and J. Massies, Appl. Phys. Lett.**78**, 335 (2001).

[13] S. Duan, X. Teng, Y. Wang, G. Li, H. Jiang, P. Han, and D. Lu, J. Cryst. Growth **190**, 197 (1998).

[14] A. Brown, W. Doolittle, S. Kang, J. Shen, Z. Wang, and Z. Dai, J. Elect. Mat. **29**, 894 (2000).

[15] V. Mamutin, A. Toropov, N. Kartenko, S. Ivanov, A. Wagner, and B. Monemar, Mat. Sci. Eng. B **59**, 56 (1999).

[16] R. Beresford, D. Paine, and C. Briant, J. Cryst. Growth **178**, 189 (1997).

[17] M. Kelly, R. Vaudo, V. Phanse, L. Gorgens, O. Ambacher, and M. Stutzmann, Jp. J. Appl. Phys Pt. 2 **38**, L217 (1999).

[18] H. Amano, M. Kitoh, K. Hiramatsu, N. Sawaki, and I. Akasaki, Jpn. J. Appl. Phys. Pt. 2 **28**, L2112 (1989).

[19] S. Nakamura, N. Iwasa, M. Senoh, and T. Mukai, Jpn. J. Appl. Phys. **31**, 1258 (1992).

[20] A. Ptak, K. Ziemer, L. Holbert, C. Stinespring, and T. Myers, MRS Internet J. Nitr. Semi. Res.**5**, U173 (2000).

[21] G. Namkoong, W. Doolittle, S. Kang, H. Sa, A. Brown, and S. Stock, MRS Internet J. Nitr. Semi. Res.**5**, 1 (2000).

[22] M. Losurdo, P. Capezzuto, and G. Bruno, J. Appl. Phys.**88**, 2138 (2000).

[23] S. Keller, B. Keller, Y. Wu, B. Heying, D. Kapolnek, J. Speck, U. Mishra, and S. DenBaars, Appl. Phys. Lett.**68**, 1525 (1996).

[24] S. Nakamura, Jpn. J. Appl. Phys. **30**, L1705 (1991).

[25] X. Shen, T. Ide, S. Cho, M. Shimizu, S. Hara, H. Okumura, S. Sonoda, and S. Shimizu, J. Cryst. Growth **218**, 155 (2000).

[26] M. Murphy, K. Chu, H. Wu, W. Yeo, W. Schaff, O. Ambacher, J. Smart, J. Shealy, L. Eastman, and T. Eustis, J. Vac. Sci. Technol. B**17**, 1252 (1999).

[27] R. Dimitrov, M. Murphy, J. Smart, W. Schaff, J. Shealy, L. Eastman, O. Ambacher, and M. Stutzmann, J. Appl. Phys.**87**, 3375 (2000).

[28] E. Hellman, MRS Internet J. Nitr. Semi. Res.**3**, 1 (1998).

[29] A. Smith, R. Feenstra, D. Greve, M. Shin, M. Skowronski, J. Neugebauer, and J. Northrup, Appl. Phys. Lett.**72**, 2114 (1998).

[30] T. Zywietz, J. Neugebauer, M. Scheffler, J. Northrup, and C. Van de Walle, MRS Internet J. Nitr. Semi. Res.**3**, 1 (1998).

[31] J. Neugebauer and C. VandeWalle, Appl. Phys. Lett.**69**, 503 (1996).

Chapter 4 X-ray Photoelectron Spectroscopy Studies of GaN Surfaces and Interfaces

4.1 Principles of XPS

In X-ray Photoelectron Spectroscopy, a sample is excited using x-rays and the energy spectrum of the photoexcited electrons emitted from the sample is measured. XPS is one of a number of spectroscopies based on the photoemission of electrons from solids developed by Kai Siegbahn and coworkers at Uppsala University,[1] collectively referred to as Electron Spectroscopy for Chemical Analysis (ESCA). XPS is distinguished from other electron spectroscopies by the energy of the photons used for excitation. Photons of energy 100-10,000 eV are employed for XPS. There are two types of x-ray sources commonly used for XPS, synchrotron and elemental bombardment. Synchrotron radiation has the advantage of being continuously tunable, extremely intense, and has a very narrow line width. The limited number of synchrotrons and the difficulty of obtaining beam time, however, makes this type of source unwieldy for most researchers in the field. In addition, the availability of monochromators limits the photon energies to 10-300 eV. Most XPS research uses electron bombardment of a suitable element to produce x-rays of the desired energy. Most commonly used are Al and Mg x-ray sources. Mg and Al produce characteristic $K\alpha_{1,2}$ x-ray lines at energies of 1253.6 eV and 1486.6 eV with linewidths of 0.7 eV and 0.8 eV respectively. A monochromator can be employed to reduce the Al $K\alpha$ linewidth to 0.3-0.4 eV FWHM. We have used this type of source for the XPS studies presented here. The energy spectrum of the photoexcited electrons yields a map of the electronic density of states in the sample, modulated by photoelectric cross sections x-ray line width,

spectrometer resolution, and electric fields within the sample. In XPS, the binding energy of the photo-emitted electrons is expressed relative to a reference level, which for solid samples is taken to be the Fermi level of the spectrometer-sample system. The relevant energy relations for XPS are shown schematically in figure 4.1. The binding energy E_B is given by;

$$E_B = h\nu - T_{sp} + \phi_{sp} \tag{4.1}$$

where $h\nu$ is the photon energy, T_{sp} is the electron kinetic energy measured by the spectrometer, and ϕ_{sp} is the spectrometer work function. Also labeled in figure 4.1 are T_s, the electron kinetic energy immediately after photoexcitation, and ϕ_s, the sample work function.

Figure 4.2 shows a typical XPS spectrum from GaN (0001). Figure 4.2a is a survey spectrum showing the many core level peaks as well as the characteristic LMM Auger peaks for GaN. Figure 4.2b is a high resolution scan of a GaN sample showing the lowest binding energy core level, the 3d doublet, and a continuous density of states around 3 eV corresponding to the valence band. The ability of XPS to excite electrons out of core levels in elements allows one to determine a great deal about the chemical makeup of a sample. Elemental compositions can be determined by comparing the relative intensities of core-level peaks for the different elements contained within the sample. In addition, information on the chemical bonding of the sample can be obtained by measuring energy shifts in the position of core levels for each constituent element.

Figure 4.3 shows the energy shift of a monolayer of Ga on a thick sample of GaN. A distinguishing feature of all electron spectroscopies is their high level of surface sensitivity owing to the short mean free paths of electrons traveling through solids. The main features of the XPS spectrum correspond to electrons ejected from the sample that have not lost energy due to inelastic scattering. Electrons that inelastically scatter before reaching the detector contribute to a broad background signal at higher binding energy (corresponding to lower electron kinetic energy) than

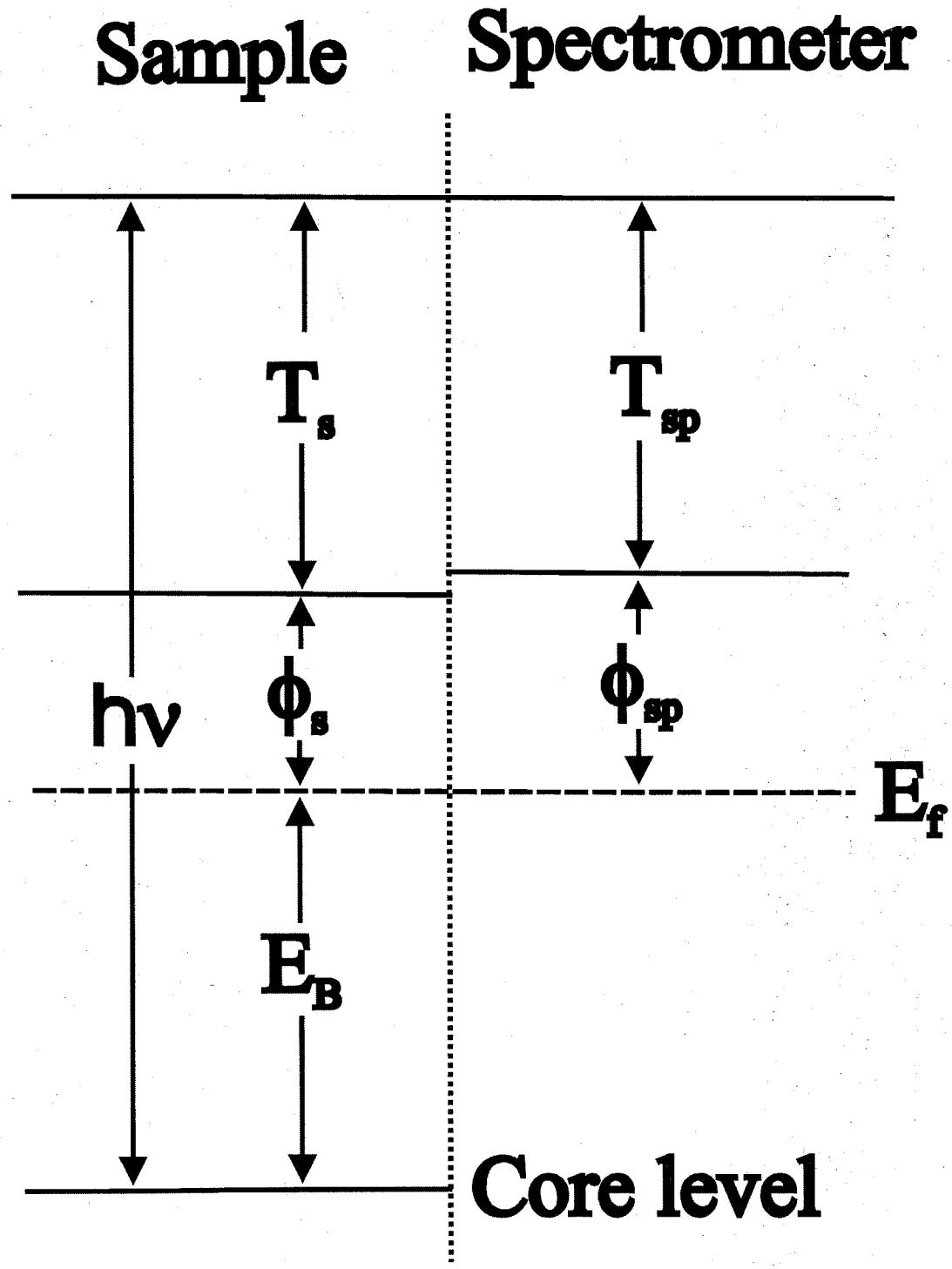

Figure 4.1: Schematic diagram of spectrometer-sample energy levels in x-ray photoelectron spectroscopy. ϕ_s and ϕ_{sp} are the sample and spectrometer work functions. T_s and T_{sp} are the electron kinetic energies immediately after photon absorption, and as measured by the spectrometer, respectively. E_B is the binding energy of the core level with respect to the Fermi level (E_f), and $h\nu$ is the incident photon energy.

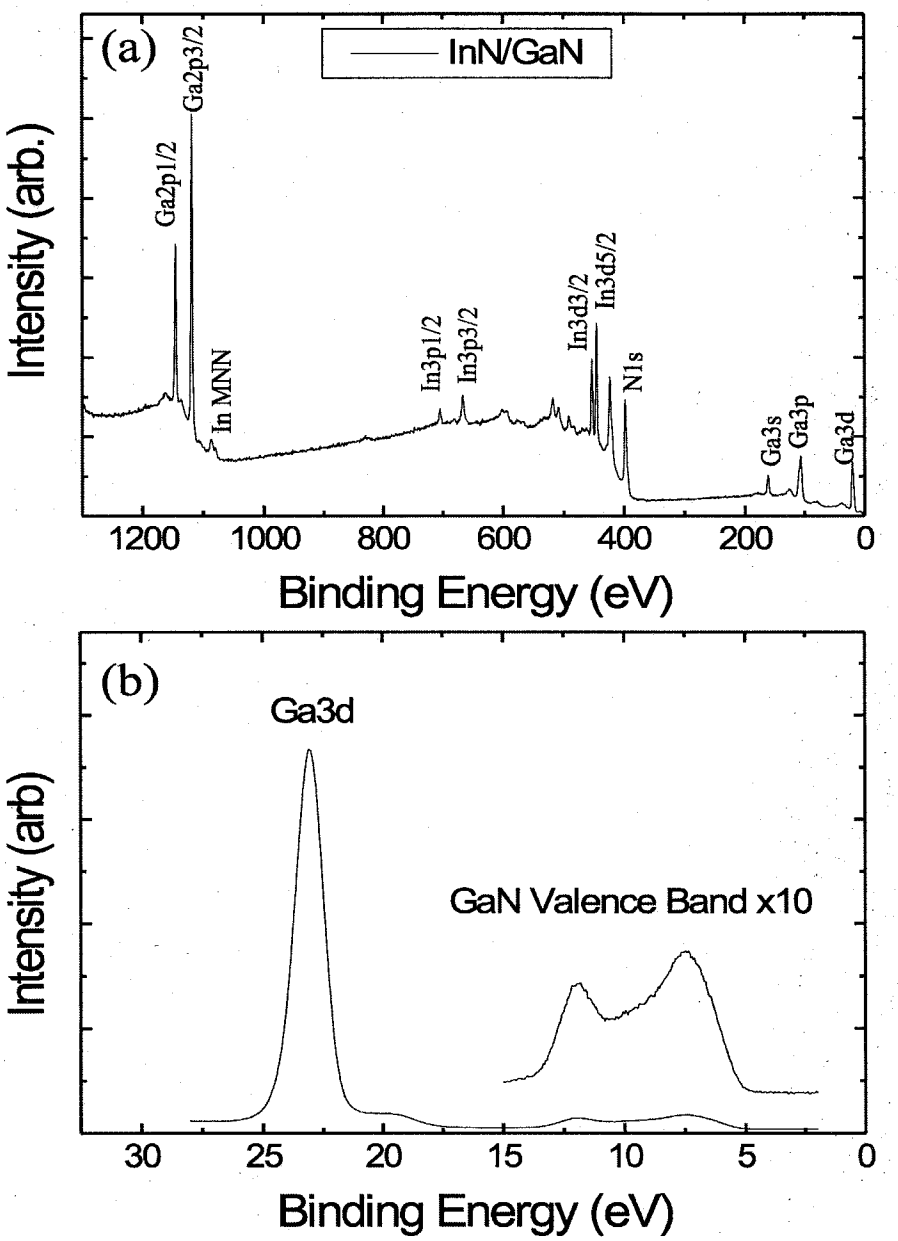

Figure 4.2: X-ray Photoelectron Spectroscopy data showing a) survey data of a thin layer of InN on GaN b) Ga3d and valence band from GaN sample.

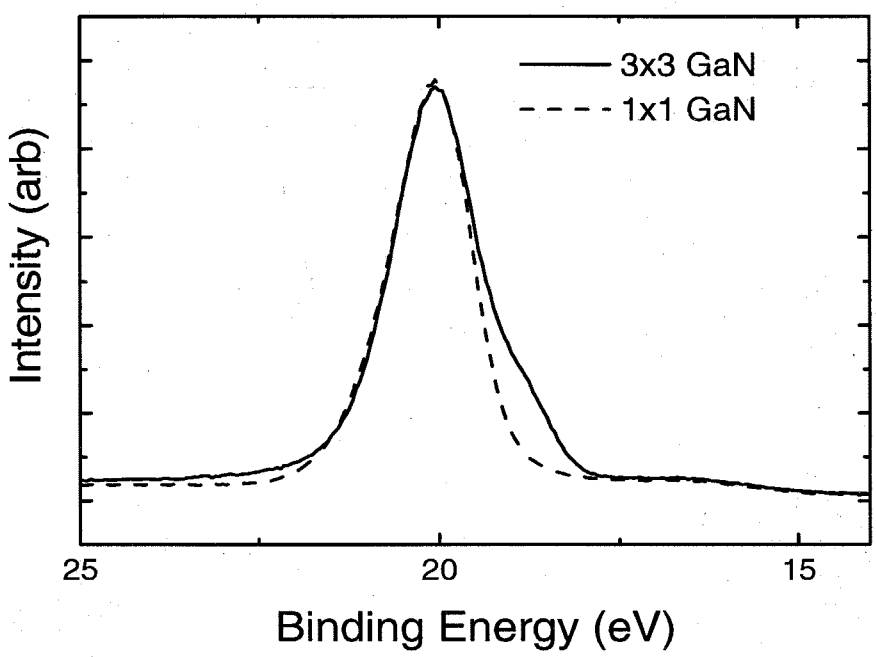

Figure 4.3: X-ray Photoelectron Spectroscopy data showing the energy shift of surface Ga atoms due to surface reconstruction from a 3x3 reconstructed GaN sample.

the state from which they were originally emitted. The resulting spectrum is therefore heavily weighted by contributions from surface or near surface atoms. For typical XPS experiments, with energies around 1400 eV, the escape depths are 10-30 Å, with the escape depth of semiconductors such as GaN being ~20 Å. Electronic escape depths are sensitive to the kinetic energy of the photoelectron. For ultraviolet photoelectron spectroscopy (UPS)in which the photoelectron energies range between 1 and 40 eV, electron escape depths of 5-10 Å are typical. UPS is therefore extremely surface sensitive. XPS, while still being sensitive to the surface chemistry, yields an electron energy spectrum that is essentially characteristic of the bulk material.

The surface sensitivity of electron spectroscopy necessitates the creation of ultra-high vacuum (UHV) conditions to maintain a clean surface for analysis. At pressures of 10^{-6} Torr, contaminants of unity sticking will accumulate on the sample surface at a rate of approximately on monolayer per sec. Therefore, UHV XPS chambers

are typically maintained at pressures of $\sim 10^{-10}$ Torr. Under these conditions, clean surfaces can often be maintained for several days. This does not however obviate the need for introducing a sample with a clean surface into the UHV environment. A number of methods for maintaining clean surfaces for introduction into XPS chambers have been developed and are discussed further in chapter 4.3.1.

4.2 Introduction

4.2.1 Background and motivation

Despite extensive theoretical efforts, band offsets in novel material systems cannot yet be predicted reliably using current theoretical techniques, and therefore must be determined experimentally. This has provided strong motivation for development of accurate yet relatively simple methods for measuring band offsets. A number of optical and electrical techniques have been developed to measure band offsets, however, most of these require growth of high-quality complex epitaxial structures which may not be feasible for novel material systems where growth technology has not had time to develop. In addition many electrical methods for determining band offsets require fabrication of functional electrical devices, and in fact, one may wish to measure the band offset for a given material system to determine if development of sophisticated growth and processing techniques is worthwhile. X-ray photoelectron spectroscopy (XPS) requires neither complex epitaxial growth, nor production of active electrical devices, and has been shown to be a reliable and accurate technique for measuring band offsets.[2, 3, 4, 5] The XPS technique requires only the growth of bulk material and simple heterojunctions, and gives a direct measurement of the valence-band offset. These two attributes make XPS an ideal tool for determining valence band offsets in novel material systems. This chapter includes XPS investigations into the band offsets of the column III-Nitride material system and surface reactivity of GaN.

4.2.2 Outline of Chapter

Section 4.2 discusses the basic principles of XPS and its application to investigations of semiconductor surfaces and interfaces. Section 4.3 describes the XPS based valence-band offset measurement; Section 4.3.1 presents the experimental procedures, while Section 2.3.2 explains the data analysis techniques employed to determine valence-band offset values. The chapter is summarized in Section 4.4

4.3 Measurement of Band Offsets by XPS

The determination of band offsets using XPS has a number of advantages over other band-offset measurement techniques. Unlike many optical or electrical methods XPS is a direct measurement of the band offset, so interpretation of the experimental results is straightforward. XPS also requires a relatively simple structure so fabrication of complicated devices is not required making it ideal for novel material systems with minimal growth technologies. This technique has been extended to include effects arising from strain in lattice mismatched systems.[6, 7]In addition, XPS can yield information about chemical reactivity at semiconductor heterojunction interfaces.[7]

XPS has been used by a number of investigators to study band offsets in a wide variety of material systems. Kraut, Grant, Waldrop, and Kowalczk [4, 5] developed the high precision analysis technique employed for XPS investigations of band offsets, and applied them to the Ge/GaAs,[8, 9] GaAs/AlAs,[10, 11] and InAs/GaAs [12]material systems. In addition, XPS has been used to measure band offsets in the nearly lattice-matched ZnSe/GaAs/Ge material system,[13, 14] InAs/GaSb heterojunctions,[15] and GaSb/AlSb heterojunctions.[16] Band offset measurements have also been reported for the Cd,Hg,Zn Te material system.[17, 18]

A number of nitride based devices have been successfully fabricated with outstanding performance characteristics. These devices however suffer from a high density of threading dislocations and other growth related electrical difficulties. This makes determination of band offsets employing electrical techniques difficult and makes the

use of non device related offset measurement techniques, such as XPS, attractive for determining offset values. To this end, we have undertaken an investigation of valence band offsets employing XPS.

4.3.1 Experimental Procedures

The measurement of band offsets by XPS relies on the ability to measure the energy separations of core-levels with respect to one another and to the valence band maximum. Figure 4.4 illustrates the method employed to measure valence-band offsets using XPS. A convenient core level in each material is chosen, and the core level to valence band maximum separation is measured for each material. A heterojunction is then grown with a thin overlayer approximately 25 Å thick. A thickness of 25 Å is large enough to ensure that the electronic structure of most of the top layer is characteristic of bulk material, [19, 20, 21]yet thin enough to allow significant contribution to the electron energy spectrum from the underlying layer. The energy separation between the two reference core-levels is then measured to obtain the valence band offset. Some considerations must be taken into account when choosing the reference core-levels to be used in the measurement. The atomic core level must be unique to a single constituent of the heterojunction, i.e. the N1s level would be a poor choice for determining the AlN/GaN band offset. The two core-levels should also be separated by at least a few eV in binding energy to avoid overlapping peaks in the heterojunction measurement. In addition, their binding energies should not be separated by much greater than 100 eV, since large separations can lead to greater uncertainties in the offset value calculated.

Figure 4.5 shows a set of XPS data used in the AlN/GaN valence-band offset measurement. As seen in the figure, the Ga 3d and Al 2p to valence band edge binding energies are determined in GaN and AlN respectively in figure 4.5c and a. The core level separations are then measured in an AlN/GaN heterojunction sample (figure 4.5b) consisting of $\sim$ 25 Å AlN grown on a thick sample of GaN typically 1 μm The valence band offset (ΔE_v) is given in terms of the measured separations

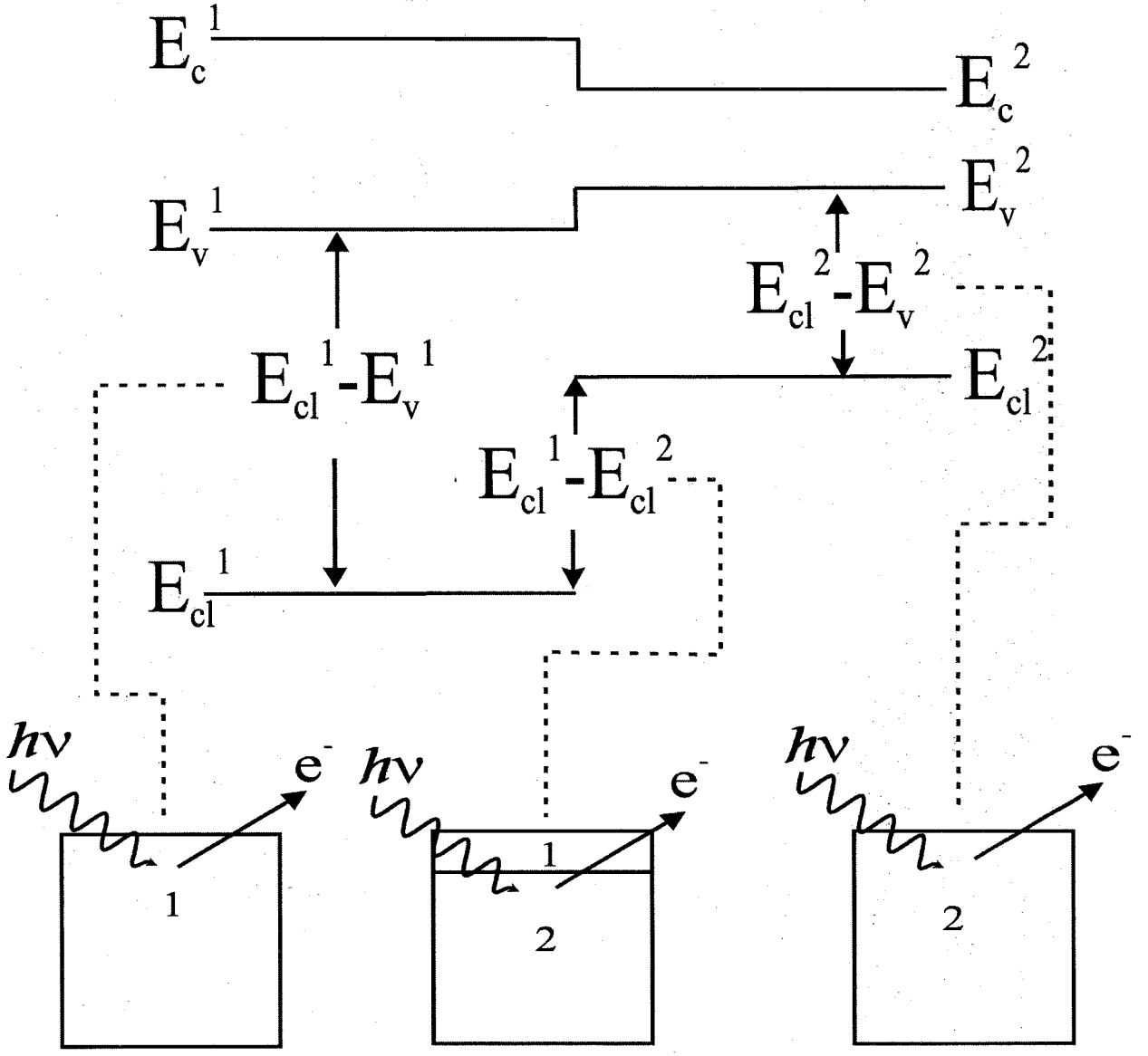

Figure 4.4: A schematic energy-band diagram illustrating the basic aspects of a band offset measurement employing XPS. Core-level to valence band maximum energy separations are measured in thick films of each material, the separation between reference core-levels are then measured in a heterojunction sample. These three quantities yield the valence-band offset.

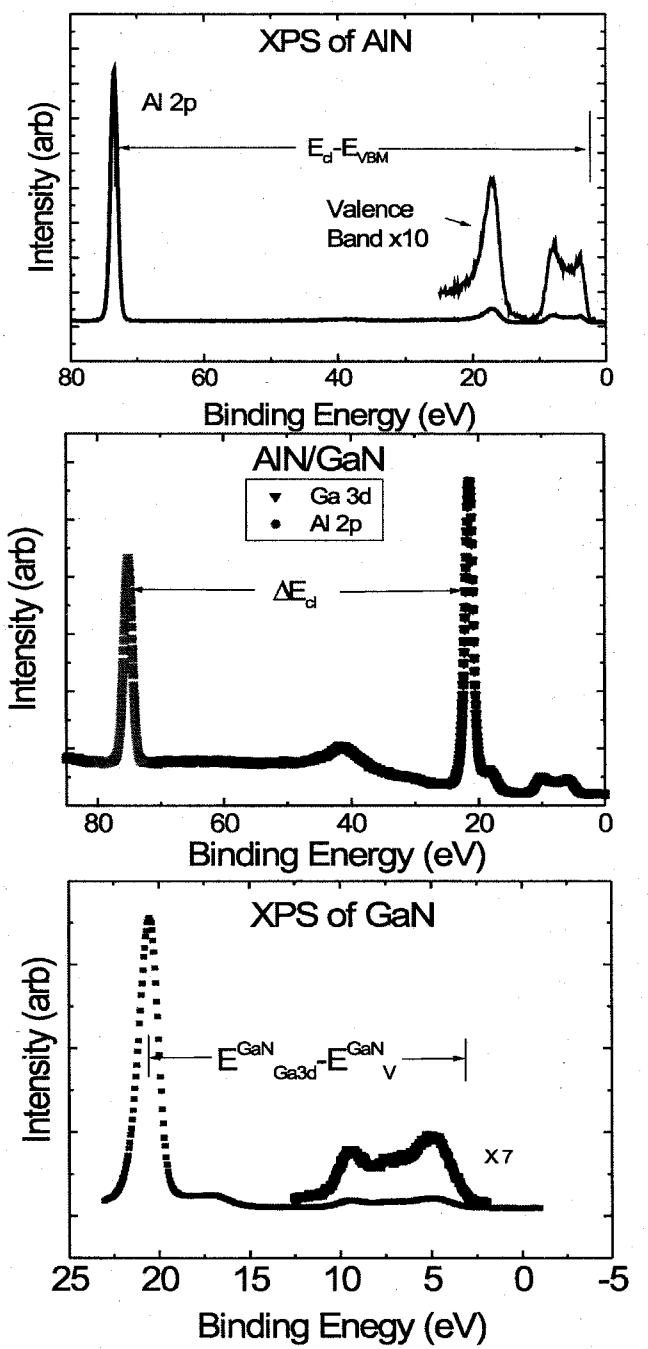

Figure 4.5: X-ray Photoelectron Spectroscopy data showing a)Al2p and valence band from AlN sample, b) Al2p and Ga3d core levels from AlN/GaN and c) Ga3d and valence band from GaN sample.

shown in figure 4.5a-c by;

$$\Delta E_v = (E_{cl}^1 - E_{cl}^2) + (E_{cl}^2 - E_v^2) - (E_{cl}^1 - E_v^1) \tag{4.2}$$

Where E_{cl}^i is the core level binding energy of semiconductor i, and E_v^i is the valence band maximum binding energy.

In principle the band offset should be independent of the order in which the interface is grown, i.e. a thin layer of AlN on GaN verse a thin layer of GaN grown on AlN, this property is known as commutativity of the band offset. Some investigators have claimed that growth sequence can effect the detailed atomic structure at the interface, and therefor the value of the band offset.[11] The existence of a growth sequence dependent band offset could have implications for the design of devices utilizing that heterojunction. Thus by checking for commutativity, one might obtain some idea of the structural and electronic quality of the grown interfaces.

Given the surface sensitivity of XPS, care must be taken to avoid surface and interface contamination. Formation of a surface oxide for example can lead to significant distortion of the valence band spectrum, as well as produce chemically shifted core-level peaks that alter the measured core-level binding energy. These two effects combine to produce erroneous measurements of the core-level to valence-band maximum energy separation. Similarly, contamination or other alteration of the heterojunction interface could yield shifted core-level binding energies, and thereby affect the core-level energy separation measurement.

To avoid complications arising from surface contamination, a number of methods have been employed for transferring samples from the growth to analysis chambers. One such method is a vacuum glove box. The sample is transferred into a detachable vacuum pumped chamber and moved from the growth chamber to the XPS chamber, where it is then reintroduced into the UHV environment. Another method that has been employed is a sacrificial cap layer. For GaAs, as an example, a layer of As is deposited on the surface after growth and cool down. After reintroduction of the sample into the XPS chamber, the As cap is evaporated from the surface by heating the

sample, thus removing the contamination from atmospheric exposure. Passivation is generally quite effective at protecting samples from atmospheric contamination. The heating required to remove the passivation layer can often cause mixing at reactive interfaces, however, such as in III-V/II-VI heterojunctions. Preferable to these techniques is a system with the XPS and other analysis tools attached via a UHV transfer tube to the growth chamber. This allows for characterization of the sample immediately after growth, and guarantees a clean sample surface. We have employed this type of sample handling for the XPS data presented in this thesis. Figure 4.6 shows the UHV system used to perform our sample growths and XPS measurements. As seen in the diagram, a III-N MBE system, II-VI MBE system, metalization chamber, Si-Ge MBE system, III-V MBE system, and XPS analytical chamber are connected via UHV transfer tubes. This avoids uncertainties associated with transfer of samples through atmosphere and the associated contamination.

Care must also be taken to prepare samples with appropriate doping. Low doping can cause sample charging, resulting in spurious peak shifts. The doping level must also be low enough that the band bending at the surface or interface is negligible over the sampling depth of XPS. The surface depletion length is given approximately by

$$W = \sqrt{\frac{2\varepsilon_s V_{bi}}{qN_d}} \tag{4.3}$$

For doping (N_d) of 10^{18} this leads to depletion widths of $\sim$ 230 Å for a built in voltage (V_{bi}) of 1 volt in GaN.(ε_s =10) This produces significant bending of the bands within the sampling depth of XPS ($\sim$ 100 Å). Undoped or lightly doped 10^{16} materials are usually conductive enough to avoid charging and minimize bending at the interface. As will be discussed later, InN is autodoped to $\sim$ 10^{20} when grown on GaN. This leads to significant broadening of the XPS spectra, and difficulties in determining core-level and valence band maximum positions.

Although GaN has been extensively studied for applications in both light emitting and high power devices, the AlN/GaN valence band offset remains an area of contention. Values quoted in the literature range from 0.8 eV [22] to 1.36eV [23]. This

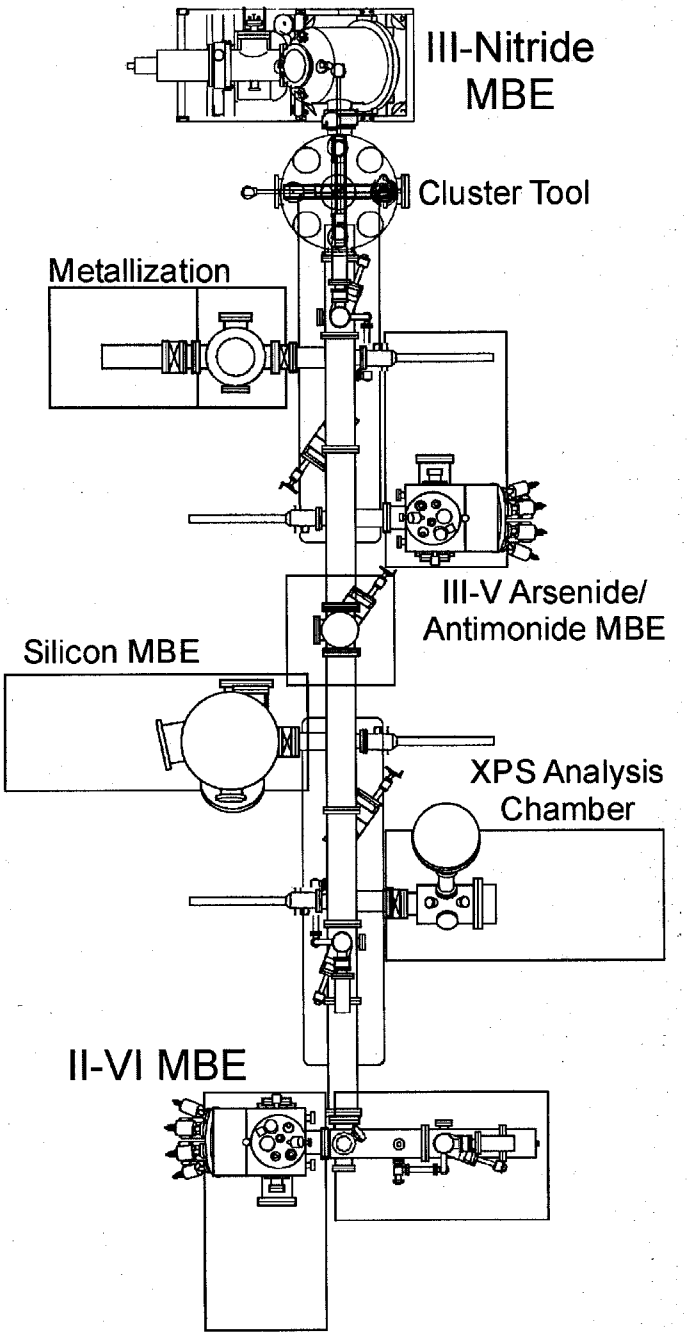

Figure 4.6: A schematic of the growth and analysis system employed for nitride studies.

chapter includes an investigation of the AlN/$Al_XGa_{1-X}N$ band offset as a function of alloy composition. Samples were grown using radio frequency plasma assisted molecular beam epitaxy and characterized with x-ray photoelectron spectroscopy (XPS). Core-level and valence-band XPS data for AlN (0001) and $Al_XGa_{1-X}N$ (0001) samples were analyzed to determine core-level to valence band maximum (VBM) energy differences. In addition, oxygen contamination effects were tracked in an effort to improve accuracy. Energy separations of core levels were obtained from AlN/$Al_XGa_{1-X}N$(0001) heterojunctions. From this and the core-level to valence band maximum separations of the bulk materials, valence band offsets were calculated.

4.3.2 Sample Preparation and Data Collection

Aluminum gallium nitride was grown by molecular beam epitaxy (MBE) on c-plane sapphire substrates employing a low temperature (650 °C) AlN buffer layer. The substrate temperature was held at 800 °C during growth under slightly metal-rich conditions. The growth rate was 0.35 μm/h and the final film thickness was nominally 1 μm. All interfaces were epitaxial and samples were single crystal as confirmed by reflection high energy electron diffraction. The samples were then transferred through a UHV transfer tube to the XPS chamber. High-resolution data in the core level to valence band maximum energy range were taken in 12-hour increments followed by 30-minute survey spectra taken over the O1s through Ga3d energy range. The former were taken to measure the core level to valence band maximum separations. The latter were taken to track the oxygen adsorption on the sample surface. The samples were then returned to the MBE chamber and exposed to nitrogen plasma to remove any oxygen contamination. Figure 4.7 shows two XPS spectra illustrating the removal of oxygen by nitrogen plasma exposure. The change in adsorbed oxygen can be seen by comparing the O1s peak, located at -531 eV, in the pre exposure spectrum to the O1s peak in the post exposure spectrum. By comparing sensitivity adjusted electron flux from the O1s peak relative to Ga3d core level peak, the contribution to the net XPS spectrum from the adsorbed oxygen on the surface was estimated at ~6%

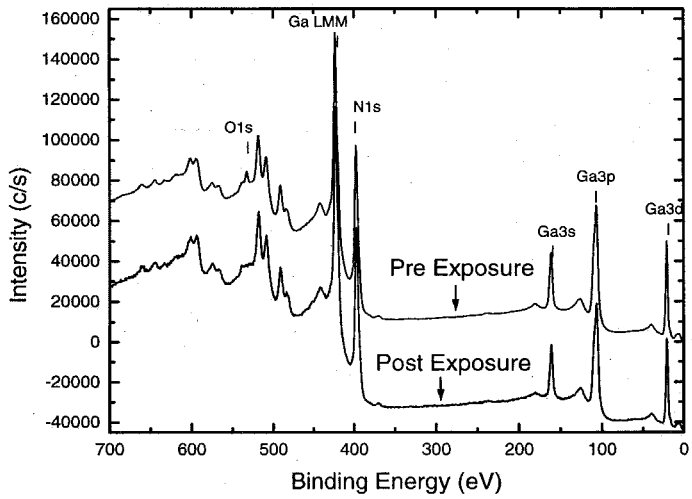

Figure 4.7: XPS survey spectrum of GaN sample before and after exposure to nitrogen plasma showing decrease in O1s peak.

before exposure. After a fifteen minute exposure to nitrogen plasma the O1s peak was undetectable ($< 0.5\%$). A thin layer ($\sim$25 Å) of AlN was then grown on top of the AlGaN. The thickness of the AlN cover layer fulfilled two requirements. First, it was thick enough to relax strain due to the AlN/AlGaN lattice mismatch. Second, it was thin enough to allow significant electron flux from the underlying AlGaN layer to escape the cover layer without scattering. Measurements of the core level separations were then made. Figure 4.5 a-c show the XPS data required to measure the valence band offset in AlN/AlGaN heterojunctions.

4.3.3 Analysis

Core level peak positions (E_{Ga3d}^{AlGaN},E_{Al2p}^{AlN}) were determined by fitting a linear combination of Gaussian and Lorentzian peak shapes to core peak data. Valence band maximum positions (E_v^{AlGaN},E_v^{AlN})were determined by convolving a theoretical valence band density of states (TVBDOS) with a predetermined instrument response function, and fitting to the leading edge of the valence band data. Convolving the TVBDOS with an instrumental response function simulates the finite resolution of the hemispherical energy analyzer used to measure electron flux. The instrument

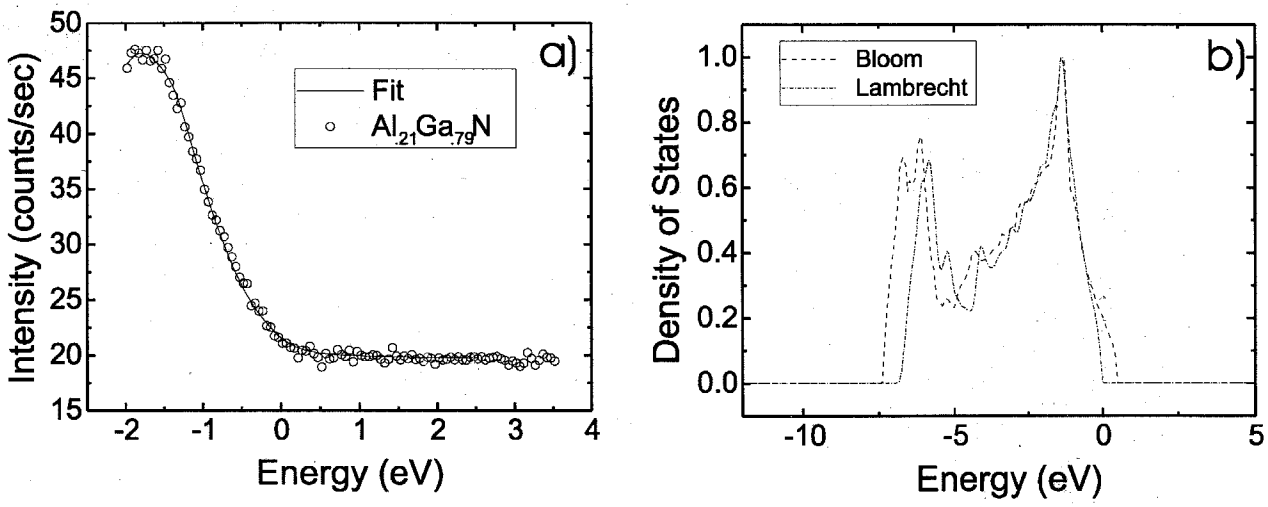

Figure 4.8: a) Broadened theoretical valence band density of states fit to the leading edge of AlGaN valence band XPS data. 0 eV is the valence band maximum. b)Comparison of theoretical valence band densities of states.

resolution function was approximated by a linear combination of a Lorentzian and Gaussian. The known lifetime broadened Au4f lines were convolved with the trial response function. Then the FWHM and percent Gaussian of the response function were determined by fitting to data from background subtracted 4f lines of a gold calibration sample. The x-ray cross section for electrons in the valence band varies in an unknown fashion. Therefore the sensitivity of XPS to electrons is not constant over the entire valence band. To reduce the uncertainties associated with the unknown crossections, the data was fit over a limited energy range near the valence band maximum. The fitting was made over an interval that began 2 eV above the VBM to a position E_{fit} below the VBM. E_{fit} was varied to determine the best value for E_v^{AlGaN}. Figure 4.8a shows an example of a fit to an AlGaN valence band edge.

The core level to valence band maximum separation, $(E_{Ga3d}^{AlGaN} - E_v^{AlGaN}) and (E_{Al2p}^{AlN} - E_v^{AlN})$, was plotted versus E_{fit}. The variation in core level to valence band edge separation over E_{fit} is an indication of fit quality and separation accuracy. During fitting, the GaN theoretical valence band density of states was allowed to vary between that of Bloom *et al* [24] and Lambrecht and Segall.[25] As seen in figure 4.8b, these two densities of states differ in their leading edge shape. This extra degree of freedom allowed accurate fitting to the valence band edge slope. The valence band maximum

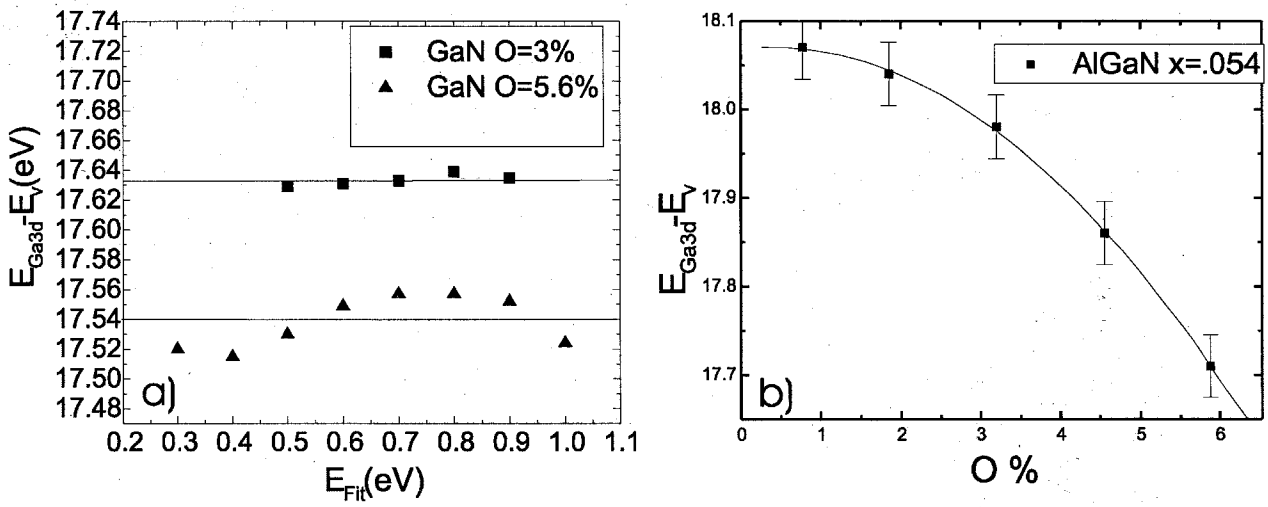

Figure 4.9: a) Core level to valence band max separation as a function of end point E_{fit} in fitting interval. b) Separation as a function of oxygen contamination on sample surface.

positions of both DOS were aligned. (NOT as in the figure, where the first peak positions have been aligned to show the difference in leading edge shape.) The position and composition of the density of states was then fit to the GaN data. In the AlN analysis, an AlN DOS was used as the TVBDOS. For AlGaN, a linear combination of GaN and AlN DOS was used as the theoretical density of states for fitting purposes. In the AlGaN analysis, however, the valence band maximums were not aligned. Their positions were varied to fit the data. Figure 4.9a is the core level to VBM separation for two levels of oxygen contamination on a GaN sample as a function of E_{fit}. It was found that separations were highly dependent on oxygen content. The valence bands' low luminosity requires long acquisition times. The time spent taking each spectrum (typically 12-hrs.) results in a steady build up of oxygen contamination on the sample surface. We observed a corresponding decrease in core level to VBM separation as well as a steepening of the valence band maximum leading edge. To address these changes, separations where measured several times as the oxygen content increased. Figure 4.9b is a plot of core level to VBM separation as a function of oxygen content. Extrapolating back to 0 oxygen % then results in the most accurate core level to valence band maximum separation for the pure material.

Table 1 lists all the relevant binding energy separations measured using the above

x	0	0.054	0.21
offset	1.11 ± 0.2eV	0.95 ± 0.2eV	0.65 ± 0.2eV
$E^{AlN}_{Al2p} - E^{AlN}_{v}$	70.80 ± 0.1eV	70.80 ± 0.1eV	70.80 ± 0.1eV
$E^{AlGaN}_{Al2p} - E^{AlGaN}_{v}$	17.66 ± 0.05eV	18.07 ± 0.1eV	17.78 ± 0.1eV
$E^{AlN}_{Al2p} - E^{AlGaN}_{Ga3d}$	54.25 ± 0.1eV	53.68 ± 0.1eV	53.67 ± 0.1eV

Table 4.1: $AlN/Al_XGa_{1-X}N$ band offsets.

analysis. In addition it gives the corresponding valence band offsets for the compositions we studied. Figure 4.10 is a graph of the valence band offsets for $AlN/Al_XGa_{1-X}N$ versus X. Fitting the offset by $E_v = p1 - 1.11(X-0.5) + p2(X-0.5)^2$ results in a bowing parameter $p2$ of .59 eV. Our value of $1.11 \pm .1$ eV for the AlN/GaN valence band offset is in disagreement with the value of 0.8 ± 0.1eV given in Ref.[22] As previously noted, figure 4.8b shows the significant variance in theoretical valence band density of states. The separation in position of valence band maximum after aligning the leading peak is 0.5 eV. This type of variation in TVBDOS could account for the large difference in the GaN core level to VBM separation reported in Ref.[22] compared to the present XPS measurement.

4.4 Oxidation of GaN

4.4.1 Introduction

Wide band gap semiconductors have attracted considerable attention for applications ranging from lasers to high power electronics. In the last few years, substantial improvement in the structural and electronic properties of GaN has been achieved. This has resulted in major advances in blue-green light-emitting diodes and lasers as well as HFET power devices. The performance of these devices, however, is still limited by a number of materials problems as well as difficulties in producing low resistance contacts. This is particularly true of p-type GaN where extremely high doping densities are required to produce p-type material. Reasonably good ohmic contacts to n-GaN have been found, and the interface chemistry of these contacts

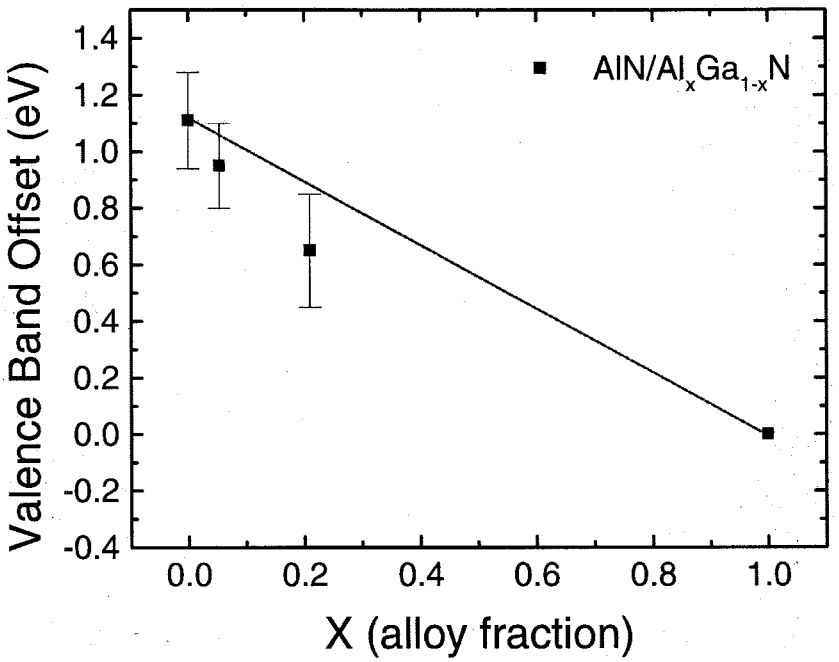

Figure 4.10: AlN/AlGaN band offsets as a function of alloy composition.

investigated. [26] The effects of adsorbates on Fermi-level pinning and Schottky barrier heights, however, is not well understood. A study of the (1x1) GaN surface has shown an increase in electron affinity of ~0.58 eV due to oxygen chemisorption. [27] These types of surface effects have strong implications for device fabrication. We report here a study of the (3x3) reconstructed surface of GaN(0001) including effects due to oxidation.

4.4.2 Experiment

GaN was grown on sapphire (0001) substrates by RF assisted molecular beam epitaxy using a low temperature GaN buffer layer. The substrate temperature was held at 800 °C during growth under slightly metal-rich conditions. The surface morphology and reconstruction were characterized by reflection high energy electron diffraction (RHEED). The RHEED pattern was streaky during growth, and showed a clear (3x3) reconstruction after cool down. The (3x3) reconstruction has been determined to correspond to N-polar GaN. [28] This was confirmed after data acquisition ex-situ by etching in molten KOH. [29] After growth, the samples were moved under vacuum to an XPS chamber via a UHV transfer tube. Data was then taken over 4 regions of interest: the Ga3d core level, N1s core level, O1s core level, and the valence band region. Data acquisition was alternated with in-place exposure to O_2 at room temperature via a leak valve. The sample is in line of sight of a hot filament and the oxygen can therefore be considered excited. Oxygen exposure was measured by monitoring system pressure, and is given in Langmuirs (L), were 1L=10^{-6}Torr s.

4.4.3 Analysis

Several trends were detected in the XPS spectra during oxidation of the (3x3) surface. It was found that the (3x3) reconstruction of the GaN surface results in a second peak on the lower binding energy side of the bulk Ga3d peak in GaN (Fig.4.11a). The shift to lower binding energy is characteristic of metallic bonding between Ga atoms. This implies that the reconstruction corresponds to a fractional Ga adlayer atop a Ga

terminated GaN surface. This is in agreement with a previous in-situ STM study of GaN reconstructions. [28] The Ga3d spectrum was fit to determine the relaxed Ga coverage of the surface. Figure 4.11a shows the results of a fit employing three peaks, one for each state of Ga, and one for the N2s state that lies at ~17 eV. Each Ga peak was fit by two identical spin-orbit split doublets consisting of the sum of a Lorentzian and Gaussian. The splitting was held at 0.46 eV and the branching ratio was set at 0.66. A Gaussian was used for the N2s peak. From this fit, the ratio of the bulk to metallic Ga3d peak areas was found to be 4.35±0.2. For calculating the surface coverage, we begin by assuming the measured intensity from a given core level of a single layer of atoms m monolayers below the surface (I_m) can be described by,

$$I_m = \sigma I e^{\frac{-m}{\lambda(E)Cos(\alpha)}} \tag{4.4}$$

where σ is the sensitivity factor for the given material and core level,[30] and I is an instrumental scale factor depending on primary beam current, detection efficiency, etc. The inelastic mean free path (IMFP) for electrons with energy E, is denoted by λ(E), and is expressed in atomic layers. The collection angle measured from the surface normal (α) was set at 45^o for this study. We designate $I_o^{Ga3d}=\sigma_{Ga3d}I$ as the measured Ga3d peak intensity of a single monolayer of Ga on the surface. The measured intensities of the relaxed surface Ga3d and bulk Ga3d peaks can then be expressed by;

$$I_s^{Ga3d} = \chi I_o^{Ga3d} \tag{4.5}$$

$$I_B^{Ga3d} = I_o^{Ga3d}(\sum_m e^{\frac{-m}{\lambda(E)Cos\alpha}} - \chi) \tag{4.6}$$

Here, c is the fractional surface coverage of relaxed Ga. By taking the ratio of these intensities, and solving for c, an expression for the fraction of relaxed surface Ga can be obtained.

$$\chi = \frac{\beta}{1+\beta}\sum_m e^{\frac{-m}{\lambda(E)Cos\alpha}} \tag{4.7}$$

In equation 4.7, β is the ratio of surface to bulk peak intensities (1/4.35 in our measurements). Although the IMFP for GaN has not been measured, an estimate

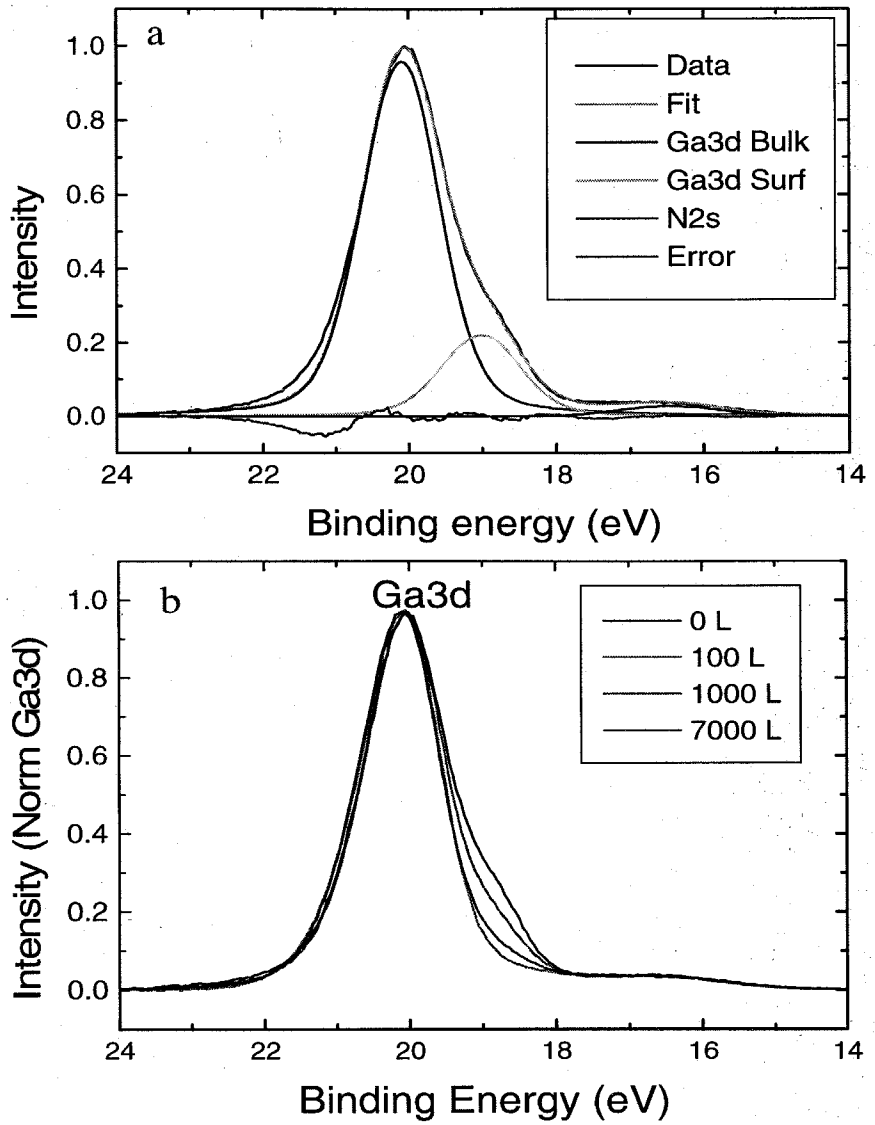

Figure 4.11: X-ray Photoelectron Spectroscopy data showing a)the energy shift associated with surface relaxation of the GaN(3x3) reconstruction, b) graph showing the reduction in relaxed Ga peak with Oxidation.

was obtained from a compilation of previous IMFP measurements. [31] We have used a value of 8.0 atomic layers for the IMFP for 1467eV electrons from the Ga3d region. This corresponds to a surface coverage of 1.15±0.2 monolayers.

Although there is some uncertainty introduced by the lack of measured IMFP for GaN, it appears safe to conclude that the surface consists of ~1 monolayer of relaxed Ga. The (3x3) reconstruction has been found to consist of Ga adatoms positioned in three fold coordinated sites above a Ga termination layer by imaging the reconstruction using STM. Although Ga droplet formation cannot be conclusively ruled out, our data indicates that the entire Ga termination layer is relaxed by the addition of this 0.11 monolayers of Ga adatoms.

The Ga3d metallic peak intensity decreases with oxygen adsorption indicating bonding between the Ga and oxygen. The valence band density of states (VBDOS) spectrum has the shape and position of the bulk GaN VBDOS with an additional component extending to 0 eV (Fig.4.12). The VBDOS metallic component also decreases in intensity as the sample is exposed to O_2. This component is therefore associated with the metallic nature of the reconstructed surface. Using a linear extrapolation to estimate the position of the GaN valence band and the half height position of the metallic Fermi edge (E_F) results in EF-VBM =2.1±0.2eV. This is in agreement with an oxygen adsorption study of the (1x1) surface by Bermudez [27] in which they measured E_F-VBM = 2.4 0.2 eV.

The O1s/Ga3d peak area ratio was measured as a function of oxygen exposure. The O1s peak position is seen to shift to higher binding energy relative to the GaLMM peak as oxygen exposure increases.(Fig.4.13a) This may indicate two states closely spaced in energy for oxygen adsorption. The two states may be due to the difference between binding to the Ga termination layer versus binding to the Ga adlayer. The oxidation was found to terminate with an O1s to Ga3d peak area ratio of 0.43±0.1, corresponding to an oxygen surface coverage of 1.3±0.2 monolayers. This is much too high for simple adatom binding, therefore the Ga termination layer must participate in the oxidation.

The O1s peak was fit by a Gaussian and was found to have a FWHM of 2.0±0.1

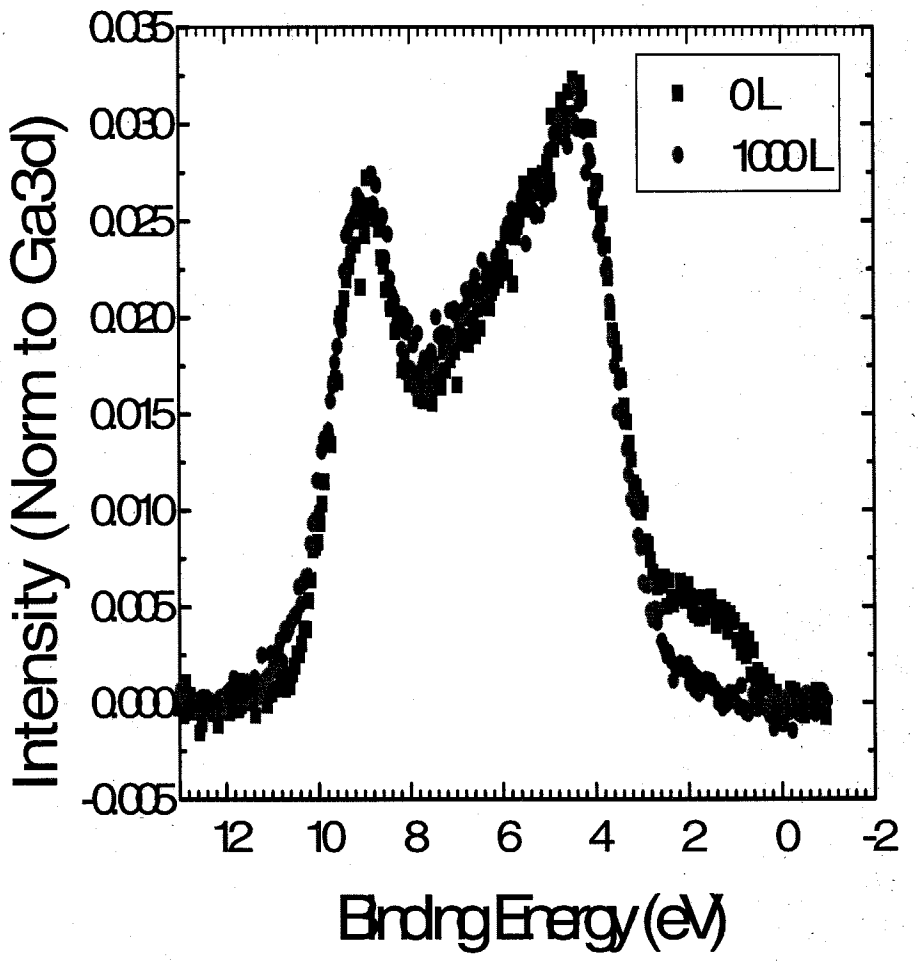

Figure 4.12: X-ray Photoelectron Spectroscopy data showing the metallic ledge extending from the valence band to Fermi level associated with surface relaxation of the GaN(3x3) reconstruction.

eV before deconvolution of the instrumental broadening. This is significantly smaller than the 3.2 eV FWHM measured in [27] for the oxygen adsorption onto (1x1) GaN surfaces. For comparison, figure 4.13b shows the O1s peaks that result from Oxidation of a GaN(1x1) reconstruction. Two distinct peaks are observed. This may explain the larger width of the O1s peak observed by Bermudez. Water adsorbed on the surface has been considered but rejected as a candidate for these extra peaks. This is based on the fact that samples left in vacuum to oxidized do not show a consistently different ratio of O1s peaks than samples oxidized via introduction of O_2 gas. We have tentatively assigned these peaks to binding on N polar and Ga polar surfaces.

4.5 Chapter summary

In summary, AlN/$Al_XGa_{1-X}N$ band offsets have been measured by using X-ray photoelectron spectroscopy. A valence band offset of 1.11±0.1 eV is reported for AlN/GaN. The alloy dependence of the band offset has also been investigated. A preliminary positive valued bowing parameter of .59 eV was found.

We have also studied the (3x3) reconstruction of MBE grown GaN using X-ray photoelectron spectroscopy. We have characterized surface binding energy changes, and investigated the surface reaction with oxygen exposure. We have found a Ga3d surface binding energy change of 1.1±0.1 eV and a metallic Ga adlayer Fermi-level to bulk valence band maximum separation of 2.1±0.2 eV. We have observed the removal of surface relaxation by oxygen exposure and interpreted this as bonding of the surface Ga termination layer and adlayer with oxygen. The width of the O1s peak was found to be smaller for the (3x3) surface than that previously measured for the (1x1) surface.

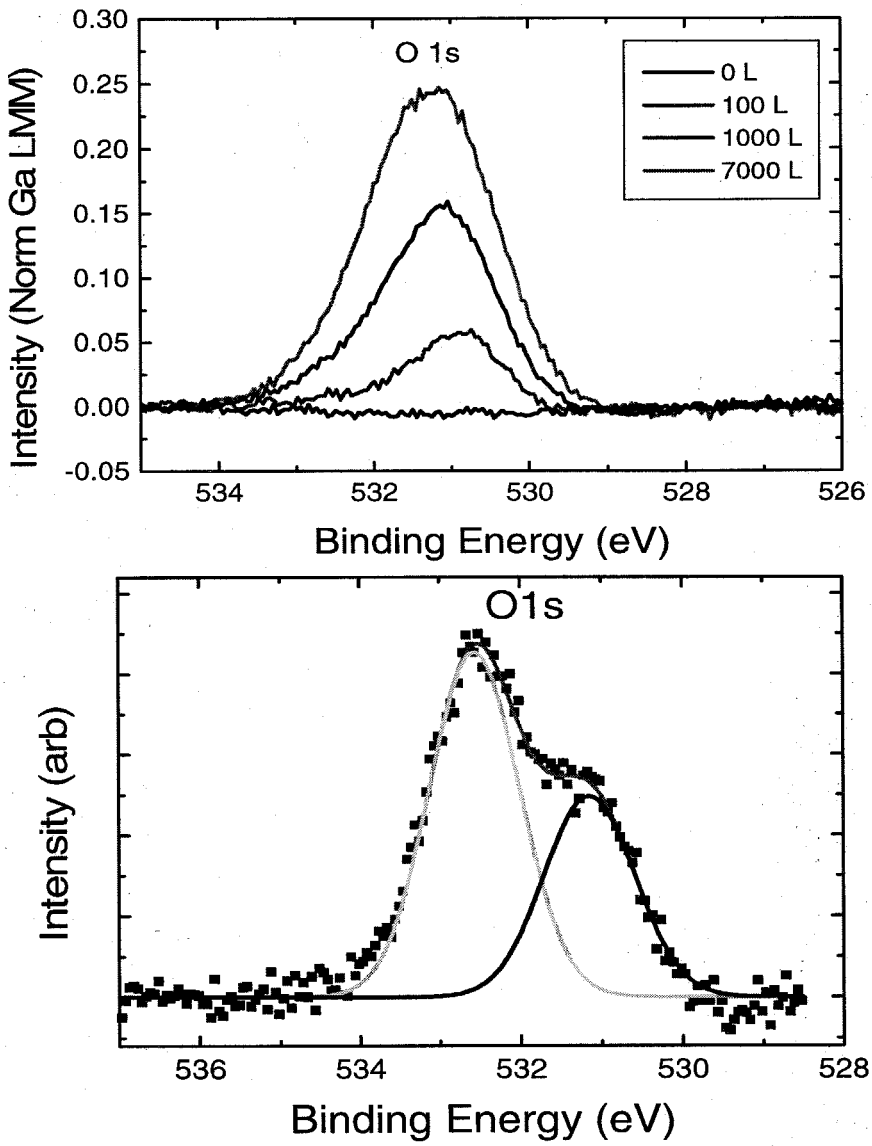

Figure 4.13: X-ray Photoelectron Spectroscopy data showing a)the growth of the O1s peak during Oxidation and its shift toward higher binding energy, b) graph showing two oxygen peaks associated with the (1x1) surface.

Bibliography

[1] K. Siegbahn, C. Nordling, A. Fahlman, R. Nordberg, K. Hamrin, and J. Hedman, *ESCA: atomic, molecular, and solid-state structure studied by means of electron spectroscopy* (Almqvist and Wiksells, Stockholm, 1967).

[2] K. Kroemer, Surf. Sci **132**, 543 (1983).

[3] G. Duggan, J. Vac. Sci. Technol. B**3**, 1224 (1985).

[4] E. Kraut, R. Grant, J. Waldrop, and S. Kowalczyk, Phys. Rev. Lett. **4**, 1620 (1980).

[5] E. Kraut, R. Grant, J. Waldrop, and S. Kowalczyk, Phys. Rev. B **28**, 1965 (1983).

[6] E. Yu, E. Croke, T. McGill, and R. Miles, Appl. Phys. Lett.**56**, 569 (1990).

[7] E. Yu, E. Croke, D. Chow, D. Collins, M. Phillips, T. McGill, J. McCaldin, and R. Miles, J. Vac. Sci. Technol. B**8**, 908 (1990).

[8] R. Grant, J. Waldrop, and E. Kraut, J. Vac. Sci. Technol.**15**, 1451 (1978).

[9] J. Waldrop, E. Kraut, S. Kowalczyk, and R. Grant, Surf. Sci. **132**, 513 (1983).

[10] J. Waldrop, S. Kowalczyk, R. Grant, E. Kraut, and D. Miller, J. Vac. Sci. Technol.**19**, 573 (1981).

[11] J. Waldrop, R. Grant, and E. Kraut, J. Vac. Sci. Technol. B**5**, 1209 (1987).

[12] S. Kowalczyk, W. Schaffer, E. Kraut, and R. Grant, J. Vac. Sci. Technol.**20**, 705 (1982).

[13] S. Kowalczyk, E. Kraut, J. Waldrop, and R. Grant, J. Vac. Sci. Technol.**21**, 482 (1982).

[14] F. Xu, M. Vos, J. Sullivan, L. Atanasoska, S. Anderson, J. Weaver, and H. Cheng, Phys. Rev. B **38**, 7832 (1988).

[15] G. Gualtieri, G. Schwartz, R. Ruzzo, R. Malik, and J. Walker, J. Appl. Phys.**61**, 5337 (1987).

[16] G. Gualtieri, G. Schwartz, R. Ruzzo, and W. Sunder, Appl. Phys. Lett.**49**, 1037 (1986).

[17] S. Kowalczyk, J. Cheung, E. Kraut, and R. Grant, Phys. Rev. Lett. **56**, 1605 (1986).

[18] T. Tuc, C. Hsu, and J. Faurie, Phys. Rev. Lett. **58**, 1127 (1987).

[19] G. Barraf, J. Applbaum, and D. Hamann, Phys. Rev. Lett. **38**, 237 (1977).

[20] C. Van de Walle and R. Martin, Phys. Rev. B **34**, 5621 (1986).

[21] C. Van de Walle and R. Martin, Phys. Rev. B **35**, 8154 (1987).

[22] G. Martin, S. Strite, A. Agarwal, A. Rockett, H. Markoc, W. Lambrecht, and B. Segall, Appl. Phys. Lett.**65**, 610 (1994).

[23] J. Waldrop and R. Grant, Appl. Phys. Lett.**68**, 2879 (1996).

[24] S. Bloom, G. Harbeke, E. Meier, and I. B. Ortenburger, Status Solidi B **66**, 161 (1974).

[25] W. Lambrecht and B. Segall, Phys. Rev. B **50**, 14155 (1994).

[26] C. Wu and A. Kahn, J. Vac. Sci. Technol. B**16**, 2218 (1998).

[27] V. Bermudez, J. Appl. Phys.**80**, 1190 (1996).

[28] A. Smith, R. Feenstra, D. Greve, J. Neugebauer, and J. Northrup, Phys. Rev. Lett.**79**, 3934 (1997).

[29] M. Seelmann-Eggebert, J. Weyher, H. Obloh, H. Zimmermann, A. Rar, and S. Porowski, Appl. Phys. Lett.**71**, 2635 (1997).

[30] P. E. inc., *Multipak Operator's Manual* (Physical Electronics, Flying Cloud, Mn, 1996).

[31] M. Seah and W. Dench, Surf. Int. Anal. **1**, 2 (1979).

Part II

Devices

Chapter 5 Characterization of Nitride Based Devices

Research into nitride based devices has primarily focused on optical applications such as short wavelength LEDs and laser diodes (LDs). Recent successes in producing high power HFETs has led to the realization that nitride materials may also play important roles in high power and high frequency applications. This is primarily due to the large breakdown fields and high saturation velocities of the nitrides. HRL has recently reported on the electrical characteristics of HFETs grown and fabricated at their facility in Malibu. They report a high-efficiency 20 watt GaN power amplifier, which is the highest continuous wave power level and efficiency ever reported for the technology. GaN HFETs are expected to perform in the 10-100 GHz range. This makes nitride materials ideal for microwave switching as well as emitters for cellular phone applications. In addition, AlGaN/GaN HFETs have shown the capability to switch high voltages, above 100V. [1] This may make GaN devices ideal for analog front ends in analog to digital converters. Optoelectronic devices such as LEDs, UV detectors, and laser diodes are currently being fabricated and marketed, and heterojunction field effect transistors are well on their way to commercialization. This insures that the trend toward higher quality material and better processing technology will continue.

An obvious application of GaN's high critical fields that has yet to be investigated with significant success is high power switching for the power industry. High critical fields allow thinner devices and higher doping for the same standoff voltage. This leads to lower on state voltage drop, less wasted power, and lower cooling requirements. Figure 5.1 shows the theoretical, estimated, and measured value of the critical field of a number of semiconductor materials. As can be seen in the figure, the critical field of GaN is approximately an order of magnitude larger than Si, and comparable to

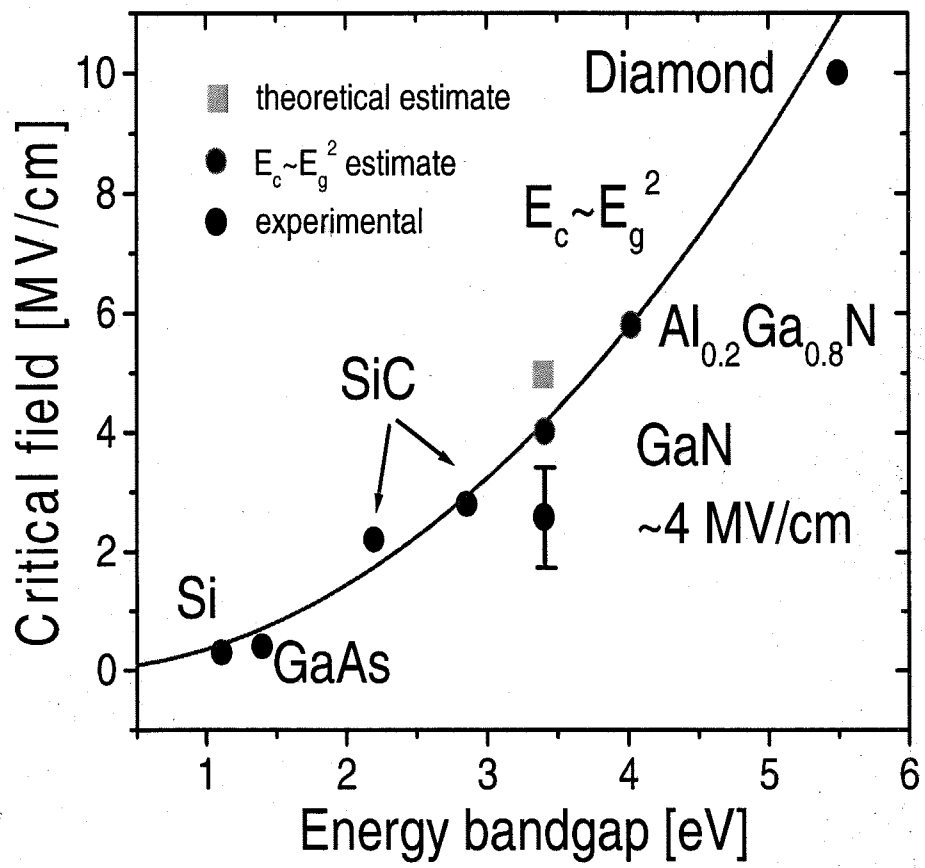

Figure 5.1: The critical fields for a number of semiconducting materials vs. their band gap.

or possibly larger than SiC. AlGaN ternary compounds may also have a significantly increased critical field if the E_g^2 dependence of critical field holds true. Along these lines, we have previously fabricated and characterized a high power Schottky rectifier with 750V reverse breakdown, as well as a 450V GaN pn diode. The next step is therefore production of a switch. We investigated GaN npnp thyristors since the thyristor is a commonly used device for high power switching in the power industry. The next section reviews the fabrication and characterization of these devices.

5.1 GaN Thyristors.

Thyristors are a family of devices that show bi-stable current voltage characteristics. Their general structure consists of p-n-p-n layers of varying doping with a number of contacts ranging from 2 to 4. If contacts are made to only the two outermost layers, the device is commonly called a Schockley diode. If, in addition, a contact is made to one of the inner layers to serve as a base electrode, similar to an npn transistor, the device is called a semiconductor controlled rectifier (SCR), or thyristor. The outer layers are heavily doped to facilitate ohmic contact formation and charge injection in on state operation. One of the inner layers is lowly doped to serve as the voltage stand off region, and the other inner layer is moderately doped to serve as the base region. Figure 5.2 shows a schematic of a thyristor and its corresponding current voltage characteristics. In the IV diagram are labeled V_{BR}, V_{BF}, and V_{ON}. These correspond to the reverse biased breakdown voltage, forward biased breakover voltage, and the on state voltage. In the thyristor schematic are labeled the anode, cathode, and base contacts as well as junctions J_1, J_2, and J_3. Two basic factors limit the reverse breakdown and forward breakover voltages of this structure: avalanche breakdown, and punch-through. In reverse bias, the anode is negatively biased relative to the cathode. In this mode, junctions 1 and 3 are reverse biased and junction 2 is forward biased. For our devices, layer n_1 is lowly doped and corresponds to the stand off region. This causes most of the voltage to be dropped across junction 1 in reverse bias. Breakdown occurs when the depletion region caused by the applied voltage either reaches completely across region n_1 and contacts region p_2 (this is termed punch through), or when the field at junction 1 reaches the critical field of the material and causes avalanche breakdown. The punch through voltage for a one-sided abrupt junction is given by;

$$V_{PT} = \frac{qN_{n1}W_{n1}^2}{2\varepsilon_s} \tag{5.1}$$

Avalanche breakdown occurs when the electric field becomes large enough that the carriers gain enough energy between scattering events that when they do scatter,

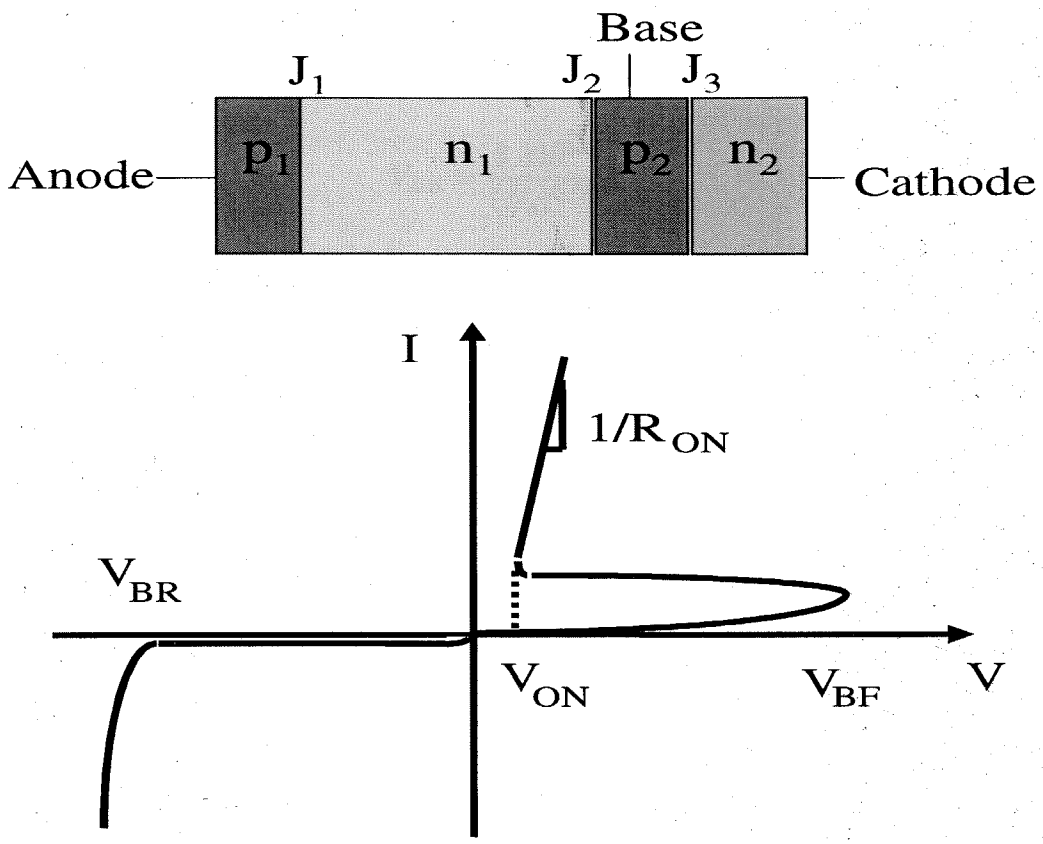

Figure 5.2: a) Schematic diagram of a thyristor structure, b) Current voltage characteristics of a thyristor structure.

they can produce an electron-hole pair that then proceed to repeat the process of generating more carriers. If it is assumed that electrons initiate the ionization process, the condition for avalanche multiplication and break down is given by;

$$\int_0^W \alpha_n exp[-\int_x^W (\alpha_n - \alpha_p)dx']dx = 1 \tag{5.2}$$

By using the calculated ionization coefficients of ref.[2] and assuming $\alpha_n = \alpha_p$, we can solve this numerically. The avalanche breakdown for GaN as a function of doping density, N_d, is given by;

$$V_{BR} = \frac{3.310^{15}}{(N_d)^{0.73}}[V] \tag{5.3}$$

Alternatively, if the critical field for the material is known, the break down voltage is given by;

$$V_{BR} = \frac{\varepsilon_s E_{cr}^2}{2qN_d} \tag{5.4}$$

The thickness of the stand off region of devices presented in this chapter were $\sim 1\,\mu$m. Using a conservative estimate of the critical field of 2.5 MV/cm, the breakdown in these structures should occur via punch through, and for a $1\,\mu$m thick GaN layer doped at $5\text{x}10^{16}/\text{cm}^3$, should occur at ~40V.

Figure 5.3a shows the layer thickness, doping, and contact scheme for the thyristor sample studied. Figure 5.3b shows the on and off state curve trace for this device. These devices showed very strong bi-stability. The on state current was found to be approximately 370 times larger than the off state current at 1.5V. They did not, however, switch into the off state during the downward sweep of voltage. In fact, they showed a persistent on state once switched until thermally or electrically stressed. This was accomplished by applying a high bias to the device followed by a quick ramp down to zero volts. Following this procedure, the device would remain in the off state until the voltage was again raised above the forward break over voltage at which point the device would return to the persistent on state. The switching and subsequent stressing was non destructive, however, and the devices could be cycled repeatedly. As a test, we repeatedly switched one device on and off over one hundred

times.

This effect may be related to the persistent photoconductivity (PPC) observed in both n and p type GaN. PPC has been shown to have characteristic decay times on the order of 10^4s in MOCVD material.[3, 4] A strong temperature dependence of the relaxation time has also been observed with much shorter relaxation times for temperatures above 350 °C.[3] It is believed that this excess conductivity is caused by capture barriers for the ionized acceptors, and fits to the decay of PPC has led to a value of 0.2eV for the barrier height.[4] Some speculate that this barrier is caused by a relaxation of the lattice after ionization. The temperature dependence of the PPC relaxation time would suggest that electrically stressing the device results in heating which in turn shortens the relaxation time enough to allow a return to the off state. Simply allowing the device to sit for extended times resulted in inconsistent results with some devices returning to the off state while others remained on regardless of time. The switching voltage progression of one device is shown in figure 5.4. After the initial switch at ~21V, the device switches on at a very low voltage,~5V. As the device is continually switched on and off, the switching voltage slowly improves to around 10V. Annealing the device at 650 °C for 30s returns the switching voltage to ~20V. Other explanations for this complex electrical behavior may include breakdown induced conductive paths in the bulk, or surface flashover along the mesa walls. The significant amount of reverse biased blocking, however, argues against breakdown induced shorting, and unless the large area contacts are in fact Schottky, surface flash over should not result in the observed IV trace after breakdown. The exact mechanism for this behavior, be it charging of deep levels or breakdown of one type or another, may have significant impact on the viability of bipolar GaN based devices. Section 5.2 discusses electroluminescence and current voltage characterization of GaN pn and pin junctions that sheds some light on the conduction mechanisms involved in GaN devices.

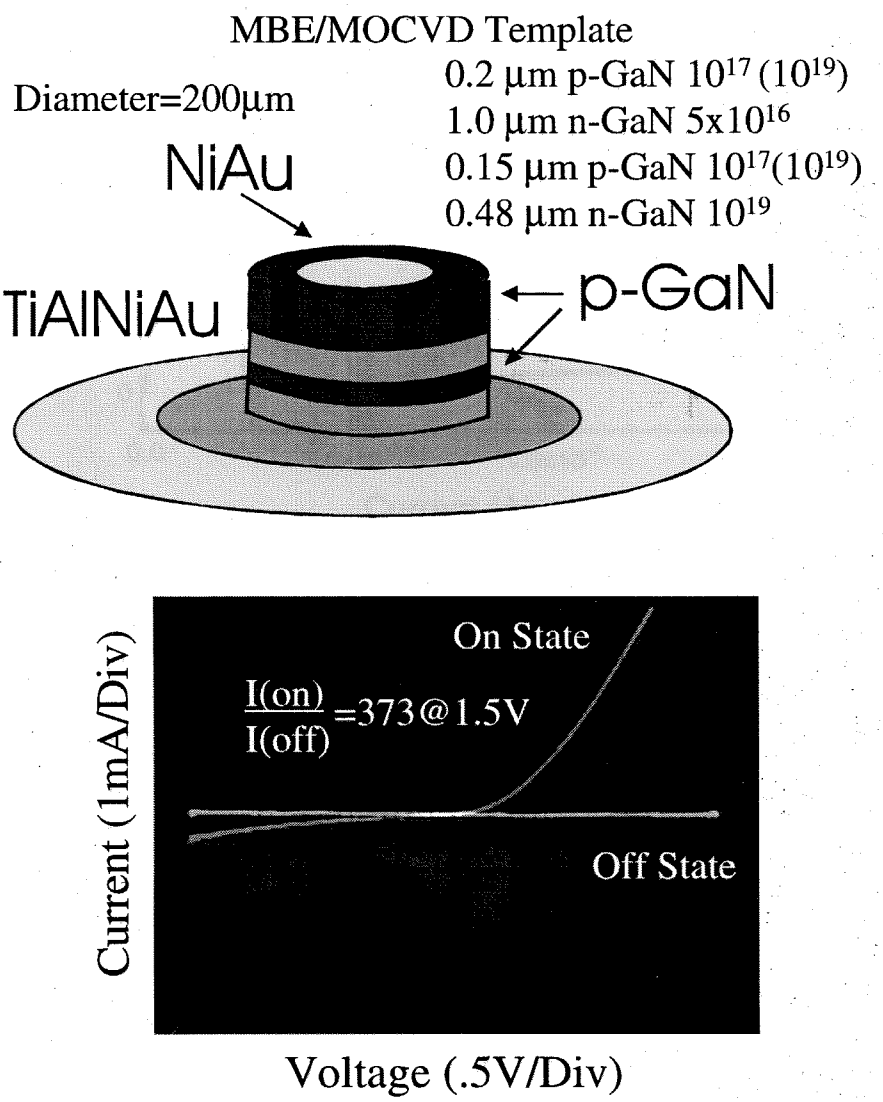

Figure 5.3: a) Schematic of thyristor device. b) Curve traces of the stable on and off states of this device.

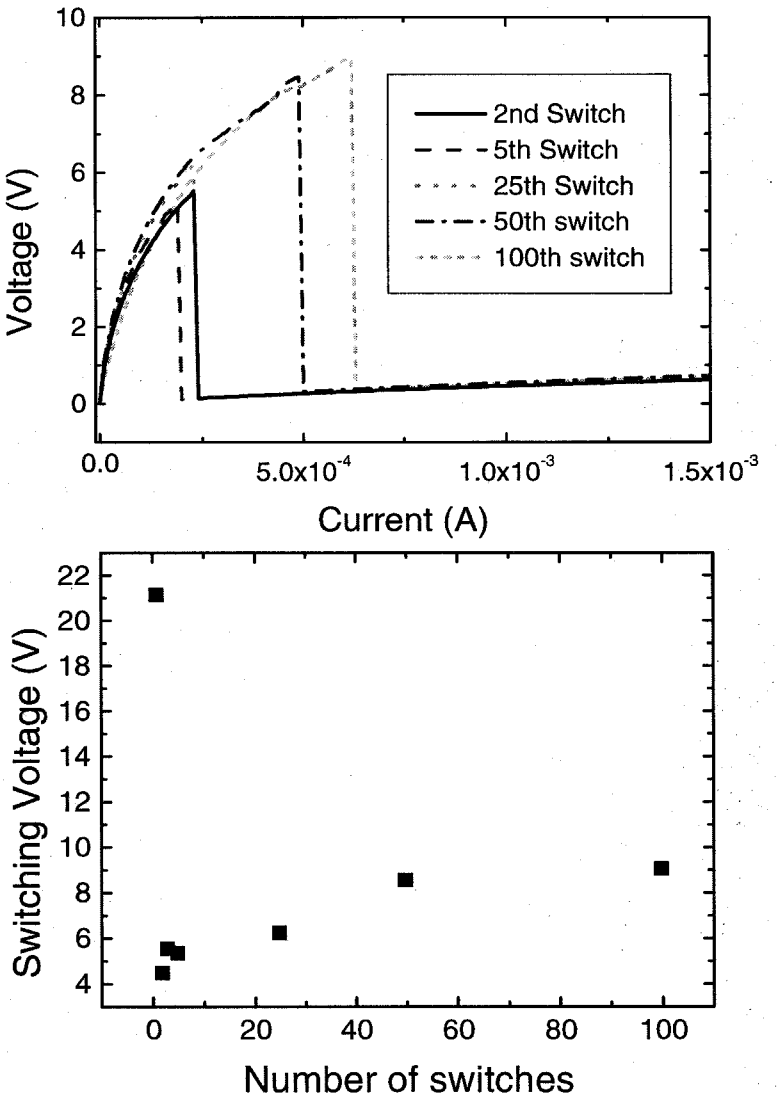

Figure 5.4: a) Current voltage graph of switching progression of GaN Schockley diode. b) Switching voltage of Schockley diode during on-off cycling.

5.2 Electroluminescence Characterization of GaN Bipolar Devices

Doping GaN p-type is difficult for two reasons. First is the large ionization energies associated with all acceptor dopents yet investigated. Second is the intrinsic n-type background doping of GaN. High quality material still possesses an n-type carrier concentration of $\sim 10^{16}/cm^3$. These intrinsic carriers compensate the acceptor levels often resulting in highly resistive material. To overcome these difficulties, doping densities on the order of $10^{20}/cm^3$ of the acceptor impurity, typically Mg or Zn, are required to produce p-type material. These high levels of dopents in conjunction with the high level of defects results in hole mobilities of approximately 10 cm^2/Vs. In addition, the high vapor pressure of Mg hinders incorporation of this dopent in to the growing film at typical GaN growth temperatures. These inherent difficulties combined with the many still unresolved growth issues results in a number of hurdles for producing bipolar nitride devices.

Figure 5.5 contains the IV and EL data taken from a GaN pn diode grown on sapphire by RF-MBE. Although we have not been able to calibrate our p-type doping density reliably due to some of the issues mentioned above, it is believed that this sample is doped in the $10^{19}/cm^3$ range based on the cathodoluminescence data presented in figure 5.6. The device showed considerable leakage current in reverse bias with a gradual and continuous increase in leakage with reverse bias so reverse breakdown voltage could not be determined.

The inset of figure 5.5 shows the forward biased IV curve on a log scale which highlights the unusual turn on characteristics of these devices. It is believed that this early turn on current is associated with a recombination-tunneling mechanism involving a trap state within the band-gap. There are two models that may explain these data. the first involves trap assisted tunneling in which an electron on the n side of the junction may first fall into a trap near the junction and then tunnel into the valence band of the p side. This path has been analyzed by Riben and Feucht

[5]who have shown that the forward current density is given by;

$$J = C_1 N_t e^{BV_j} \tag{5.5}$$

Here, C_1 is a constant, N_t is the trap density and B is a constant given by;

$$B = (8\Pi/3h)(m_h^* \varepsilon_s)^{0.5} N_d / [N_a^{0.5}(N_a + N_d)] \tag{5.6}$$

Fitting the area indicated on the graph results in a value of B of 6.11. With Nd of the n-type material equal to $1x10^{18}/cm^3$, this gives a value of $5x10^{18}/cm^3$ which is approximately what is expected from the growth conditions of this sample. The second model is that this is a standard trap related recombination current but with a high level of trap states resulting in the dominance of recombination within the space charge region. Either of these models, however, indicate a high level of trap states within the material. The same fit as used above leads to a value of 6.35 for the ideality factor (n).

The EL spectrum of this material shows a small amount of blue luminescence as a shoulder on the short wavelength side of the emission spectrum and no band related recombination. It is dominated by the broad "yellow" luminescence (YL) associated with nonideal growth conditions. Some researchers have claimed that the yellow luminescence is related to oxygen doping of the GaN. This is not supported by our observations of YL in samples grown here. Samples grown on the same day would be expected to show similar YL given that the residual oxygen in the chamber is unlikely to change drastically from growth to growth in the same day, yet cathodoluminescence of these samples can vary greatly. More likely, as supported here by the IV data, these recombination's are via deep level states in the gap. We find that growth under nitrogen rich conditions significantly increases the level of yellow luminescence observed in the resulting film. This agrees with the hypothesis that YL is related to Ga vacancies.[6] However, it does not rule out the possibility that defects are responsible given that crystal quality also degrades with nitrogen rich growth conditions.

Figure 5.6 shows the current voltage characteristics of a GaN pin diode. The inset of figure 5.6a shows the forward biased current. The distinct trap related current is not as prevalent as that seen in the previous figure. This may be due to the lower doping in the intrinsic region resulting in lower band bending, and hence, a greater tunneling distance. Alternatively, this may be related to a lower density of trap states, thus suppressing the recombination rate. Consistent with this is the strong electroluminescence peak centered around 435nm of figure 5.7. This "blue band" recombination is a well documented feature of luminescence from Mg doped GaN.[7, 8, 9] This indicates that recombination occurs in the p-type layer. Figure 5.7a shows the luminescence as a function of forward current. No significant shift in peak position was observed as the current was raised within these parameters. This indicates that temperature related narrowing of the band gap is not responsible for the sub bandgap luminescence observed here. Again, the recombination takes place within the p-type layer. This is expected given the low mobility of holes in GaN. In addition, the ratio of the blue band peak height to the YL peak height has a value of 2.1, 3.6, 5.0, and 5.1 for forward currents of 2, 4, 6, and 10 mA respectively. This supports the idea that for low forward biases trap related recombination dominates.

Figure 5.7b compares the forward to reverse bias luminescence of these diodes. These devices leak considerably in reverse bias, as can be seen in the previous I-V graphs. The luminescence data suggests that this leakage current is also associated with the deep levels present in the material. In addition, the dominance of the yellow luminescence in the reverse biased condition indicates that the reverse current is primarily injection of electrons from the p layer into the n layer since recombination in p type material results in blue luminescence. This characterization of pn junctions indicates that improving the material quality of the material is required before we will achieve significant success in growing working thyristors.

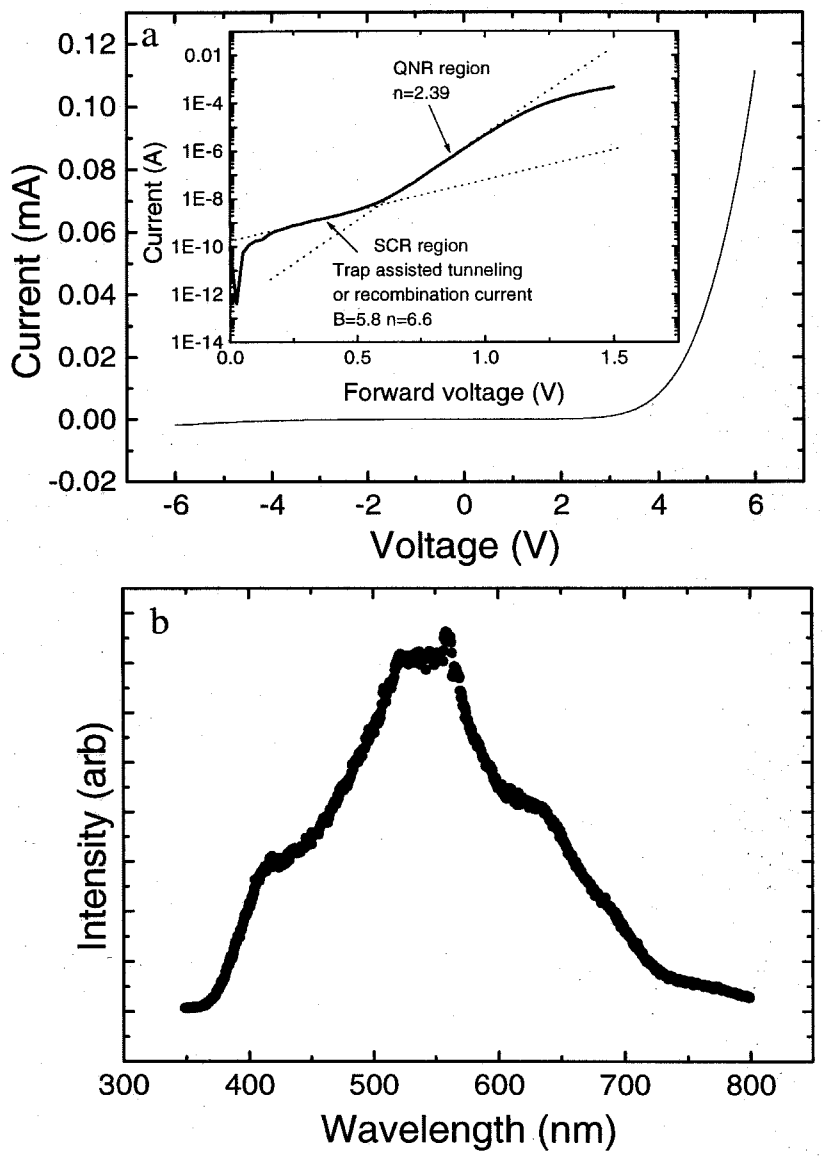

Figure 5.5: Characterization of a GaN pn junction. a) IV curve showing the slow turn on and inset highlighting the trap assisted tunneling current for a forward biased junction. b) EL spectrum of this device showing the broad emission spectrum and low intensity of band gap recombination.

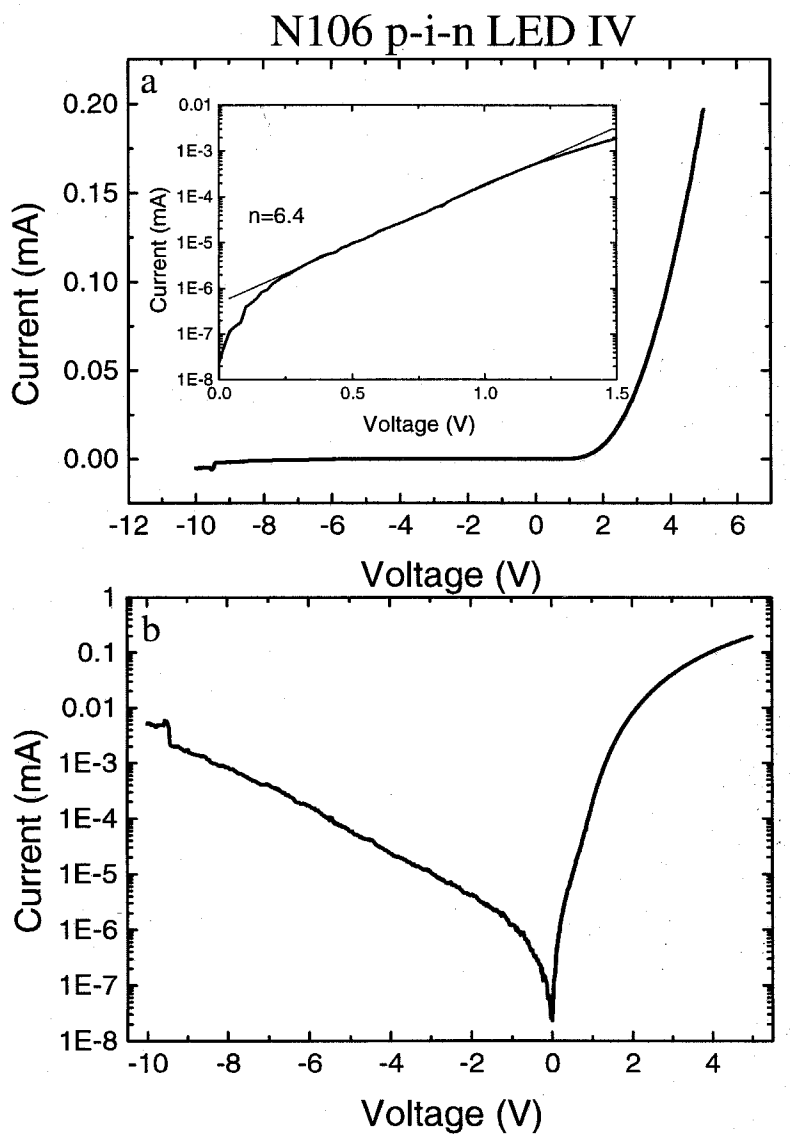

Figure 5.6: Characterization of an GaN pin junction. The IV curves show a) the slow turn on of these devices, and b) their large leakage current in reverse bias.

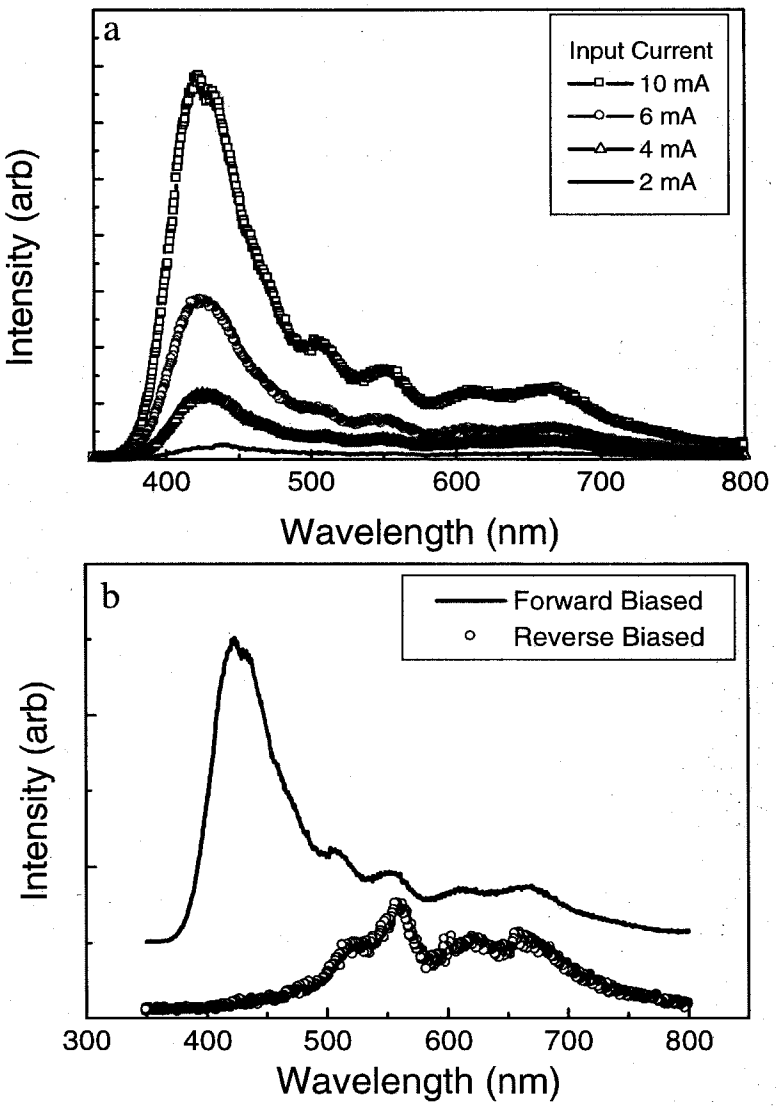

Figure 5.7: Characterization of an GaN pin junction. a) Current dependence of EL. b) Forward and reverse biased EL.

5.3 Chapter Summary and Conclusions

A few nitride based devices were fabricated and characterized via current voltage measurements and electroluminescence. Two terminal GaN thyristors with 1 μm thick standoff layers were fabricated. They showed a number of unusual current voltage behaviors including persistent on states, inconsistent switching voltage, and thermal sensitivity. The maximum breakover voltage observed was 21V. GaN pn and pin diodes were also grown and fabricated. They showed significant leakage current that was shown to be associated with a high level of yellow band luminescence. The pin diode had better luminescent qualities than the pn diode. The peak wavelength of emission from the pin diode was found in the 435nm range consistent with recombination within the p-type layer.

Chapter 6 Photoelectrochemical Etching and GaN MEMs

6.1 Technique Overview

The robust and chemically inert nature of GaN makes processing of this material extremely difficult. No viable wet etch technology has yet been developed that successfully etches GaN at an acceptable rate. Most researchers have therefore resorted to physical ion bombardment of one type or another. These techniques include reactive ion etching (RIE), chemically assisted ion beam etching (CAIBE), or direct ion milling. This type of etching produces significant damage to the surface of the GaN resulting in defect induced changes in the contact behavior. One such effect is the compensation of p-type material by the defects caused by physical etching. This leads to highly resistive contacts and poor device performance.

A nondamaging method of forcing chemical etching of GaN is through the use of photoelectrochemical (PEC) etching. Standard PEC etching of GaN is achieved by exposing it to above bandgap radiation while immersed in an aqueous KOH solution [10]. It is believed that band-bending at the n-GaN/electrolyte interface causes photogenerated holes to be swept toward the surface where they participate in the chemical dissolution of the semiconductor [11]. In p-GaN, the bands bend in the opposite sense, creating a barrier for hole migration to the surface. This results in etch selectivity between dopent types and opens the doors to selective etching of complex structures. Undercutting of p-GaN layers was first observed by Youtsey et.al. [11]. More recently it was studied using backside illumination through the sapphire substrate [12]. The fabrication of complex microstructures in GaN, however, requires that the undercutting be precisely controlled and optimized. For one, etching must be prevented in regions of the n-type underlayer designed to provide mechanical an-

choring for the p-type membrane above. Furthermore, for structures with a large undercut span, the lateral etch rate must be high to achieve a practical total etch time. Figure 6.1 show the general schematic of a PEC etching cell. In addition it contains a schematic representation of the band bending believed to be responsible for the dopent selective behavior of PEC as described above.

In our experiments, p-on-n bi-layer samples were immersed in 0.1 M KOH and exposed from the front side by a Xenon arc lamp with 100 mW/cm^2 in the UV. Prior to the PEC etch, opaque metal masks (Ni/Au $80nm/20nm$) were patterned onto the samples and then annealed at 500°C for 5 minutes in argon to prevent peeling in the corrosive bath. As indicated in the figure, we observed that the n-type epilayer does not etch in the areas immediately below the masks. However, masked regions near the outermost periphery of the overlayer undercut very slowly as a result of stray UV radiation that is reflected back through the sapphire substrate directly into the n-GaN layer. To suppress this reflection, the samples were suspended in solution by a Ni wire epoxied near the side. (We expect this problem can be effectively eliminated by using backside polished substrates with a thin SiO_2 anti-reflection coating.) The Ni wire also served as an electrical contact to the p-GaN overlayer during the PEC etch. It was maintained at a positive 1.5 V bias with respect to a Pt cathode in solution. The application of this bias was seen to dramatically accelerate the undercutting of the unmasked p-GaN areas, with lateral etch rates in excess of $30\mu m$/min being observed for certain geometries. The origins of this marked increase in etch rate are not well understood at this time. However, observations of the undercutting dynamics suggest that the sample bias gives rise to drift currents of the electrolyte within the narrow etched channels under the p-GaN film. We suspect these currents deliver chemically active OH^- radicals to the etch front much more efficiently than diffusion alone.

6.2 Material Effects on Etching

Figure 6.2 shows three selectively etched structures. Figure 6.2a is an MBE grown pn (1 μm p on 1 μm n) diode that has been exposed to the PEC process. Figure 6.2b

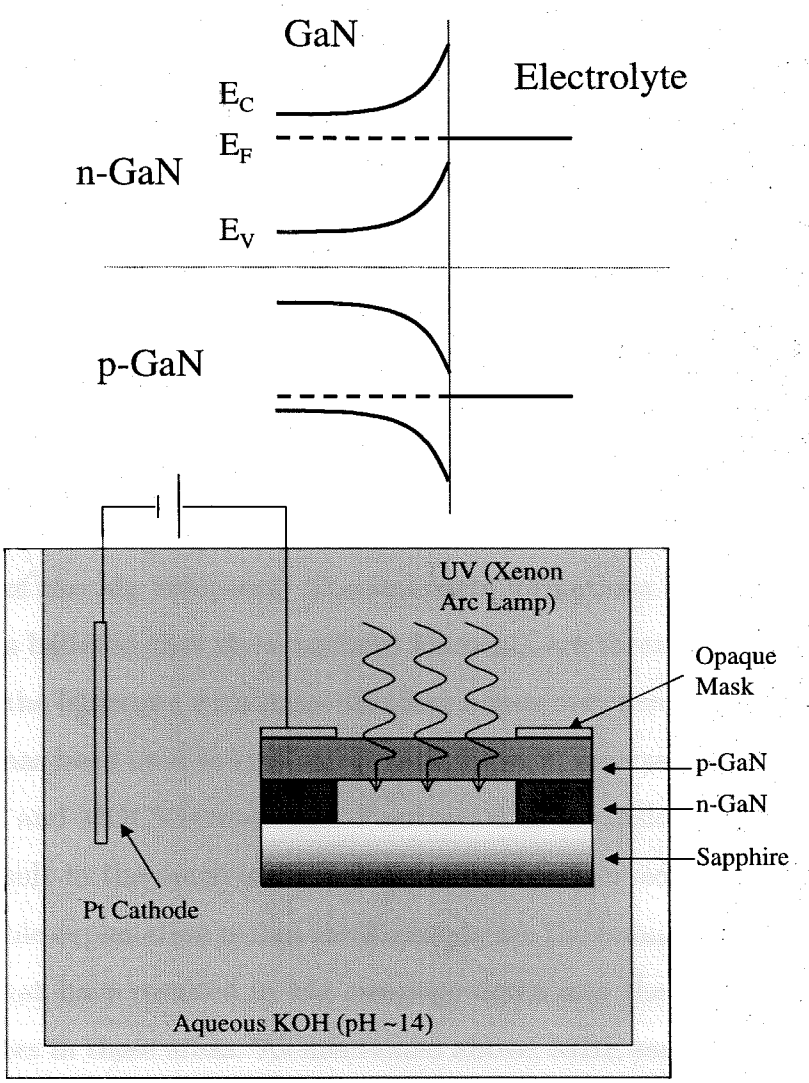

Figure 6.1: a) Schematic diagram of band bending at the interface of p and n GaN and electrolyte. b) Diagram of PEC etch cell.

is an MOCVD sample that has undergone the same process. These structures were formed by first producing mesas using chemically assisted ion beam etching, and then subjecting the sample to the PEC etch. As can be seen in the figures, the n type layer on the bottom was etched rapidly away leaving a suspended overhang. The MOCVD material is found to be less resilient to the etching procedure. The surface that had been etched using CAIBE has deteriorated slightly, and small stalactites consisting of unetched n type material decorate the bottom of the p type layer. The MBE sample, however, showed no deterioration during the etch and no unetched material remains of the n type material. Two mechanisms may be responsible for the differences between the two samples. The first explanation involves the high density of hydrogen present during MOCVD growth. Hydrogen is known to passivate the p-type Mg acceptor by forming Mg-H complexes. Post growth anneals are required to break these complexes and activate the Mg acceptor. The hydrogen, however, is not removed from the sample during this process, and this may result in a slow repassivation of the Mg acceptors. The stalactite formations may also be related to hydrogen. It is believed that these resilient filaments are threading dislocations. The interaction of the hydrogen with these dangling bonds may result in passivation of the surface. This has been used to explain the differences in reverse biased leakage current between MBE and MOCVD materials. Passivation of the dislocations by hydrogen is believed to result in the much lower leakage currents observed in MOCVD material. Another possible explanation is that the filaments are the remnants of open core screw dislocations that have resulted in Mg creepage down into the n type layer resulting in low etch rates in these areas. As mentioned above, MBE samples are very resilient to the etch. Figure 6.2c shows a .55cmx.4cm piece of p-type GaN that has been completely removed from the sapphire substrate.

6.3 MEMs Devices

This etch selectivity opens the door for a whole range of MEMs devices. Several material properties of GaN make it a promising candidate for micro-electromechanical

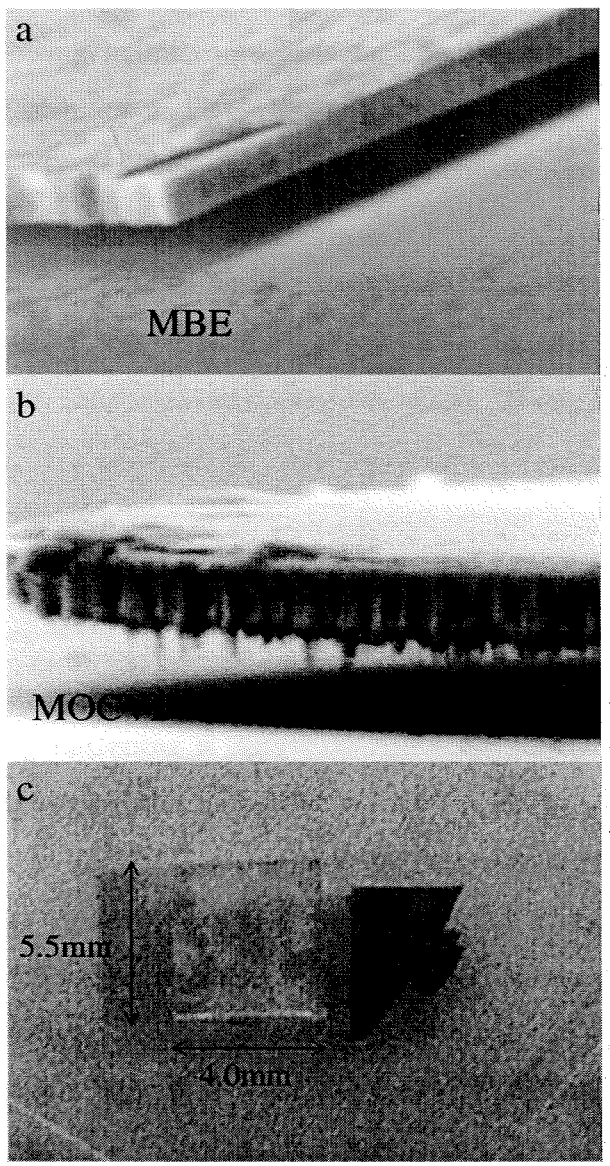

Figure 6.2: SEM micrographs of a) MBE pn sample after etching, b) MOCVD sample after etching showing low resilience and stalactite filaments, c) Optical view of sapphire and broken p layer that was removed.

applications. Among the properties which set it apart from silicon, the conventional choice for MEMS, is its large piezoelectric coefficients. This piezoelectric response would provide a powerful means for the excitation and detection of acoustic waves in micro-resonators. In addition, the strong piezoresistive effect in p-GaN [13] is ideal for electrical strain sensing in micro-positioners. Furthermore, chemical inertness and high temperature stability make GaN a suitable choice for MEMS applications in harsh environments. Transparency to visible wavelengths also allows it to feature in optical micro-switches and waveguides.

One such device that we studied was a piezoresistive cantilever. The $(000\bar{1})$ GaN layers used here were grown by molecular beam epitaxy on c-plane sapphire. Both the n+ (Si) and the p+ (Mg) epilayers are $1\mu m$ thick. Both are thought to have carrier concentrations in the range of $10^{18}/\text{cm}^3$ based on Hall measurements of similar samples for Si doped samples and cathodoluminescence for p type samples. Figure 6.3 shows a schematic diagram of the matching bridge used for detecting the change in resistance of the cantilever during deflection. An SEM micrograph of one of the piezoresistive cantilevers is shown on the top right. The measured change in resistivity of the cantilever during flattening is shown at the bottom. Calculating the gauge factor GF for this design is difficult given the uncertain equilibrium strain within the beam after separation. In addition, flexing the cantilever results in both positive and negative strains within the lever arms. A lower limit for the gauge factor can be obtained by using the fact that the cantilever bends up $10\,\mu$m at the end on release from the substrate, and assuming all of the strain is positive. This results in a GF of 0.5 for these cantilevers. This is significantly less than that obtained from planer devices on sapphire in which a GF of 260 was reported.[13]

Another example of the diverse microstructures which can be realized using this etch process is the GaN microchannel shown in figure 6.4. The microchannel consists of a $1\,\mu$m thick p-GaN membrane that spans between two long anchoring strips on either side. To fabricate this microchannel, a series of Ni/Au bars with $100\mu m$ spacing were patterned on the sample using standard lithographic techniques. The sample was then exposed to the PEC etch, during which the unmasked regions between the bars

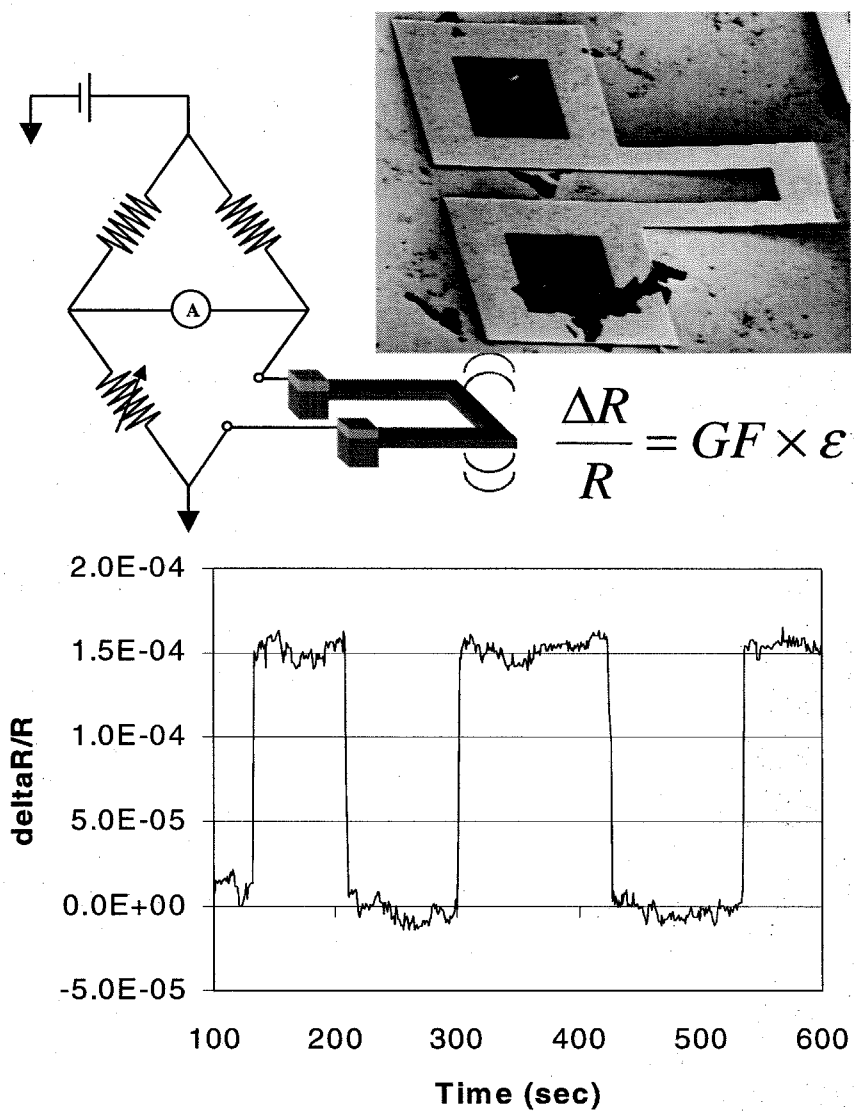

Figure 6.3: Piezoresistor setup and resulting voltage swing.

were undercut. Etching of n-GaN underlayer proceeded inward from both sides in the direction of the bars. A total undercut channel length of $5mm$ etched to completion in roughly 2 hours. This puts a lower limit on the selectivity of at least 500:1 for n type etch rate over p type etch rate. Figure 6.4 shows a schematic drawing of the resulting microtunnel. In addition, figure 6.4c shows an SEM side view and zoom in on the tunnel edge showing the bowing that results after separation of the p layer from the substrate. Figure 6.4b shows one of these channel structures with contacts made to the p type material above the anchoring regions of the structure. The picture is a top view of one of the tunnels. The dark areas are where the curvature of the surface results in reflection of light away from the collection optics of the microscope. The bright line down the middle is the horizontal surface of the top of the tunnel. The left figure shows this micropump with no voltage applied between the contacts, the right image shows the same area but with 10V applied between the contacts. It can be seen that the application of the bias results in a flattening of the surface a distance approximately $100\,\mu$m to either side of the contact region. This is believed to result from the heating of material between the contacts. As this material heats and expands locally, a strain gradient develops that eventually reaches a critical strain. At this point the system can lower its strain energy by deforming into the shape shown here. By producing a line of contacts and applying voltage to every other pair sequentially, a peristaltic pumping action can be generated down the length of the tunnel. This could potentially lead to an array of on chip analysis techniques interconnected via micropumps such as these. In addition, the cantilever piezoresistor structure has potential as a feedback mechanism for determining pump motion or pressure changes if integrated into the design of the layer structure grown for the device. Given the optical emission qualities of GaN, it is reasonable to believe that an optical emission-absorption-detection microanalysis device could be fabricated in which light emitted from a device on one side of the microtunnel could be detected by a device placed on the opposite side. The chemical stability of GaN may allow caustic chemicals to be investigated as well. These are just a couple ideas about possible applications to which this technique could be applied. The possibilities seem endless.

6.4 Chapter Summary

In summary, a method for selectively etching n type GaN is descrided. The effects of defects and growth method are discussed in terms of the resulting etched layer morphology. Finally, fabrication and characterization of a piezoresistive cantilever and micofluidic pump is detailed.

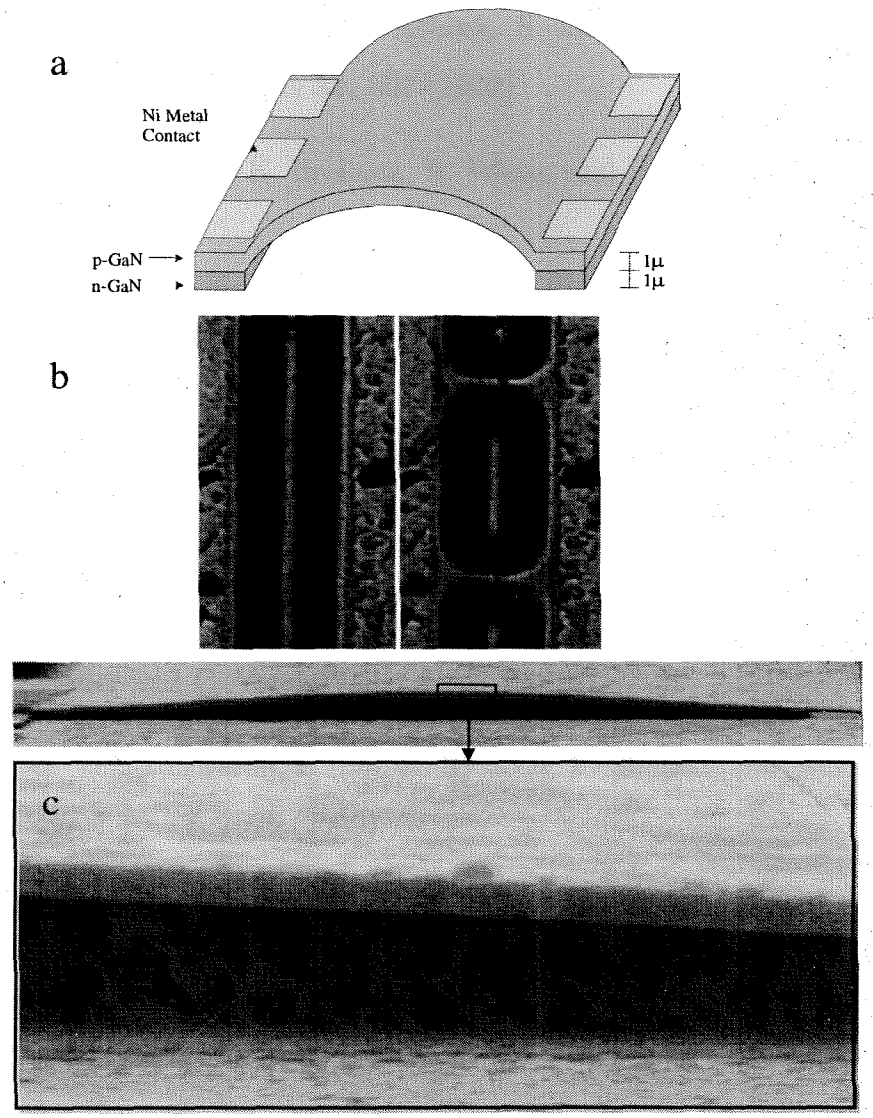

Figure 6.4: a) Schematic diagram of GaN microtunnel. b) optical view of micropump. Left picture shows device without applied voltage; right shows compression when voltage is applied to contacts. c) side view SEM of the end of a microtunnel.

Bibliography

[1] X. Dang, R. Welty, D. Qiao, P. Asbeck, S. Lau, E. Yu, K. Boutros, and J. Redwing, Electronic Letters **35**, 602 (1999).

[2] J. Kolnik, I. Ogusman, K. Brennan, R. Wang, and P. Ruden, J. Appl. Phys.**82**, 726 (1997).

[3] C. Johnson, J. Lin, H. Jiang, M. Khan, and C. Sun, Appl. Phys. Lett.**68**, 1808 (1996).

[4] M. Hirsch, J. Wolk, W. Walukiewicz, and E. Haller, Appl. Phys. Lett.**71**, 1098 (1997).

[5] A. Riben and D. Feucht, Solid State Elecron. **9**, 1055 (1966).

[6] J. Neugebauer and C. VandeWalle, Appl. Phys. Lett.**69**, 503 (1996).

[7] S. Ves, U. Venkateswaran, I. Loa, K. Syassen, F. Shahedipour, and B. Wessels, Appl. Phys. Lett.**77**, 2536 (2000).

[8] F. Shahedipour and B. Wessels, Appl. Phys. Lett.**76**, 3011 (2000).

[9] Y. Kwon, S. Shee, G. Gainer, G. Park, S. Hwang, and J. Song, Appl. Phys. Lett.**76**, 840 (2000).

[10] M. Minsky, M. White, and E. Hu, Appl. Phys. Lett.**68**, 1531 (1996).

[11] C. Youtsey, G. Bulman, and I. Adesida, JOURNAL OF ELECTRONIC MATERIALS **27**, 282 (1998).

[12] A. Stonas, P. Kozodoy, H. Marchand, P. Fini, S. DenBaars, U. Mishra, and E. Hu, Appl. Phys. Lett.**77**, 2610 (2000).

[13] R. Gaska, M. Shur, A. Bykhovski, J. Yang, A. Khan, V. Kaminski, and S. Soloviov, Appl. Phys. Lett.**76**, 3956 (2000).